Modelling and simulation of electromagnetic source mechanisms and sensor optimization via homogenization

Dissertation

zur Erlangung des akademischen Grades

Dr. rer. nat.

eingereicht an der
Mathematisch-Naturwissenschaftlich-Technischen Fakultät
der Universität Augsburg

von

Ursula Weiß

Augsburg, Oktober 2020

Erstgutachter: Prof. Dr. Malte A. Peter
Zweitgutachter: Prof. Dr. Markus Sause

Tag der mündlichen Prüfung: 04. Dezember 2020

Abstract

The failure of a brittle dielectric material under mechanical load generates acoustic emission (**AE**) and electromagnetic emission (**EME**).
Detection and analysis of acoustic signals are commonly used for the investigation of failure in solid materials. AE analysis aims at deriving information about the amount of damage, source position and type of damage from counting signal activity, localizing source positions and identifying classes of signals in order to investigate material failure.
Similar to AE analysis, counting and classification of EME signals can provide further information about accumulated damage and failure type. In experiments, we observe further a strong directional character of the EME source, which indicates that EME analysis allows conclusions about position and orientation of fracture surfaces in the material.
Both, AE analysis and EME analysis, allow conclusions based on real-time information on a qualitative basis. The lack of detailed understanding of correlation between source mechanisms and measured signals prohibit the reliability of quantitative information so far.

The profound understanding of the basic characteristics of the emitting EME source and the origins of the electromagnetic fields are essential to enable better analysis and interpretation of emitted signals.
We establish a model of the emitting source, which is capable of explaining the different parts of the experimentally obtained EME signals by comparison of simulation and experimental data obtained during mode-I fracture of epoxy resin materials. Three contributions of the EME signals originate from separation and relaxation of charges during crack growth and from the vibration of charged crack surfaces. The simulations reproduce the results of the experimentally examined directional character of the emitted electromagnetic field and the strong dependence of the amplitude of the signals on the distance of source and capacitive sensor plate.

The long-term objective of detection and analysis of EME and AE signals for the purpose of determination of failure type, location of failure and orientation of crack walls motivates the need for optimization of the EME sensor system. In particular, because there is no commercial sensor system available for EME detection until now, the development of EME sensor systems employed in the experiments is so far based on the experience of the scientists.
We approach the topic of sensor optimization using and extending the so-called method of shape optimization via homogenization and investigate the applicability of the method in the described context in order to answer questions related to the sensor design in the experiments.

Acknowledgements

I use my mother tongue for the acknowledgements, as it is much easier for me to find the right words. For the sake of completeness, here is the short version in English: I thank my supervisors Prof. Dr. Malte Peter and Prof. Dr. Markus Sause, my colleague Sebastian Gade and my family and friends, especially Lisa, Florian and Tom.

Ich bedanke mich an erster Stelle bei Prof. Dr. Malte Peter und Prof. Dr. Markus Sause. Bereits ihre Betreuung meiner Masterarbeit ermöglichte meine fachliche Neuorientierung von der Wirtschaftsmathematik hin zur angewandten Mathematik an der Schnittstelle zur Physik. Ich bin dankbar, dass ich so - besser spät als nie - den Sinn in meinem Studium gefunden habe und sie mich danach ermutigt und es ermöglicht haben, diese Entwicklung in einer Promotion weiter zu verfolgen.
Ich danke Prof. Dr. Malte Peter für die Begleitung und Unterstützung meiner fachlichen Entwicklung in der Promotionsphase und für die vielen Möglichkeiten meinen Horizont zu erweitern. Ich danke ihm insbesondere auch für seine uneingeschränkte Unterstützung meiner persönlichen Entwicklung und meiner Pläne.
Ich danke Prof. Dr. Markus Sause, dass er die Arbeit mit so engem Anwendungsbezug ermöglicht hat und für die unzähligen konstruktiven Diskussionen und sein immer offenes Ohr.

Besonderer Dank gilt an dieser Stelle auch Sebastian Gade. Seine experimentelle Daten und die gemeinsame Forschung sind die Basis für den ersten Teil dieser Arbeit.

Ich danke meiner Familie und meinen Freunden für die bedingungslose und immerwährende Unterstützung.

Besonderer Dank gebührt ...

- ... meiner Kollegin, Freundin und jetzt „Doktorschwester“ Lisa. Danke für alle großen und kleinen - immer bunten - gemeinsamen Momente.
- ... meinem Sohn Florian. Wenn du lachst, hüpft mein Herz vor Freude.
- ... meinem Mann Tom. Danke für einfach alles.

Contents

1. Introduction

In fibre-reinforced polymers, fibres made of carbon, glass or ceramics are embedded in a matrix of epoxy resin or polyester resin forming a composite material with material properties that differ from the respective single components. By varying for example fibre type, fibre content, length of fibres or fibre orientation, structural elements made of fibre-reinforced materials can be specifically adapted and optimized according to the load situation. High strength, stiffness and fatigue resistance in combination with low density make composite materials ideal for lightweight construction for example in aviation and space travel and therefore economically and technologically interesting.
To reach the full potential of a composite material, a detailed understanding of mechanisms that lead to damage and failure of the composite is required. The actual strength, durability and stiffness of composite structures is influenced by various damage mechanisms such as for example fibre failure, delamination or matrix cracking occurring under stress at numerous locations throughout the material [Hamstad, 1986]. All these different effects result in complex damage behaviour leading to limited predictability of material failure of fibre-reinforced polymers preventing exploitation of the full potential up to the present [Sause, 2016].
Acoustic emission (AE) analysis and electromagnetic emission (EME) analysis are non-destructive testing methods which make an important contribution to a better understanding of the complex processes involved in material failure.
AE analysis is a standard method for monitoring occurrence and development of damage in composite materials. Micro-deformations, which are usually linked to irreversible changes in the material such as crack formation and propagation, cause acoustic waves, which propagate in the material. Piezo-electrical sensors mounted on the surface of the material detect these acoustic waves and transform them into voltage signals, which provide the basis for further investigations. By counting signal activity, localizing source positions and identifying classes of signals, AE analysis aims at deriving information about the amount of damage, source position and type of damage in order to investigate material failure [Sause, 2016].
Emission of electromagnetic fields during failure of materials is a phenomenon, which has been under investigation for many years. First reported within minerals (sylvine) in 1933, EME was measured for different materials and failure types henceforward, substantiating that the emitted EME signals are highly dependent on material and failure types. [Frid et al., 2003]
Similar to the acoustic emission analysis, counting and classification of EME signals can

provide further information about accumulated damage and failure type. In contrast to AE analysis, source localization of an occurring failure is not possible in EME signal analysis without further information due to the propagation speed of electromagnetic waves close to speed of light. [Sause, 2016]
In cases where the separate methods approach their limits, combination of AE and EME analysis can be advantageous. For example, they form a good tool for crack localization based on time delay between detection of EME and AE signals due to the different propagation velocities of acoustic and electromagnetic waves [Sedlak et al., 2008].
Both, AE and EME analysis allow conclusions based on real-time information on a qualitative basis but the lack of detailed understanding of correlation between source mechanisms and measured signals prohibit the reliability of quantitative information so far [Sause, 2016].
For a comprehensive understanding of the processes during failure of fibre-reinforced polymers, it is essential to investigate failure of fibre and matrix individually. In a collaboration of experimental physics and applied analyis in the framework of the project "Relation of electromagnetic and acoustic emission to temporal and spatial crack motion on a microscopic scale in polymers and carbon fibres" funded by the DFG, the groups investigated AE and EME during crack propagation in polymers, carbon fibres and composite materials in different experiments accompanied by simulation.
This work is motivated by an experiment examining EME and AE during three-point bending tests of brittle dielectric materials carried out within the framework of the project. Figure 1.1 shows a sketch of the used setup.

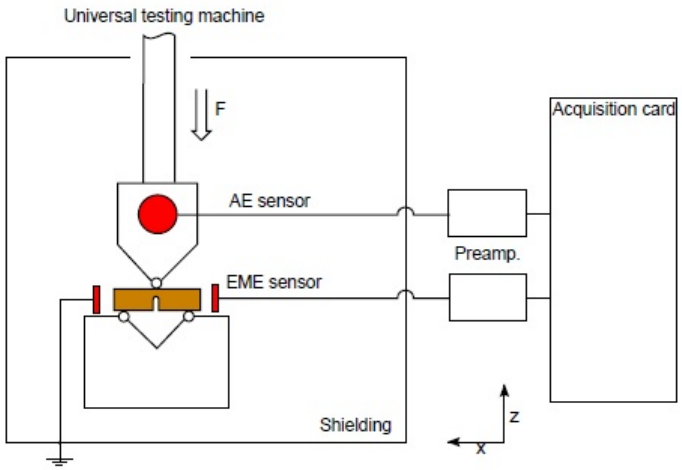

Figure 1.1.: Diagram of experimental setup (Graphics from: S. O. Gade et al., Relation of Electromagnetic Emission and Crack Dynamics in Epoxy Resin Materials, Journal of Nondestructive Evaluation, published 2014 by Springer Nature) [Gade et al., 2014].

In the experiments, force applied via a universal testing machine induces fracture of RTM6 specimen with force in the specimen acting perpendicular to the crack walls, which is called mode-I fracture. The setup enables simultaneous monitoring of AE and EME and ensures a distinct orientation of the crack surfaces in the material.
The origins of the emitted electromagnetic fields during failure of materials are still highly debated [Frid et al., 2003]. It is therefore necessary and aim of the experiment and the present thesis to gain a profound understanding of the basic characteristics of the EME source in order to enable better analysis and interpretation of emitted EME signals.
Figure 1.2 shows a typical pair of AE and EME signals measured in the experiments.

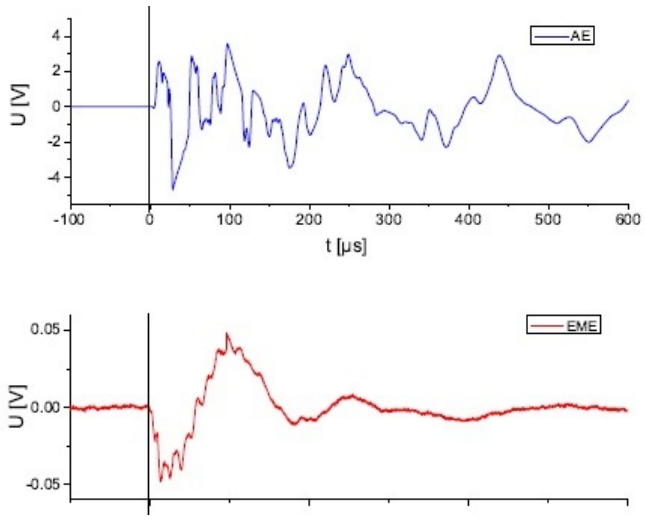

Figure 1.2.: Typical pair of AE and EME signals obtained in three point flexural tests of RTM6 (Graphics from: S. O. Gade et al., Relation of Electromagnetic Emission and Crack Dynamics in Epoxy Resin Materials, Journal of Nondestructive Evaluation, published 2014 by Springer Nature) [Gade et al., 2014].

The EME is measured by a capacitive sensor consisting of two copper plates. The left plate is grounded, the right plate is attached to a measurement circuit consisting of preamplifier and acquisition card.
The measured EME signal clearly shows two different signal components, a component referred to as the **base signal** in the following is superimposed by a **high-frequency component** (**superimposed oscillation**).
Low variance in orientation of the fracture surfaces of less than five degrees ensures a reproducible source of EME signals. Adjustability of the right plate of the EME sensor allows to study the influence of source–sensor distance on the EME signals, the rotation of the specimen allows to examine the influence of crack orientation. By investigation of relation of EME and crack dynamics and the influence of orientation and distance of the induced crack surfaces on the detectable EME signals, the experiment enables investigation

of the basic characteristics of the EME source.

Two main areas of interest arise from the described experiment.
On the one hand, a better understanding of the origins of EME and the characteristics of the source is required. For this purpose, we model the EME source in the experiment and develop a model of the EME source by comparison of simulation results with the experimentally derived data. Modelling and simulation of EME requires careful choice of involved equations of electrodynamics and solid mechanics and their appropriate coupling. Furthermore, it is particularly important that the discretization, i.e. mesh size and time step, is precisely adjusted to the model. It turns out that our derived and implemented source model is able to reproduce all experimentally observed characteristics of the EME source.
Besides the interest in the EME source, one is particularly interested in the optimal shape and position of the EME sensor in the experiment, which is still based on the experience of the scientists to date. Mathematical formulation of this problem as an optimal design problem reveals that the well-known theory of shape optimization via homogenization for real-valued material parameters must be extended to complex-valued material parameters. We investigate the extension of the method and point out the difficulties that arise in context of complex-valued material parameters. Under certain additional assumptions, we develop and implement a method that addresses the problem of EME sensor optimization.

Part I and Part II of this work deal with these two areas of interest.

Part I of the present work is concerned with modelling of the EME source in the epoxy resin specimen. Simulations compared to the experimental results investigate the source mechanisms of EME during crack propagation and enable the development of an EME source model.

Part II of the thesis focuses on questions concerning the optimal shape and position of the EME sensor used in the experiments. To this end, we first theoretically investigate an extension of the method of shape optimization via homogenization. In a further step, the application of the derived method allows to answer questions about the optimal sensor design which arise in connection with the experiment.

Part I.

Investigation of source mechanisms of electromagnetic emission during crack propagation caused by mode-I failure in epoxy resin materials

In the first part of this work, we focus on modelling the EME source in the specimen. The origins of the EME are still widely discussed and the lack of a source model comprising all the so far experimentally found characteristics of the EME source motivates the development of a new source model. Simulations compared to the experimental results form the basis for investigation of source mechanisms of the EME during crack propagation. In this way, we establish a model of the emitting source which is capable of explaining the different parts of the experimentally obtained EME signals. Three contributions of the EME signals originate from separation and relaxation of charges during crack growth and from the vibration of charged crack surfaces. The conducted experiments show a directional character of the emitted electromagnetic field and a strong dependence of the amplitude of the signals on the distance of source and capacitive sensor plate. We are able to reproduce these results in the simulations based on the proposed source model.

In order to ensure the comparability of simulated and experimentally obtained data, the basic 3d setup of the later discussed models matches the experimental geometry of the flexural test setup for polymers (see figure 1.1). In the following, the experimental data for comparison of the simulation to experimental results is courtesy of S.O. Gade and published in the joint paper [Gade et al., 2014] by S.O. Gade, U. Weiss, M.A. Peter and M.G.R. Sause.

Part I of this thesis is structured as follows.
In chapter 2, the developed EME source model is introduced and an overview of the different source model approaches considered in the simulations is presented. Furthermore we provide the necessary background to mathematical modelling and simulation of the involved mechanisms and the post-processing of the simulation results. In chapter 3, we approach the described EME source model by considering the charge distribution as a function of crack growth on hypothetical crack surfaces in the material in our model. In first simulations, we reproduce a representative EME signal by time-dependent charge generation on one hypothetical crack surface. In order to include the measured directional character of the EME source as well, we extend the model further and take into account time- and position-dependent charge generation on two hypothetical crack surfaces in the specimen. Chapter 4 is concerned with the EME signal component originating from the vibration of the charged crack surfaces. We couple the model derived in the previous chapter with crack wall vibration in the specimen. Chapter 5 concludes by summarising the findings of Part I.

2. Towards an EME source model

The following sections provide the basis for the simulations described in chapters 3 and 4. §2.1 recaps the existing source model approaches and introduces a new source model supporting the experimental findings concerning the characteristics of EME. §2.2 presents the examined source models and §2.3 is concerned with mathematical modelling of the proposed source model including simplifications. §2.4 describes important details of the implementation based on the described equations in the simulation software COMSOL Multiphysics®, §2.5 describes the procedure for final comparison of signals from experiment and simulation using a transfer function taking into account the measurement electronics.

2.1. Source model theory

The first models of the source of electromagnetic emission during failure of samples of sylvine were established in the late seventies [Frid et al., 2003]. Since that time different attempts were made to combine all experimentally found characteristics of electromagnetic emission in one source model. In [Sause, 2016], M. Sause categorizes the different approaches roughly as dislocation models, discharge models, capacitor models and Frid's electrical surface wave model.
Despite the variety of existing attempts all models so far established fail for different reasons. In [Frid et al., 2003], Frid et. al recap and review the different theories and provide a new model based on already existing and at the time new found experimental results. Following their argumentation, an all-encompassing source model has to explain the different experimentally found characteristics of EME sources summarized by Frid:

- Occurrence as individual pulses or clusters of pulses
- Influence of fracture dynamics/dimensions
- Dependence on material properties
- Distinct character and orientation
- Occurrence independent of crack mode (tensile and shear cracks).

Frid et al. suggest that the typical shape of EME signals originates from the generation of a charge source with strength proportional to the crack area growth and oscillations on both sides of the crack originating from electrical surface waves. Despite the consideration

of all the aspects mentioned before, this electrical surface wave model is not supported by the results presented in the following.

In [Sause, 2016], M. Sause points out that a valid source model has to include in particular the contributions of mechanical movement occurring during crack propagation, which are not included in Frid's model.

At first, simulations question the idea of a correlation between the form of the base signal and mechanical effects of the vibration of the crack surfaces. Data derived from test source experiments in comparison with simulation results described in chapter 3 clarify that the form of this signal part actually originates from the bandwidth of the recording setup. Nevertheless, further simulations described in chapter 4 show that vibration of crack surfaces potentially acts as source for the superimposed oscillation observed in the EME signals.

The lack of a source model comprising all the experimentally found characteristics confirms the need of introduction of a new source model. In our proposed model, we conclude the EME signals for mode-I failure of brittle materials to originate from three contributions which are shown schematically in figure 2.1:

1. **Generation of charges** at the crack tip due to breakage of molecular bonds (which results in temporal increase of charges),

2. **Charge relaxation** dependent on the material properties and the geometry of the crack,

3. **Charge movement** due to crack wall vibration.

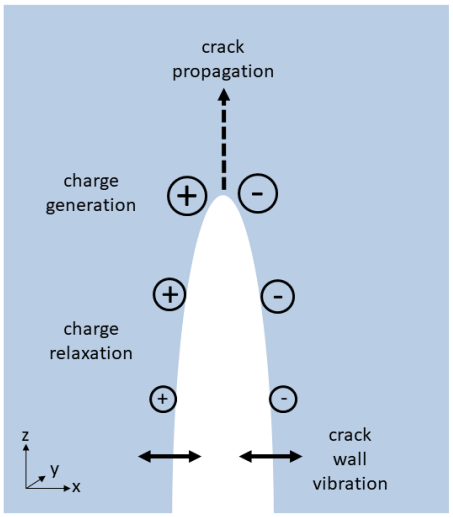

Figure 2.1.: Schematic description of signal generation.

The following simulations and comparison of the results with experimental data substantiate our hypothesis of the formation of the electromagnetic signals:
When a crack propagates in the material molecular bonds break and charges appear at the crack surface, leading to an asymmetric charge separation. This results in a rise of the potential at the sensor. The temporal characteristic of the resulting charge distribution is related to the propagation velocity of the crack tip in the material. The separated charges then recombine with a relaxation time depending on the dielectric properties of the material and the geometry of the crack. The combination of both effects causes a temporal increase of charges due the progress of crack propagation and a subsequent decrease due to charge relaxation. As we will see later, these contributions result in the base signal component.
Another part of the signal is created by vibration of the charged crack surfaces. The charges present at the crack surfaces move according to the present mechanical movement of the crack surfaces as long as they are present. This movement results in the superimposed oscillation in the signal.
In the following we investigate whether the described source hypothesis is suitable to describe the experimentally obtained signals and source characteristics.

2.2. Overview of examined source model approaches

In order to deepen the understanding of the characteristics of the EME source mechanism and to confirm our hypothesis of EME formation during mode-I fracture, we approach

the complete source model described in §2.1 step by step. This procedure enables the investigation of dependencies between different characteristics of the source and their effects in the obtained signal as well as the development of a profound understanding of the experimental setup and included measurement electronics. Furthermore the successive approach allows for initial avoidance of a direct modelling of mechanical effects of crack propagation in order to get around the computational costly consideration of fracture mechanics in the models.

In a first attempt (Model 1a), the electromagnetic emission source as a function of time on one internal boundary of the single-edge notched beam as displayed schematically in figure 2.2 deepens the understanding for the model geometry, signal processing and post-processing and enables first comparisons of simulated and experimentally obtained signals.

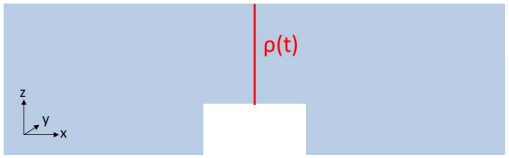

Figure 2.2.: Schematic description of Model 1a.

The second attempt (Model 1b) with time- and position- dependent application of charge following the crack tip on two hypothetical crack surfaces in the specimen (see figure 2.3 for schematical description) allows for reproduction of the directional behaviour of the emitting source observed in the experiments.

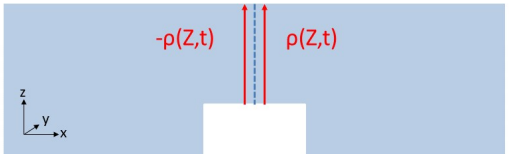

Figure 2.3.: Schematic description of Model 1b.

In our third attempt (Model 2), schematically shown in figure 2.4, we attend to the superimposed oscillation by including mechanical movement of the hypothetical crack surfaces (crack wall vibration) following a prescribed oscillation in a generalized geometry setting.

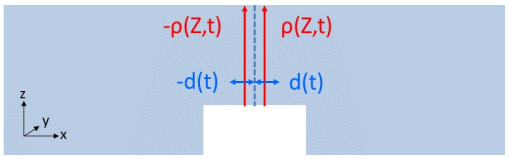

Figure 2.4.: Schematic description of Model 2.

2.3. Mathematical modelling of electrodynamics and solid mechanics

In order to model the sources of EME described in §2.2, we consider the equations describing the corresponding phenomena, namely Maxwell's equations of electrodynamics and simplifications thereof for charge generation and relaxation and the equations of solid mechanics for inclusion of crack wall vibration in the simulation model. The following sections recap the key aspects of the mathematical description of electrodynamics and solid mechanics in context of the presented topic and make use of standard notation. A short introduction to both topics can be found for example in [Eck et al., 2011], a more detailed explanation of electrodynamics in [Bartelmann et al., 2018].

2.3.1. Maxwell equations and simplifications

The following exposition is based on [Eck et al., 2011] and [Bartelmann et al., 2018]. The basis for mathematical consideration of electrodynamics is formulated in **Maxwell's equations**:

$$\nabla \cdot E = \frac{\varrho}{\epsilon_0} \tag{2.3.1}$$

$$\nabla \cdot B = 0 \tag{2.3.2}$$

$$\nabla \times E = -\frac{\partial B}{\partial t} \tag{2.3.3}$$

$$\nabla \times B = \mu_0 \left(J_c + \epsilon_0 \frac{\partial E}{\partial t} \right) \tag{2.3.4}$$

with **electric field** E, **magnetic field** B, **permittivity of free space** ϵ_0, **permeability of free space** μ_0, **electric charge density** ϱ and **electric current density** J_c. This formulation relates to a representation on microscopic scale including total charge and total current at atomic level. The equations are therefore called **microscopic version of Maxwell's equations**.

Gauss' law (2.3.1) describes charges as source of the electric field whilst equation (2.3.2) states that the magnetic field is solenodial. Faraday's law of induction (2.3.3) describes the generation of electric field by a time-varying magnetic field. (2.3.4) states that magnetic fields are in turn generated by electric current or by time-varying electric fields.

Since the magnetic field is not subject of investigation of neither the experiment nor simulations and, based on the assumption of negligible inductive effects, we reduce our system to:

$$\nabla \cdot E = \frac{\varrho}{\epsilon_0} \qquad \text{Gauss' law} \tag{2.3.5}$$

$$\nabla \times E = -\frac{\partial B}{\partial t} = 0 \qquad \text{Faraday's law of induction.} \tag{2.3.6}$$

The electric field is therefore considered as irrotational, what allows to describe the electric field as gradient of a scalar potential V, provided that one considers a simple connected domain:

$$E = -\nabla V. \tag{2.3.7}$$

The consideration of single charges and their effects is unmanageable in applications, therefore one passes to the description of **Maxwell's equations in macroscopic formulation**.

2.3.1.1. Macroscopic formulation of Maxwell's equations

When an electric field is applied to a dielectric material, the material reacts to the field in terms of electric dipoles at microscopic level what is macroscopically reflected in a **bound charge density** ρ_b. The **total charge density** ρ consists of this bound charge density ρ_b and the charge density generated by **free charges** ρ_f . The part from the free charges can be split up again into a part ρ_{ext} originating from external charge distribution and a part from free charge carriers in the material ρ_c. [Bartelmann et al., 2018]

$$\begin{aligned} \rho &= \rho_b + \rho_f \\ &= \rho_b + \rho_c + \rho_{ext}. \end{aligned}$$

Here and in the following we explicitly consider ρ_c and ρ_{ext} separately. In the following ρ_{ext} serves for the formulation of the EME source in the material.
Introducing the **dielectric displacement field D**

$$D = \epsilon_0 E + P$$

covering the materials reaction to the electric field due to bound charges by the **polarization field P**

$$\rho_b = -\nabla \cdot P \tag{2.3.8}$$

equations (2.3.5) and (2.3.6) transform to the macroscopic formulation

$$\nabla \cdot D = \rho_f \qquad \text{Gauss' law} \tag{2.3.9}$$

$$\nabla \times E = 0 \qquad \text{Faraday's law.} \tag{2.3.10}$$

According to the charge density, the **conduction current density** J_c is due to free

charges in the material, the temporal change of the dielectric displacement D generates the **displacement current density** J_d:

$$J_d = \frac{\partial}{\partial t} D \tag{2.3.11}$$

The equation of continuity guarantees conservation of free charges in the material:

$$\nabla \cdot J_c = -\frac{\partial \rho_c}{\partial t} \qquad \text{charge conservation} \tag{2.3.12}$$

stating that the source of the conduction current is a temporal change of the free charge density in the material.
The equations considered so far are material independent. They are supplemented by Ohm's law and constitutive relations described in the following.
We complement Maxwell's equations by Ohm's law, expressing the proportionality of electric field E and conduction current density J_c:

$$J_c = \sigma E \qquad \text{Ohm's law,} \tag{2.3.13}$$

introducing the **conductivity** σ of the material which is in general given as a tensor.
Furthermore, we supplement the given equations by the material law which describes P as function of the electromagnetic field. In linear media with slowly varying fields, P is proportional to E:

$$P = \epsilon_0 \chi_e E \tag{2.3.14}$$

with electric susceptibility χ_e, describing the ability of a material to polarise in response to an applied electric field. Introducing the **relative permittivity** $\epsilon_r = 1 + \chi_e$ of the material, which is in general given as a tensor we deduce

$$D = \epsilon_0 E + P = \epsilon_0 \epsilon_r E \qquad \text{constitutive relation.} \tag{2.3.15}$$

Together with further simplifying assumptions stated in the following, the described equations form the basis for modelling in Part I of this work. Given the previously derived equations describing electrodynamics without inductive effects, we consider two further simplified sets of equations in our models, namely the **equations of electric currents** and the **equations of electrostatics**. As already stated we model the source of the EME by ρ_{ext}.
The following considerations form the basis for the equations implemented in the later described models. A short introduction can be found in [Com, 2015b].

2.3.1.2. Equations of electric currents

The wavelengths of the occurring electric fields are large compared to the geometrical dimensions of the experimental setup. This allows us to neglect induced electric fields. In

Model 1a described in §3.2, we therefore initially decided on modelling the contributions due to charge generation and relaxation via a current conservation equation based on Ohm's law, which follows from the previous described equations without any further assumptions or simplifications. Besides the generation of charges at the crack tip modelled by ρ_{ext} the contribution of the source model due to relaxation of charges is included in the model by the conductivity σ of the material.
Based on equation (2.3.9) we deduce

$$\nabla \cdot (\frac{\partial}{\partial t} D) = \frac{\partial}{\partial t}(\rho_c + \rho_{ext}). \tag{2.3.16}$$

Inserting the continuity equation of charge conservation (2.3.12) we conclude

$$\nabla \cdot (\frac{\partial}{\partial t} D + J_c) = \frac{\partial}{\partial t}\rho_{ext}. \tag{2.3.17}$$

Together with Ohm's law (2.3.13) this leads to the following system of equations

$$\nabla \cdot J = Q_j \tag{2.3.18}$$

$$J = \sigma E + \frac{\partial D}{\partial t} = (\sigma + \epsilon_0 \epsilon_r \frac{\partial}{\partial t})E \tag{2.3.19}$$

$$E = -\nabla V, \tag{2.3.20}$$

accounting for conduction currents and displacement currents with current source

$$Q_j = \frac{\partial}{\partial t}\rho_{ext}. \tag{2.3.21}$$

When modelling via the electrical currents approach, the sensor plates are modelled as ideal conductors by use of corresponding boundary conditions. These boundary conditions ensure that the potential on connected surfaces is equal, which corresponds to an effective conductivity of $\sigma = \infty$.
The derived equations of electric currents (2.3.18), (2.3.19) and (2.3.20) form the basis for modelling the EME source in Model 1a, cf. §3.2.

2.3.1.3. Equations of electrostatics

The previous described approach is chosen when accounting for relaxation of charges during the considered period of time due to conductivity of the material.
However, results of conducted test source experiments and comparative simulations showed, that in the described experiment with the material used this source component plays a subordinate role for the signal formation of the measured signals. Consequently we reduce our model by neglecting migration of charges in the material and switch to a quasi-static modelling of the problem in §3.3 and §4. We assume equilibrium state description of the problem in every single point in time neglecting the charge relaxation during the observation

time. By $\rho_c = 0$ in (2.3.9) the system reduces to the description of electrostatic field in dielectric media containing no free charge carriers. We consider the source of the EME as an explicitly described spatial distribution of the electric charge density ρ_{ext} in every time t:

$$\nabla \cdot (\epsilon_0 \epsilon_r E) = \rho_{ext} \tag{2.3.22}$$

$$E = -\nabla V. \tag{2.3.23}$$

Again conductive materials of the sensor plates are modelled as ideal conductors by application of corresponding boundary conditions.

2.3.2. Equations of Solid Mechanics

Consideration of mechanical movement of crack walls in our model in chapter 4 requires coupling of the equations describing the signal contribution of charge generation and relaxation with the equations of solid mechanics. The following exposition is based on [Eck et al., 2011].

In addition to the spatial (Eulerian) coordinates $x = (x, y, z)^T$, continuum mechanics makes use of the material coordinates $X = (X, Y, Z)^T$, also referred to as reference coordinates or Lagrangian coordinates.

Material coordinates are defined by the position of a material point in the reference configuration at $t = 0$ without any force.

When a solid object is deformed due to an applied force, the displacement $u(X, t)$ of material point X in time t is described by the difference of the current spatial position x of X and the original position of X:

$$x(X, t) = x(X, 0) + u(X, t) = X + u(X, t). \tag{2.3.24}$$

In solid mechanics we solve for the displacement field $u = (u, v, w)^T$.

The local measure for the deformation is the deformation gradient F

$$F = \nabla u + I, \tag{2.3.25}$$

where ∇u is the displacement gradient

$$\nabla u = \begin{pmatrix} \frac{\partial u}{\partial X} & \frac{\partial u}{\partial Y} & \frac{\partial u}{\partial Z} \\ \frac{\partial v}{\partial X} & \frac{\partial v}{\partial Y} & \frac{\partial v}{\partial Z} \\ \frac{\partial w}{\partial X} & \frac{\partial w}{\partial Y} & \frac{\partial w}{\partial Z} \end{pmatrix}. \tag{2.3.26}$$

The columns of F correspond to the tangent vectors of the images of the coordinate lines in the deformed state.

Consider two points X and $X+a$ with small distance $|a|$ before deformation. The distance of the two points in the deformed configuration can be derived by Taylor expansion:

$$|x(X+a)-x(X)| \sim |(I+\nabla u)a| = (a^T(I+\nabla u)^T(I+\nabla u)a)^{1/2}. \tag{2.3.27}$$

A local measure for length variation is therefore described by

$$C := (I+\nabla u)^T(I+\nabla u) = F^T F, \tag{2.3.28}$$

called Cauchy–Green deformation tensor. In contrast to F, it accounts for strain but not for rigid-body rotation.

Further, we introduce the Green–Lagrange strain tensor G

$$G := \frac{1}{2}(C-I) = \frac{1}{2}(\nabla u + \nabla u^T + \nabla u^T \nabla u), \tag{2.3.29}$$

which is again symmetric and independent of rotation.

The stress tensor describes the stress state in a certain point in the deformed material. Depending on the considered coordinate system, there are different formulations of the stress tensor, namely Cauchy stress σ, First Piola–Kirchhoff stress P and Second Piola–Kirchhoff stress S, which can be transformed by the following relations:

$$\begin{aligned} S &= F^{-1}P \\ \sigma &= J^{-1}PF^T, \end{aligned}$$

where J is the ratio between current and initial mass density

$$J = \frac{\varrho}{\varrho_0} = \det(F). \tag{2.3.30}$$

Cauchy stress is true stress formulated in Eulerian coordinates relating forces in the present configuration to areas in the present configuration. In contrast, the Piola–Kirchhoff tensors refer to areas in the reference configuration. For the First Piola–Kirchhoff stress, the forces are described in spatial directions, while for the Second Piola–Kirchhoff stress both area and force are described in the reference configuration.

The equation of motion in material configuration can be derived from the conservation of momentum formulated in material coordinates combined with Gauss' divergence theorem:

$$\varrho_0 \partial_t^2 u - \nabla \cdot P = F_V, \tag{2.3.31}$$

with the First Piola–Kirchhoff stress tensor P. The density ϱ_0 corresponds to the material density in the initial undeformed state, the volume force F_V has components in the actual configuration but given with respect to the undeformed volume.

Two linearisation steps provide a linear model for elastic materials.
For infinitesimal deformations, i.e. when ∇u is small, we linearize G, which is called geometric linearization:

$$G = G(u) = \frac{1}{2}(\nabla u + \nabla u^T + \nabla u^T \nabla u) \sim \frac{1}{2}(\nabla u + \nabla u^T). \tag{2.3.32}$$

The tensor ε

$$\varepsilon(u) = \frac{1}{2}(\nabla u + \nabla u^T) \tag{2.3.33}$$

is then called linearised strain tensor. In the course of geometric linearisation, the differences in the stress tensors disappear. We follow the diction in literature and denote the stress tensor by σ.
Assuming linear behaviour of the material we complement the equation of motion by Hooke's law:

$$\sigma_{ij} = \sum_{k,l=1}^{3} c_{ijkl}\epsilon_{kl}(u) \text{ for } i,j = 1,2,3, \tag{2.3.34}$$

with 4th order elasticity tensor C with components c_{ijkl}, which has 21 independent components due to symmetry reasons.
In the modelling of the experiment in chapter 4 we are dealing exclusively with homogeneous isotropic materials. In this case the number of independent elastic constants is reduced from 21 to 2 and the elasticity tensor is described by $C = C(E, \nu)$, with modulus of elasticity E and Poisson's ratio ν. This results in reduction of the equation of continuity to

$$\varrho_0 \partial_t^2 u - \frac{E}{2(1+\nu)}\Delta u - \frac{E}{2(1+\nu)(1-2\nu)}\nabla\nabla \cdot u = F_V. \tag{2.3.35}$$

This equation becomes important in chapter 4, when the model is coupled with mechanical movement of the hypothetical crack surfaces.

2.4. Implementation in COMSOL Multiphysics®

We perform the simulations with COMSOL Multiphysics®, a simulation software based on the Finite Element Method (FEM) [Com, 2015a].
Based on the graphical user interface (GUI) the user follows the typical workflow to generate a simulation model: First the model geometry is defined and corresponding materials are assigned. In a next step, the partial differential equations relevant for modelling of the considered physical processes are selected and suitable boundary and initial conditions are assigned to the geometry. In addition to direct modelling by PDEs, this can also be done via so-called physics interfaces and modules, which already summarise the corresponding partial differential equations for modelling certain phenomena. For modelling of the described EME source mechanisms, we use the Electric Currents respectively the Electrostatics interface from COMSOL®'s AC/DC Module and the Solid Mechanics interface

from the Structural Mechanics Module, which solve for the respective equations described in §2.3.1 and §2.3.2.
In a final step, the user defines a mesh on the corresponding geometry and chooses appropriate shape functions for the spatial discretization via FEM. Discretization in time is carried out by means of a selected time step and time-stepping algorithm for time-dependent problems.
A careful choice of mesh and time-step suitable to resolve the occurring frequencies is important to guarantee success of the FEM. Theoretical considerations on the occurring wavelengths and comparison of signals with different mesh-size and time-step performed with Model 1a form the basis for the mesh and time-stepping applied in the described simulations, for details see §3.2.
Besides the advantage of user-friendly and application-oriented model generation via GUI, COMSOL Multiphysics® is particularly made for coupling of different physics, which is of major interest in Model 2, when the equations of electrostatics are coupled with equations of solid mechanics.

2.5. Transfer function

In the simulations we evaluate the electric potential averaged over the non-grounded plate of the capacitive sensor as resulting signal. The design of the models does not include the signal processing part of the measurement electronics, i.e. preamplifier and acquisition card of the experimental setup (see figure 1.1). Thus, one has to distinguish between the signals present at the sensor and the signals produced as output in the experiment. Direct comparison of experimental results and results of the simulation is not possible and a post-processing step is introduced.
This step requires a deeper understanding of the EME acquisition system and investigation of its influence on the signal transmission. For this purpose, test-source experiments were conducted: an antenna coupled to an arbitrary waveform generator was introduced into the described experimental setup as a test source emitting an electric field in place of the specimen. Both periodic voltage signals within a frequency range of 100[Hz] to 1[MHz] as well as specific waveforms resembling the hypothetical temporal characteristics of the electric field as function of crack growth were generated and emitted by the antenna. The corresponding output was then analysed to study the influence of the sensor system on the signal processing, for details see [Gade et al., 2014].
The results of these test-source experiments form the basis to describe the transmission behaviour of the measurement electronics using a transfer function. For an input signal $u_{\text{in}}(t)$ generated by the waveform generator, we denote by $u_{\text{out}}(t)$ the corresponding output signal. The transfer function $H(\omega)$ relates the Fourier transformed signals

$$H(\omega) = \frac{\mathcal{F}\{u_{\text{out}}(t)\}}{\mathcal{F}\{u_{\text{in}}(t)\}}$$

and describes how signals are transformed by the sensor system.
By use of the derived transfer function accounting for the influence of preamplifier and acquisition system, we can convert the evaluated results of the models in a post-processing step into signals which can directly be compared to the signals obtained in the experiment. Due to the mode of its derivation, the transfer function reflects the measurement chain only up to an unknown scale factor. Comparison between simulation and experiment also apply up to a scaling and it is neither possible to conduct any quantitative comparison of simulated and experimentally obtained signals, nor draw quantitative conclusions on the amount of charge present at the crack surfaces.

3. Model 1: Charge distribution as function of crack propagation

Approaching the full source model step by step, a first attempt focuses on the modelling of charge distribution due to crack propagation in the specimen and does not include mechanical movement of crack surfaces.
To enable comparison of simulated and experimentally derived EME signals, Model 1a and Model 1b cover the complete experimental setup.

3.1. Basic setup: Geometry and Material

The model geometry displayed in figure 3.1 represents the experimental setup consisting of RTM6 specimen, test fixture made of non-conducting materials, the grounded shielding box and other construction parts, and the EME and AE sensors (cf. [Gade et al., 2014]). Geometrical simplifications are made for details of components such as screws, sensor holders, acoustic sensor and parts of the universal testing machine whenever the influence on the detected signal is assumed to be negligible.

- The **test fixture** is made from nonconducting materials. The load pins consist of polyvinyl chloride (PVC) and the rest of the fixture of polymethyl methacrylate (PMMA).
- The **specimen** made of RTM6 with size of $25 \times 5 \times 5$ [mm] (length, height, width) and notch of $1 \times 3 \times 5$[mm] can be rotated with the bend fixture along the z-axis in order to investigate the influence of the detection angle, see figure 3.2.

  The different source models applied in Model 1a and 1b require different geometry of the RTM6 specimen concerning the hypothetical internal crack surfaces. Details are described in §3.2.1 and §3.3.1
- The **acoustic emission sensor** (KRN type "Glaser" sensor) consists of a simplified geometry which is grounded, according to the experimental setup.
- The electromagnetic signals are detected via two small copper plates (ca. $6 \times 8 \times 1$ [mm] (length, height, width)) forming a **capacitive sensor**. Following the experimental setup, the sensor plates in Model 1 are not arranged completely symmetrically, but vary slightly in their height position.

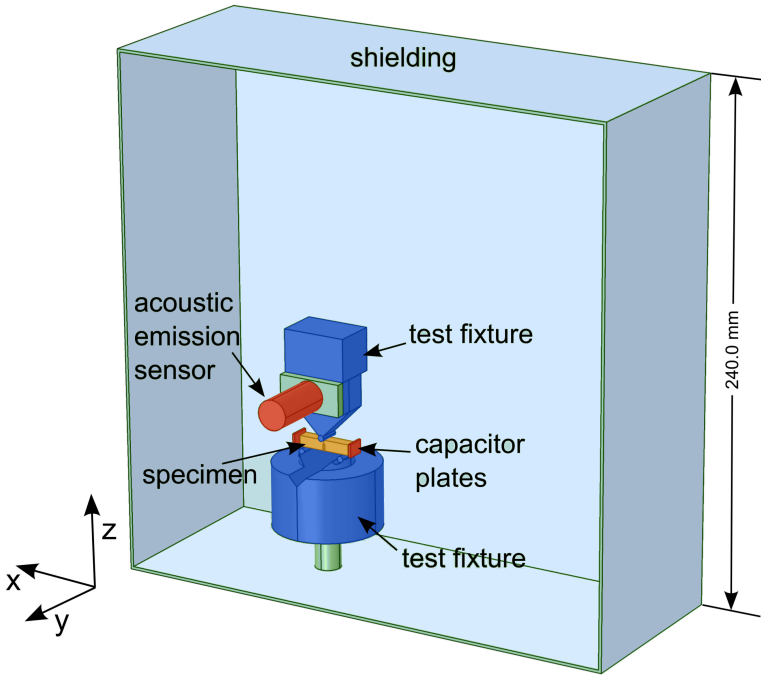

Figure 3.1.: Geometric setup of Model 1a and Model 1b (Graphics from: S. O. Gade et al., Relation of Electromagnetic Emission and Crack Dynamics in Epoxy Resin Materials, Journal of Nondestructive Evaluation, published 2014 by Springer Nature) [Gade et al., 2014].

- The whole setup is shielded against electromagnetic noise in a grounded aluminum box of 3[mm] thickness.

The following material properties are assigned to the corresponding domains. Table 3.1 lists the properties of the materials employed in the model, for details see [Gade et al., 2014].

Material	relative permittivity ϵ_r	conductivity σ [S/m]
PVC	2.90000	1.000 e-14
PMMA	3.00000	1.000 e-14
RTM6	4.12538	6.668 e-10
Air	1.00059	8.000 e-15

Table 3.1.: Material properties applied in the model

All boundaries of left capacitor plate, the bolt on which the test fixture is mounted on, the

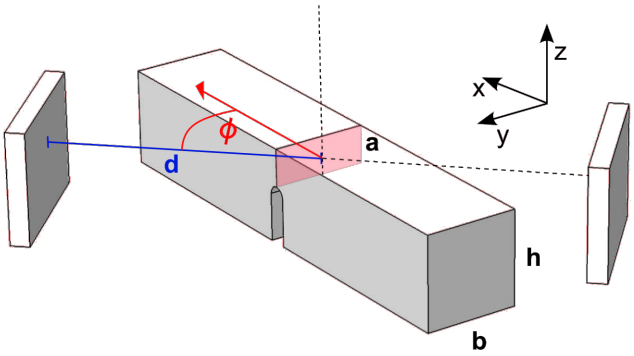

Figure 3.2.: Rotation of the specimen enables investigation of the detection angle (Graphics from: S. O. Gade et al., Relation of Electromagnetic Emission and Crack Dynamics in Epoxy Resin Materials, Journal of Nondestructive Evaluation, published 2014 by Springer Nature) [Gade et al., 2014].

acoustic sensor and the shielding box are grounded in accordance with the experimental setup. The non-grounded capacitor plate is considered as ideal conductor with infinite conductivity $\sigma = \infty$, which is modelled by application of a floating boundary condition on its surface.

We evaluate the electric potential averaged at the right plate of the capacitive sensor as resulting signal in our simulations. The signal processing part of the measurement chain consisting of preamplifier and acquisition card is taken into account by a system transfer function derived from experimental data, the procedure is described in §2.5. The resulting signal can then be directly compared with the experimental signal.

3.2. Model 1a: Time-dependent charge generation on one hypothetical crack surface

In a first attempt we apply a time-dependent surface charge $\rho_{ext} = \rho(t)$ at the hypothetical crack surface position as schematically displayed in figure 3.3 with the aim of generating a first signal for comparison with experimentally obtained data.

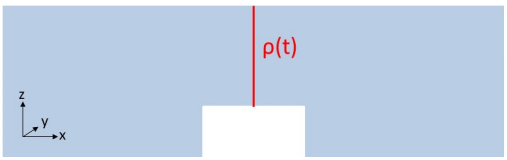

Figure 3.3.: Schematic description of Model 1a.

Containing the relevant parts of the signal regarding the frequency range the simulations

form the basis for investigations concerning mesh-size and time-stepping.

3.2.1. Source modelling

The maximum frequency of the oscillating signal component in the measured signals is 80 [kHz]. The wavelengths of the occurring electric fields are accordingly large compared to the geometrical dimensions of the experimental setup. Thus the approximation via electric currents approach as described in 2.3.1.2 is applicable.
In correspondence with the underlying source model hypothesis, the applied time-dependent surface charge density $\rho(t)$ splits into two parts, see figure 3.4: the first part represents the charge separation progress at the crack tip. A second contribution accounts for the effect caused by the movement of charges due to mechanical movement during crack wall vibration. In this model we replace oscillations due to mechanical movement with oscillations generated by time-variation of the charge density. This approach enables first comparisons between simulated and experimentally obtained signals without involving the additional computational effort of including the equations of solid mechanics in the model. Superposition of both parts forms the surface charge density applied on one internal boundary mimicking the crack surface in the material.
Simulations are performed for fixed source–sensor distance of $d = 14$ [mm] in the basic arrangement of the experiment with $\phi = 0$, see figures 3.1 and 3.2.

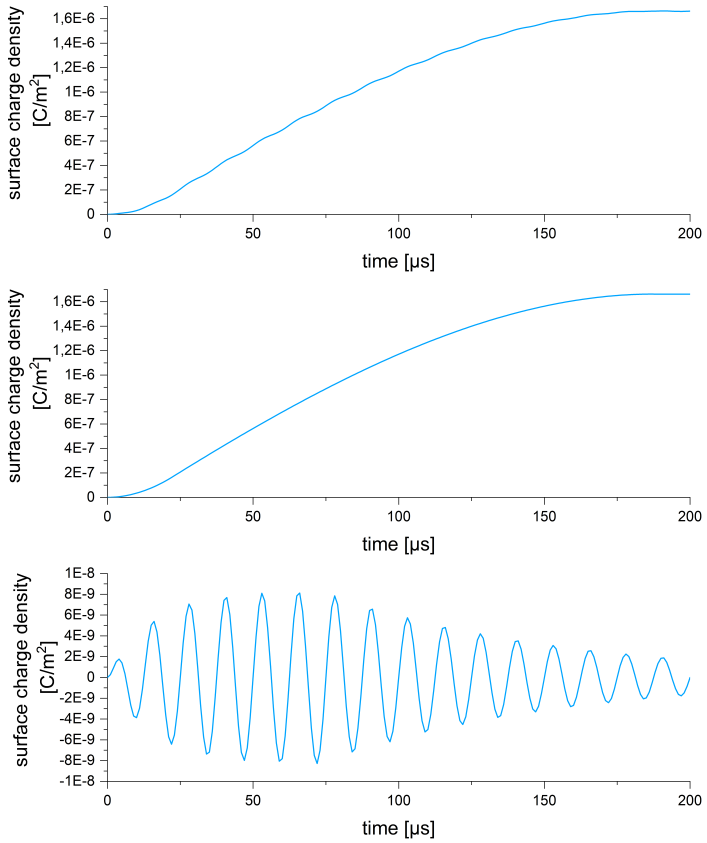

Figure 3.4.: Applied surface charge density (above) consisting of part due to charge separation progress at the crack tip (middle) and part due to crack wall vibration (below).

3.2.2. Simulation results

Besides the derivation of the transfer function we were able to reproduce a representative EME signal in the test source experiment. The direct comparison of experimentally obtained and simulated signals is in the following based on the signal resulting from this experiment.

The described modelling approach of Model 1a results in a simulated signal showing good accordance with the experimentally obtained signals of the test source experiment. As described in §2.5, a post-processing step takes into account the measurement electronics via transfer function. This step allows direct comparison of measured signals and transformed results of the simulation.

Figure 3.5 shows the measured test source signal and the simulation result.

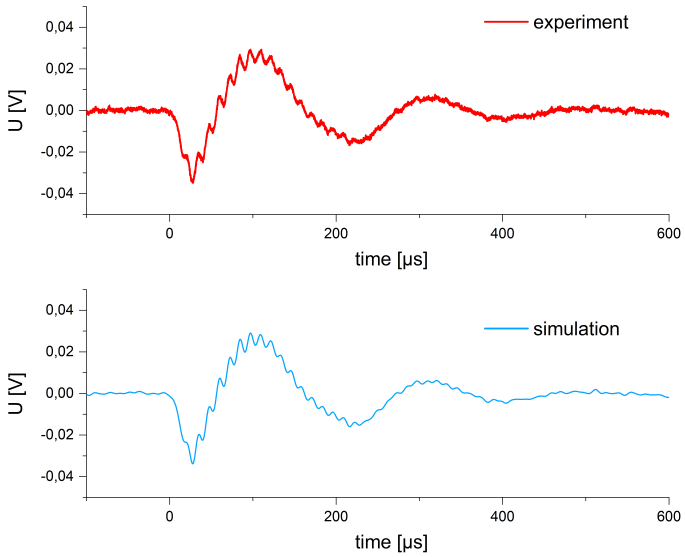

Figure 3.5.: Comparison of test source signal and converted result of simulation (Model 1a).

The results of simulation confirm the hypothesis that generation of charges and time-dependent variation of their strength lead to EME signals similar to those detected in the experiments.
Initial considerations that the observed form of the base signal part stems from the vibration of the charged crack surfaces, are disproved. Simulation results reinforce that the base signal at the non-grounded sensor plate is directly proportional to the charges present at the crack surfaces. Figure 3.6 shows the corresponding simulated signal derived at the sensor before before the post-processing step.

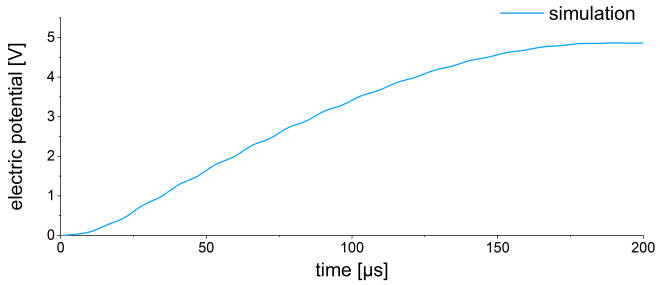

Figure 3.6.: Simulated signal at the sensor in Model 1a.

This shows that the observed form of the EME base signal originates actually from the bandwidth of the recording setup. Considering the typical temporal stages of crack growth (cf. [Sause, 2016]) in comparison with the shape of the simulated electric potential at the sensor in figure 3.6 motivates further that the base signal part of the experimentally

obtained signals rather originates from continued charge separation at the crack tip propagating in the material.
A constitutive approach in Model 1b incorporates this behaviour in terms of time-and position dependent application of charge following the hypothetical crack tip in the material.

The simulations of Model 1a in comparison with experimentally obtained data improve the understanding of effects of the experimental setup as well as the substantial influence of the measurement electronics. Unintentional effects of the experimental setup mainly suspected due to the short distance between specimen, sensor plates and acoustic sensor can be excluded based on the results of the simulation.
Careful consideration of the occurring frequencies and signal comparison with different meshes and time-steps in Model 1a form the basis for mesh and time-stepping applied in the following. We choose a resolution of the RTM6 specimen and the capacitive sensor plates with a maximum mesh element size of 0.5 [mm]. For the remaining domains we chose a element growth rate of 1.5 which ensures an adequate resolution in the area between specimen and detector and reduces the degrees of freedom in areas which do not affect the calculated field. The time-dependent calculation is conducted via Generalized-alpha-algorithm with a time-step size of 1 [μs].

Despite the good similarity of simulated and experimentally obtained signal for the selected setup, the employed source model approach of Model 1a is obviously not sufficient to reproduce the characteristics of the EME source examined in [Gade et al., 2014]. We found that a clear correlation between energy of the EME signals and detection angle is observable for both parts of the signals. While the sensor orientation in the experimental setup was fixed, the bend fixture and specimen were rotated in the (x, y)-plane, for the purpose of systematically changing the angle between crack surface and sensor plate, showing a directional field distribution in the results. The experimental results illustrate a behaviour that macroscopically rather resembles a dipole source, which cannot be reproduced by simple charge application on one crack surface. Hence, the proposed modelling approach in Model 1a is not capable of reproducing the experimentally obtained directional characteristic of the source. In Model 1b a continuative approach is chosen to overcome this major drawback of Model 1a by introducing two oppositely charged crack surfaces.

3.3. Model 1b: Time- and position-dependent charge generation on two hypothetical crack surfaces

In this consecutive approach, we focus on the component of the signal originating from charge generation at the crack tip.
The source of the EME described by ρ_{ext} is defined by opposite surface charge density $\rho(Z, t)$ and $-\rho(Z, t)$ on two hypothetical crack surfaces following the crack progress in the

material without considering the oscillating part of the signal, schematically described in figure 3.7.

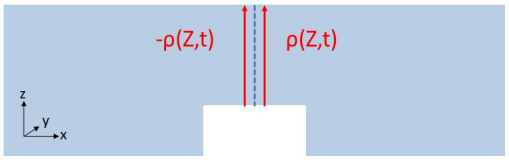

Figure 3.7.: Schematic description of Model 1b.

With this approach we aim to overcome the major drawback of Model 1a and reproduce the directional behaviour of the experimentally obtained signals.

3.3.1. Source modelling

After detailed comparative studies and consideration of charge relaxation times of the occurring materials, we decided for a further reduction of the model to the electrostatic formulation neglecting the charge relaxation process, which has insignificant effect on the obtained results.
The source of the EME modelled by ρ_{ext} is given via time- and position-dependent application of surface charge density $\rho(Z,t)$ and $-\rho(Z,t)$ on two internal boundaries of the specimen which represent the hypothetical crack surfaces. On these internal boundaries, surface charge density $\rho(Z,t)$ and $-\rho(Z,t)$ is applied following the hypothetical crack progress in the material that we deduced from the experiments. This crack progress (see figure 3.8) shows the expected typical phases of acceleration and deceleration of a crack propagating in the material (cf. [Sause, 2016]).

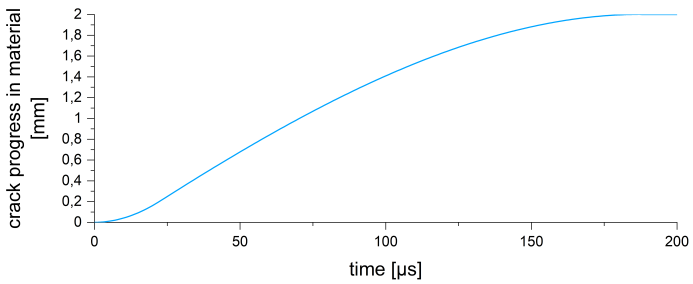

Figure 3.8.: Propagation of the crack tip in the material.

Since it is not possible to trigger the two sides of a generated internal surface separately in COMSOL Multiphysics®, we decided to apply the opposite surface charge densities on two additional internal boundaries mimicking the two crack surfaces in the material. Special care has to be taken of precise adjustment of the distance of the internal boundaries to achieve a correct effect at macro-scale. It is important to bring these as close to the hypothetical crack surface as necessary to represent the correct behaviour from a macroscopic

point of view. However, the discretization in the simulations represents a natural limit for a reasonable distance. As a result, the discretization, i.e. time step and mesh size, and the distance between internal boundaries and hypothetical crack surface must be well matched to each other.

To ensure that the simulations are able to resolve the high-frequency component of the signal which oscillates with about 80 [kHz], a time step of 1E-6[s] was chosen. When determining the mesh size at the hypothetical crack surface, one has to include the maximum speed at which a crack propagates in the material in the considerations. With a maximal crack tip velocity of about 22[m/s], which we derived from the experiments, the corresponding distance Δx that can be covered by a crack during one time step of 1E-6[s] in the simulation is 2.2E-2[mm]. Therefore, when using the mentioned time step, a mesh resolution with meshsize of at least 2.2E-2[mm] at the crack surface is required to be able to reproduce the crack growth correctly. We choose the distance of the internal boundaries to the hypothetical crack surface accordingly. These considerations resulted in a modified specimen and mesh with two additional internal boundaries with a distance of 2.2E-2[mm] to the hypothetical crack. With these settings for specimen and mesh we are able to reproduce the described behaviour of the EME source.

3.3.2. Simulation results

The modelling approach via time- and position-dependent application of charge following the crack tip in the material results in signals similar to those derived from the experiments concerning the base signal part, see figure 3.9.

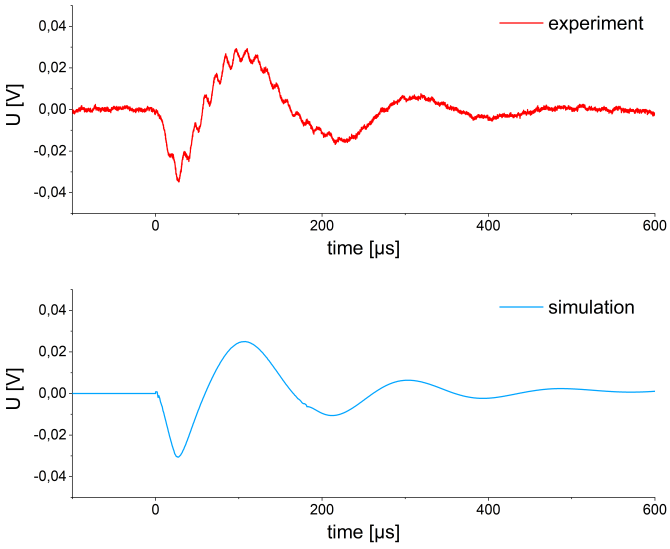

Figure 3.9.: Comparison of signal of test source experiment and simulation results of Model 1b.

Simulations are performed for three different detection angles ($\phi = 0°$, $45°$, $90°$) and different source–sensor distances according to the performed experiments as displayed in figure 3.2. In order to investigate the further characteristics of the model source, we compare the energies of the signals in experiment (full signal) and simulated signals (without vibration of crack walls), see figure 3.10. The energy of the signals obtained in the simulations is therefore scaled matching the energies of simulated and experimentally obtained signals for the 0°-position with source–sensor distance of d= 13[mm].

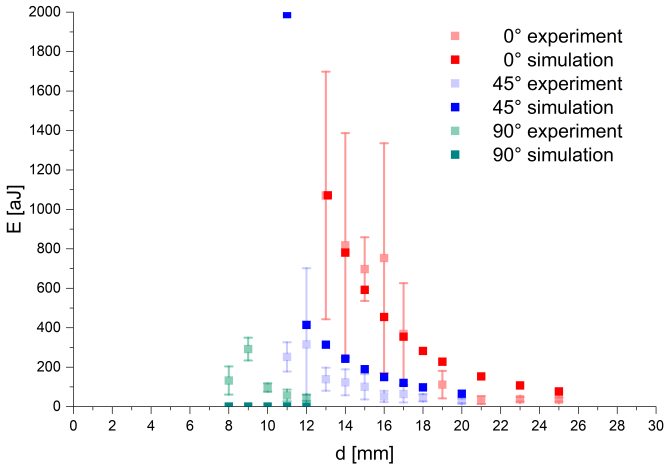

Figure 3.10.: Comparison of scaled energies of experiment and simulation for angles $\phi = 0°$, $\phi = 45°$ and $\phi = 90°$.

Whereas the energies of experimental data and simulation results show good accordance for the 0°-position we observe a deteriorating correlation for growing angle.

For a clear presentation, we show the results in Figure 3.11, 3.12 and 3.13 again separated by angle ϕ.

Comparison of the signal energies show, that the model is not able not reproduce the increasing drop of the energies in the experiment for greater angles and short source–sensor distance, suggesting that additional effects not contained in the model influence the experimentally obtained signals for short distances.

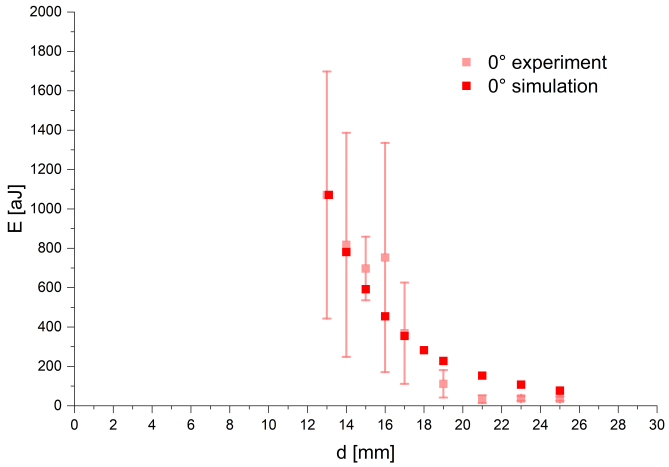

Figure 3.11.: Comparison of scaled energies of experiment and simulation for $\phi = 0°$.

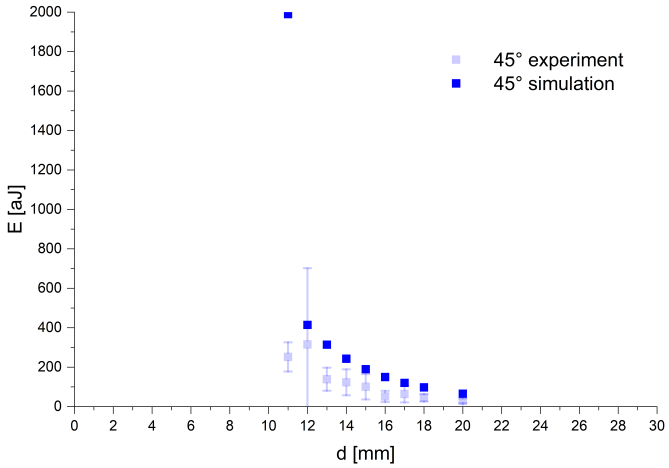

Figure 3.12.: Comparison of scaled energies of experiment and simulation for $\phi = 45°$.

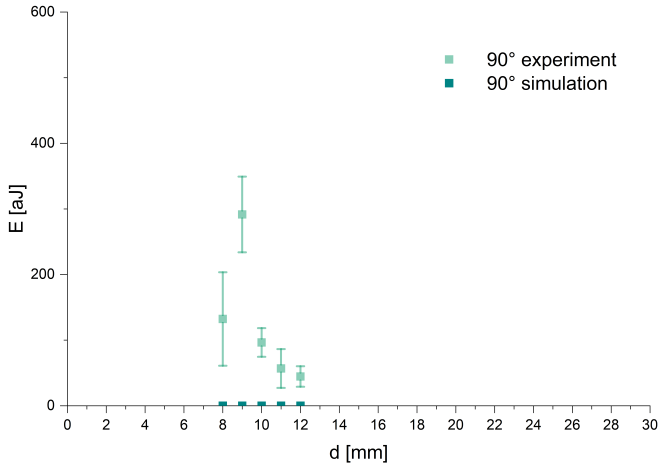

Figure 3.13.: Comparison of scaled energies of experiment and simulation for $\phi = 90°$.

The experimental data presented in [Gade et al., 2014] provides motivation for the increasing differences in the energies of experimental signals and simulation results.

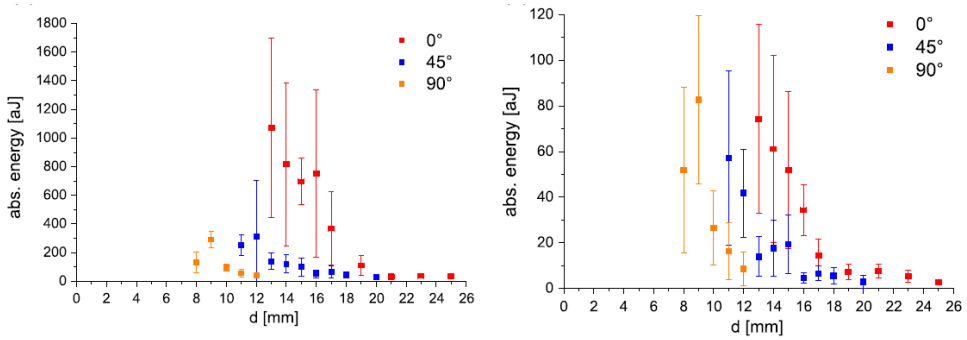

Figure 3.14.: Energies of the full signal (left) versus energies of the oscillating signal part in the experiment (right) (Graphics from: S. O. Gade et al., Relation of Electromagnetic Emission and Crack Dynamics in Epoxy Resin Materials, Journal of Nondestructive Evaluation, published 2014 by Springer Nature) [Gade et al., 2014].

Figure 3.14 reveals, that the detected energies of the base part of the signal show a stronger angular dependence than the energies of the oscillating part. Evidently the oscillating part gains importance for the total energy of the full signal for increasing angle, explaining the differences in energies between experimentally obtained signals and simulated signals, which do not contain the oscillating part of the signal.
Including the oscillating part in the modelling approach is therefore essential to describe

fully the characteristics of the energies of the emitting source. Considering the underestimation of oscillation effects in the described modelling approach, a coupling of the given model with mechanical movement of crack walls can provide further insight.
In model 2 we therefore extend the present model by the signal part originating from the crack wall vibration.

4. Model 2: Charge distribution as function of crack propagation coupled with crack wall vibration

In Model 2 we combine the developed model of chapter 3 with a controlled mechanical displacement $d(t)$ respectively $-d(t)$ of the two crack walls, as displayed in figure 4.1.

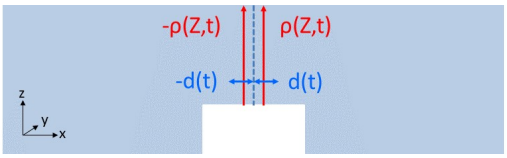

Figure 4.1.: Schematic description of Model 2.

We investigate the characteristics of the oscillation part for different angles.

4.1. Basic setup

In order to reduce the degrees of freedom and to create complete symmetry of geometry and mesh we choose a reduced setup including only RTM6 specimen and sensor plates.

The specimen resembles the Model 1b specimen, including the two inner boundaries for application of time- and position-dependent charge.

In contrast to the experimental setup, where the small copper plates differ slightly in size and position, the sensor plates are now completely symmetric in size and position, with source–sensor distance of d= 14[mm] for $\phi = 0°$ (see figure 4.2 (left)).

Specimen and sensor plates are located in the middle of a sphere mimicking an infinite space filled with air (see figure 4.2 (right)), for details see §4.2.

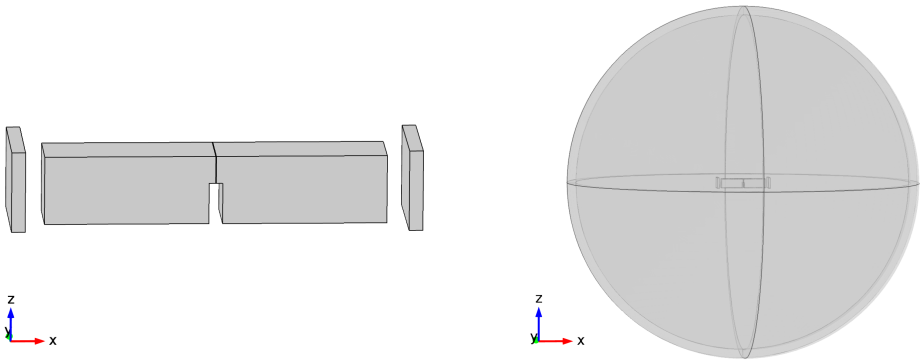

Figure 4.2.: Geometry of Model 2. Symmetric arrangement of specimen and sensor plates (left) located in a sphere (right).

In addition to the material properties for electrostatics in table 3.1 we add material properties E-modulus ($E = 2.82e9$ [Pa]), Poisson's ratio ($\nu = 0.38$) and density ($\varrho = 1140$ [kg/m^3]) for structural mechanics assuming linear elastic behaviour of the RTM6-specimen.

4.2. Source modelling

For the description of the emitted electric fields we follow the electrostatic approach with equations (2.3.22) and (2.3.23). The application of surface charge density $\rho(Z,t)$ and $-\rho(Z,t)$ on the two internal boundaries representing the crack surfaces follows the crack progress in the material as in Model 1b (see §3.3.1).

In order to model the mechanical movement of the crack walls, we include the equations of solid mechanics (see §2.3.2) with linearly elastic material model. The assigned crack surface vibration follows the oscillation $d(t)$ and $-d(t)$ on the two internal boundaries representing the hypothetical crack surfaces. The shape of the oscillation $d(t)$ pictured in figure 4.3 is deduced from the experiments and resembles the second contribution of Model 1a (see §3.2.1).

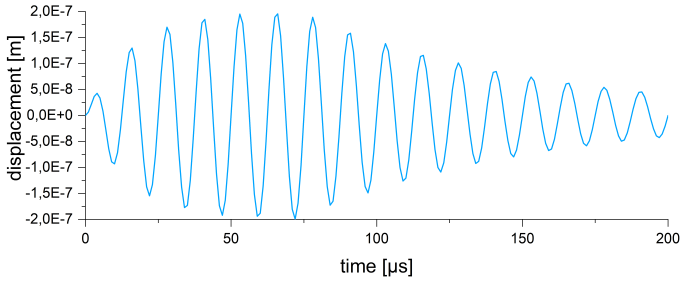

Figure 4.3.: Vibration of crack surface $d(t)$.

Due to change of the geometry and consideration of the mechanics in Model 2 we have to adapt the model additionally.
We apply an infinite element domain surrounding the air-filled sphere in a layer of 5[mm] thickness. This ensures that boundary conditions on the outside of the infinite element layer act at a very large distance from the region of interest, effectively stretching the domain to infinity. The applied default values lead to an infinite element domain that is very large compared to the geometry dimensions and with a nearly singular $1/r$ stretching of the finite elements in radial direction. [Com, 2015b]
This adjustment ensures that the calculated field is not influenced by the zero boundary condition on the surface of the surrounding sphere.
Furthermore we use the Moving Mesh interface of COMSOL Multiphysics®, which is used to study time-dependent deformations where the geometry changes its shape due to the dynamics of the problem [Com, 2015b]. In our case of a coupled structural mechanics and electrostatics approach, the moving mesh interface ensures in particular the translation between mechanical movement of the crack surfaces and charge application.

4.3. Simulation results

At first sight, simulations with additional oscillating movement of the interior boundaries representing the crack surfaces performed in the symmetric arrangement reflect approximately the findings of §3.3.2, namely a growing influence of the oscillating signal part with growing angle (see figure 4.4).
Nevertheless, analysing the simulation results from the theoretical point of view, they do not reflect the theoretically expected behaviour. In the 90° simulation we consider a geometry, which is completely symmetrical with respect to the (y, z)-plane. Modelling the EME source by the described surface charge densities $\rho(Z, t)$ respectively $-\rho(Z, t)$ and vibration of crack surfaces $d(t)$ and $-d(t)$, this should result in a signal at the sensor which is significantly small in signal strength. In fact, without numerical effects there would not be expected any signal at the sensor based on the modelled source. However, simulations calculate a signal with considerable signal strength at the sensor, which contradicts this theoretically expected result.
To explain the fundamental differences of the simulation results and expected behaviour the model was subsequently provided with a symmetric mesh in the specimen.
The results with symmetric mesh show then exactly the theoretically expected behaviour (see figure 4.5). Signals for 0° and 45° simulations agree in shape and signal strength for both simulations. In contrast to this, comparing the 90° simulations, the signal strength of the simulation with symmetric mesh is more plausible especially concerning the order of signal strength of 10^{-14} compared to 10^{-7}.
Theoretical considerations as well as the simulation results with symmetric mesh confirm that numerical effects answer for the distinct oscillating behaviour shown in figure 4.4.

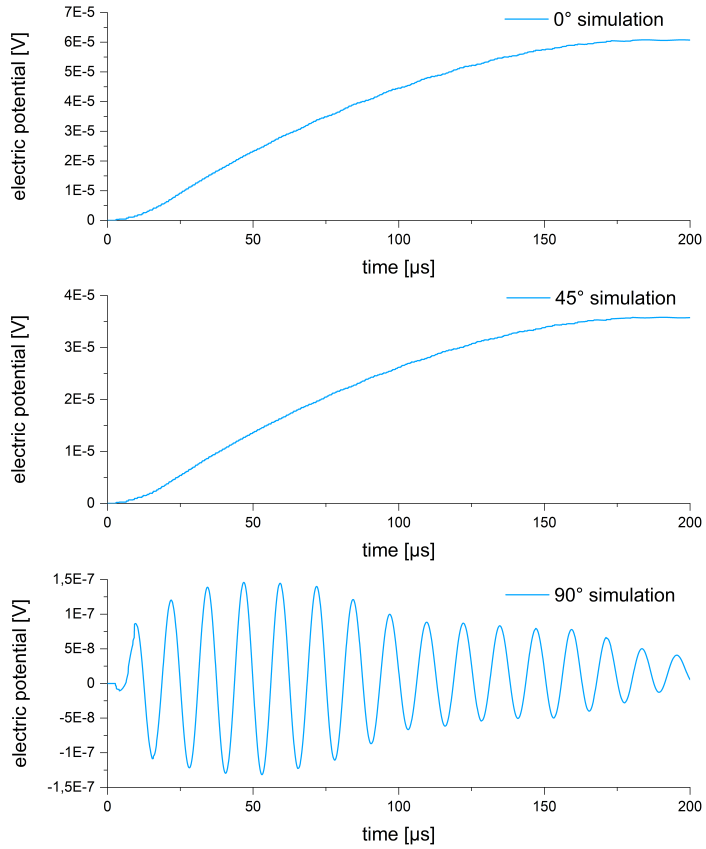

Figure 4.4.: Electric potential at the sensor for $\phi = 0°$, $\phi = 45°$ and $\phi = 90°$ in simulation with symmetric geometry.

Still, the numerical effects reproduce the behaviour witnessed in the experiments, namely the growing influence of the oscillating signal part for growing angle. The effect that small asymmetries in the mesh have great impact on the simulation results for $\phi = 90°$ indicate that in the experiments faults or asymmetries of specimen at micro-scale, asymmetric crack propagation or asymmetries in the experimental set-up, such as a slightly asymmetric sensor position, potentially have a comparably large influence on the obtained signals. We conclude that the observed behaviour of §3.3.2 is most likely due to the described effects. In Model 2 we have thus realized a source model that is able to explain and reproduce the individual components of the signals measured in the experiment. We are able to reproduce the basic directional character of the source. In the last step we succeeded in explaining the growing importance of the oscillating signal component for increasing angles.

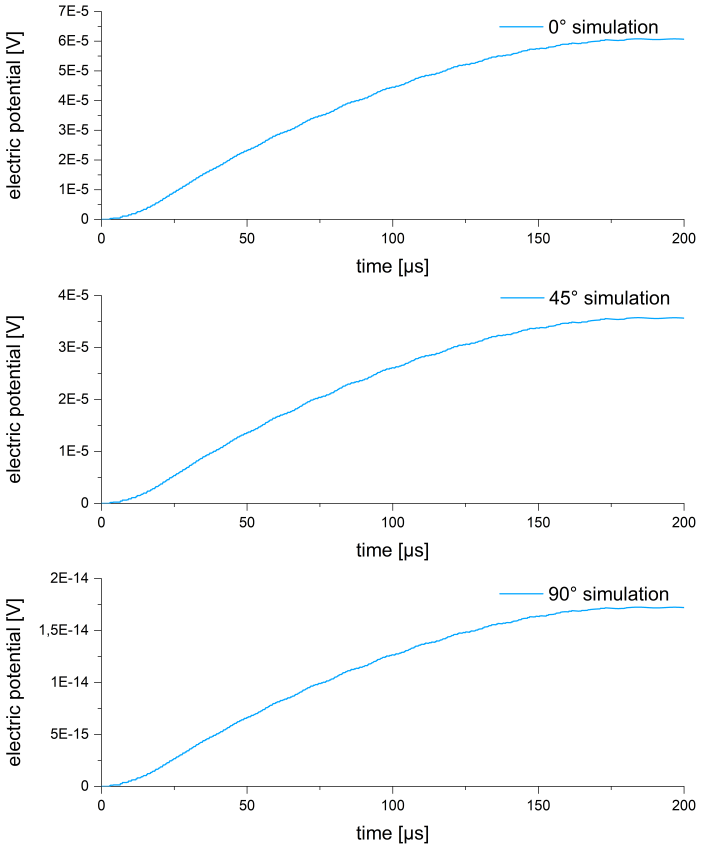

Figure 4.5.: Electric potential at the sensor for $\phi = 0°$, $\phi = 45°$ and $\phi = 90°$ in simulation with symmetric geometry and mesh.

5. Summary and outlook

Modelling and simulation of the EME source provided an important contribution to understanding the experimental setup, the sensor system and in particular the different contributions of the EME source.
With our proposed and implemented source model we are capable of explaining and reproducing the different contributions and the directional behaviour of the EME source. We motivated further the origin of the superimposed oscillation of the signal and deduced a deeper understanding of the angular dependence of the oscillation. The so far derived results strengthen our hypothesis of the basic origins of the EME, namely the base signals originating from generation and relaxation of charges and the superimposed oscillation due to mechanical movement of the crack surfaces.
Despite the extensive study of the topic and the evident progress, there are still open questions.
Most notably the question is still open as to which processes lead to generation of opposite charge ratio on the crack surfaces.
We achieve good compatibility of the implemented source model and the experimentally obtained characteristics of the source. Nevertheless, the possible influence of further effects, for example additional effects caused by surface waves introduced by Frid in [Frid et al., 2003] not yet contained in the source model should not be disregarded and should be of further interest.
Due to the weak influence of charge migration for the material under consideration, we moved to a quasi-static approach in Model 1b, which does not include conductivity and thus the contribution of charge relaxation. Following the source-model hypothesis, this signal component becomes more important for materials with higher conductivity. Latest experimental results with superconductors show the emergence of signals similar to those observed in the experiments with RTM6-specimens. However, based on the presented model hypothesis, the relaxation should be so fast that detection of EME signals would not be possible. Consequently, if one wants to adhere to the hypothesis of charge generation at the crack tip due to breakage of molecular bonds, the relaxation due to conductivity of the material is somehow prevented. In order to understand the mechanisms involved in more detail, modelling at micro-level would be required which is beyond the scope of this work, but should be addressed in future work.

Part II.

An approach to sensor optimization via the homogenization method

The question of optimal shape and position of the EME sensor in the experiments motivated the second part of this work. Up to now, the design of the sensor system has been based completely on the experience of the scientists.
The experiments give rise to various questions related to sensor construction. Relevant questions are, first of all, the question of the optimal design to maximise the signal voltage at the sensor or to minimize the sensitivity with respect to inaccuracy in position of the sensor. In the experiment described, one is also interested in analysing the influence of other components, such as the grounded AE sensor in close proximity on the optimal design of the EME sensor or whether there is mutual interference when several sensors are used. The observed directional character of the source also raises the question whether for example the position of fracture surfaces in a material can be determined by using sensor arrays to detect the signal from several directions.
Theoretically dealing with the topic of sensor optimization and deriving an optimization procedure enables the simple testing of hypotheses in connection with the questions mentioned above. In Part II of this thesis we use and extend the method of **shape optimization via homogenization** to approach the topic of sensor optimization in the described context. It turns out that extension of the well-known theory of shape optimization via homogenization for material parameters in $\mathbb{R}$ to material parameters in $\mathbb{C}$ is necessary in order to apply the theory to questions in the context of the given setting.

Part II of this work is structured as follows.
In Chapter 6, we place the question of optimal sensor design in the context of topology optimization and explain why an extension of the theory to complex-valued material parameters is necessary. Chapter 7 introduces the well-known theory of shape optimization via homogenization with material parameters in $\mathbb{R}$. The chapter forms the basis for the extensions in the subsequent chapters. In chapter 8, we introduce implementation aspects and extension of the method to optimization in subdomains and optimization in 3d in order to make the homogenization method useful in the given context of sensor optimization. Chapter 9 examines the extension of the method to complex-valued material parameters. Despite the problems arising, an optimization procedure is provided at the end of the chapter, which forms the basis for further application. Finally, in chapter 10 we apply the derived method to questions arising in the context of sensor optimization in the described experiments. Chapter 11 concludes by summarising the findings of Part II.

In the following, we make use of standard notation concerning function spaces, an introduction to the relevant concepts can be found for example in [Alt, 2012]
Let Ω be an open set in $\mathbb{R}^N$. We denote by $L^p(\Omega)$, $p \in [1, \infty)$ the space of all p-integrable functions u in Ω with

$$\|u\|_{L^p(\Omega)} = \left(\int_\Omega |u(x)|^p \, \mathrm{d}x \right)^{1/p}$$

and by $L^\infty(\Omega)$ the space of all essentially bounded functions with

$$\|u\|_{L^\infty(\Omega)} = \operatorname{ess\,sup}_{x \in \Omega} |u(x)|.$$

For a sequence of functions $(u_n)_{n \in \mathbb{N}}$ we write (u_n) and denote the strong convergence by

$$u_n \to u \text{ in } L^p(\Omega),$$

as usual we denote the weak convergence by

$$u_n \rightharpoonup u \text{ in } L^p(\Omega),$$

respectively the weak* convergence for $p = \infty$.
The Sobolev space containing p-integrable functions with p-integrable weak derivatives up to order k is denoted by $W^{k,p}(\Omega)$, and we write $H^k(\Omega) := W^{k,2}(\Omega)$.
$H_0^1(\Omega) = W_0^{k,2}(\Omega)$ is accordingly the Sobolev space with zero boundary conditions:

$$W_0^{k,2}(\Omega) = \{f \in W^{k,2}(\Omega) | \exists f_n \in C_0^\infty : \|f - f_n\|_{W^{k,2}} \to 0 \text{ for } n \to \infty\}$$

And we denote by $H^{-1}(\Omega)$ the dual space of $H_0^1(\Omega)$.

For $z = a + \mathrm{i}b$ we denote by $\Re(z)$ the real part $\Re(z) = \Re\{a + \mathrm{i}b\} = a$ and by $\Im(z)$ the imaginary part $\Im(z) = \Im\{a + \mathrm{i}b\} = b$ and employ the following definition of the complex scalar product $\langle \cdot, \cdot \rangle$:

$$\langle x, y \rangle := x^T \bar{y},$$

linear in the first variable, conjugate linear in the second variable (sesquilinear), symmetric and positive definite.

6. Optimal design in conductivity

The question of the optimal sensor design in the presented context can be mathematically formulated as a **two-phase optimization problem**, in which a fixed proportion of two different materials (here: air and copper) is distributed in a given domain in such a way that a given objective function (here: the energy captured by the sensor) is maximized.
In the framework of two-phase optimization, one typically considers two materials (phases), which differ substantially in their material parameters (such as for example thermal conductivity, strength or electrical conductivity), an underlying physics (such as stationary heat conduction, structural mechanics or electrostatics) described by a partial differential equation with corresponding boundary conditions, and an objective function measuring the quality of the distribution of the two materials in a given domain. Well-known examples of two-phase optimal design are, for example, the question of finding the best way of mixing two elastic materials in order to yield the most rigid structure or finding the best arrangement of two thermally conductive materials in order to find the best insulating design [Allaire, 2002].
There are different methods to approach the above mentioned type of optimal design problems. In §6.1, we give a short introduction to the topic of topology optimization approaches and put the design problem of interest and the method of relaxation via homogenization into this context. In §6.2, we derive the underlying partial differential equation for the presented problem of sensor optimization and, in §6.3, we explain our procedure in approaching the problem of interest considered as a problem of optimal design in conductivity.

6.1. Topology optimization approaches

In the following we provide a short introduction to the topic of topology optimization. In view of the variety of methods in this field, this aggregation is far from complete but aims at a coarse classification of the problem of optimal sensor design and the homogenization method in this context. The summary subsumes information of the reviews [Sigmund and Maute, 2013], [Deaton and Grandhi, 2014] and of [Allaire, 2002, Preface] and [Bendsœ, 1995].
Following Bendsøe [Bendsœ, 1995, p.5] and [Deaton and Grandhi, 2014] there exist mainly three aspects of optimal design namely **sizing**, **shape optimization** and **topology optimization**.
Sizing Problems usually deal with single design variables. The most popular example

is the thickness distribution of a linear elastic plate. **Shape optimization problems** address the task of finding the optimal shape of a predefined structural configuration. This is especially useful when the basic structure of an object is already determined and the optimization process should only fine-tune the given shape according to the structural use of the object. **Topology optimization problems** additionally allow for determination of number and location of holes in a given design domain and for connectivity of the domain. Therefore, topology optimization covers all aspects of design optimization including size and shape optimization problems and is the method of choice especially in the early stage of design, when all aspects, sizing, shape and topology are of general interest and can significantly affect the performance of a structure.
Since we do not want to restrict the optimization to a predefined structure the presented problem of sensor optimization can be classified as a typical topology optimization problem. Figure 6.1 summarizes different possibilities to approach optimal design problems, which are described in the following.

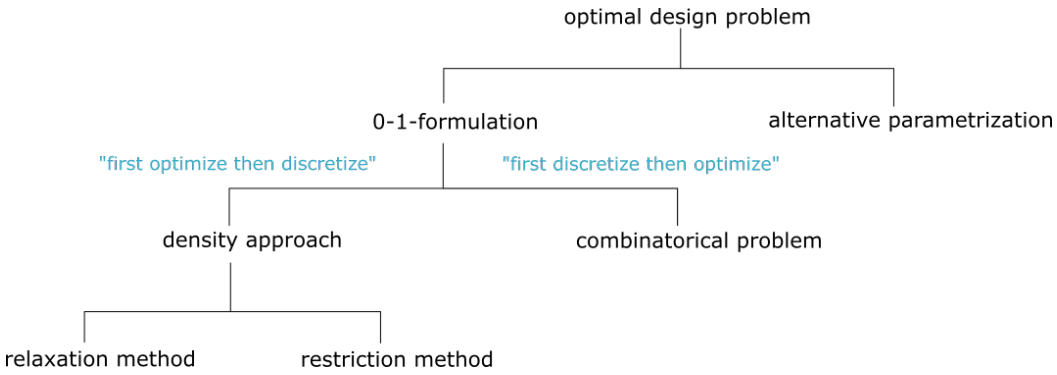

Figure 6.1.: Overview of approaches to optimal design.

One possibility to address topology optimization problems is to consider formulations of the optimal design problem for example in terms of the boundaries of an existing component whose design is to be optimized. These parametrizations describe a typical shape optimization problem. Therefore, the applied methods have to ensure the possibility of creation of new holes to transform from shape optimization algorithms to topology optimization algorithms [Sigmund and Maute, 2013].
The so-called **0-1-formulation** of the optimization problem, also sometimes called the material formulation of the problem, determines for every point in the design space if there is material (1) or not (0), respectively if there is material A (1) or B (0). A formulation of the optimal sensor design as a two-phase problem, as described above, can be assigned to this category.

According to the principle "first discretize, then optimize" the original continuous optimal

design problem in 0-1-formulation can be discretized and formulated as a discrete combinatorial problem. The corresponding methods work on a fixed FEM mesh and are based on either the mesh elements or the mesh nodes. The practicability of this approach is often determined by the number of variables involved. [Sigmund and Maute, 2013]

Alternatively, one follows the principle "first optimize and then discretize" and first analytically derives the necessary optimality criteria for the continuous problem. Regarding the 0-1-approach, one has to notice that in absence of any additional constraints such as for example perimeter constraints limiting the perimeter of the derived shape, a minimal length-scale or a maximum number of components, the optimization problem usually does not admit a solution in the set of admissible 0-1-designs. This is plausible also from a practical point of view: A structure with many tiny inclusions of holes often has better properties than a structure with few small holes of the same total volume, which means that every proposed design can be improved by making further variations of the phase arrangement. The optimal design problems in 0-1-formulation are not well-posed and in general do not admit classical design solutions (0-1-solutions). As a result, it is not possible to derive necessary optimality criteria in the 0-1-formulation. [Allaire, 2002]

There are two ways to obtain the well-posedness of the optimization problem and thus enable the formulation of optimality criteria, both of them involve the introduction of a material density instead of dealing with discrete values 0 and 1.

Restriction methods allow for intermediate values of a density linked to the material parameters as design variables, usually without giving them a physical meaning at the beginning, even though in some cases a physical justification can be provided afterwards. At the same time, the methods penalize intermediate values in order to obtain a design consisting only of 0-1-values. Other approaches work for example with explicit penalization. [Sigmund and Maute, 2013]

In **relaxation approaches**, the set of admissible designs in the 0-1-formulation, containing the two materials is extended (relaxed) to an appropriate closure of the space of admissible designs, allowing for composite materials with their effective material properties. Once the continuous relaxed problem setting is derived, this enables derivation of necessary optimality conditions and formulation of optimization methods based thereupon. In contrast to restriction methods, a penalization process to regain a 0-1-formulation in the end is undertaken once the optimal design in the relaxed admissible set is found. It has to be noted that, unlike some restriction approaches, intermediate density values gain a physical meaning as composite materials and that the effective parameters do not only depend on this density, i.e. the proportion of materials, but in addition on the underlying microstructure. The theory of H-convergence presented in chapter 7 of this thesis is the basis for the method of **relaxation via homogenization** by which we approach our problem of sensor optimization.

6.2. Equations of electrostatics in dielectric and conductive media

In Part I of the present work, the equations of electrostatics in dielectric materials are supplemented by corresponding boundary conditions, i.e. a floating potential boundary condition on the sensor surfaces, in order to model effects of conductive materials assuming that the materials are perfect conductors (cf. §2.3.1).
In order to formulate the problem of optimal sensor design as a two-phase optimization problem, both, dielectric and conductive properties of the materials have to be reflected in the equations by the material parameters and not via additional boundary conditions. Only then does the formulation of the optimal sensor problem fit into the framework of the well-known theory of homogenization via relaxation. For this goal we adapt the corresponding equations in the frequency domain. The equations of electrostatics are still used for modelling, but the effects of both dielectric and conductive materials are now included by a complex-valued material constant without any additional boundary conditions. By this approach, we modify the modelling equations of the application in a way that enables further consideration of the problem of sensor optimization in the described framework of the homogenization method.

Referring to the description of §2.3.1 and following the argumentation in [Bartelmann et al., 2018], the macroscopic equation describing the sources of the electric field is described by superposition of two contributions of charge densities: ρ_b, charge density arising from charge carriers bound in the material and ρ_f, the charge density of free charges. Further, one can subclassify the free charge density into ρ_c and ρ_{ext}. In conducting materials, free charge carriers of the material subjected to an external electric field contribute to the free charge density by ρ_c, load carriers introduced into the system from external sources are subsumed by the external charge density ρ_{ext}:

$$\nabla \cdot (\epsilon_0 E) = \rho \tag{6.2.1}$$
$$= \rho_f + \rho_b \tag{6.2.2}$$
$$= \rho_{ext} + \rho_c + \rho_b. \tag{6.2.3}$$

6.2.1. Electric field in dielectric materials

An external electric field applied to a dielectric material shifts bound charges on atomic or molecular scale, forming electrical dipoles. Polarization P, the average dipole charge density, takes these effects into account on macroscopic level:

$$\rho_b = -\nabla \cdot P. \tag{6.2.4}$$

Assuming homogeneous isotropic linear dielectric materials, polarization is proportional to the electric field with constant of proportionality χ, which is called electrical susceptibility of the material. In §2.3.1 of Part I we considered slowly vaying fields resulting in equation (2.3.14). Taking into account that the response of the medium to the applied electric field is not instantaneous we get

$$P(t) = \epsilon_0 \int_{-\infty}^{t} \chi(t - t')E(t')\,\mathrm{d}t', \tag{6.2.5}$$

what leads to

$$P(\omega) = \epsilon_0 \chi(\omega)E(\omega) \tag{6.2.6}$$

in the frequency domain.

Accordingly equation (6.2.3) transforms to

$$\nabla \cdot (\epsilon_0(1 + \chi(\omega))E(\omega)) = \rho_{ext} + \rho_c. \tag{6.2.7}$$

The function $1 + \chi(\omega)$ describing the properties of the material due to bound charges is often subsumed as relative electric permittivity $\epsilon_r(\omega) = 1 + \chi(\omega)$:

$$\nabla \cdot (\epsilon_0 \epsilon_r(\omega)E(\omega)) = \rho_{ext} + \rho_c. \tag{6.2.8}$$

In general ϵ_r is complex-valued $\epsilon_r = \epsilon_p' + \mathrm{i}\epsilon_p''$, accounting for refraction and absorption of the propagating electromagnetic wave in the dielectric material due to polarization effects by the real respectively imaginary part ([Orfanidis, 2019]).

In order to examine the behaviour of the material parameter ϵ_r for the low-frequency limit $\omega \to 0$, we need to deepen the understanding of this material parameter. For this purpose, one considers a simplified model of the motion of bound electrons in the presence of an applied field (see for example [Orfanidis, 2019], [Bartelmann et al., 2018] or [Jackson, 2006]).

Based on Newton's law and the idea that in general an electron is prevented from following the electric field unhindered by being tied to its nucleus with a spring-like force on the one hand and by friction forces arising from collisions proportional to the velocity on the other hand one deduces

$$m\ddot{x} = eE - kx - m\gamma\dot{x}, \tag{6.2.9}$$

with mass m and phenomenological parameters which resemble a spring constant k, resonance frequency $\omega_0 = \sqrt{km}$ of the spring and rate of collisions per unit time $\gamma > 0$.

Considering harmonic oscillating electric fields with frequency ω ($E(t) = Ee^{-\mathrm{i}\omega t}$) in materials with bound electrons it is possible to deduce from this simple model the relative

permittivity

$$\epsilon_r(\omega) = 1 + \frac{\omega_p^2}{\omega_0^2 - \omega^2 - \mathrm{i}\omega\gamma}, \tag{6.2.10}$$

with $\omega_p = \frac{N_b e^2}{\epsilon_0 m}$ the so-called plasma frequency, ω_0 resonance frequency, γ collision rate of the material.

This model describing the relative permittivity is called Lorentz-oscillator-model (cf. [Bartelmann et al., 2018]) or Lorentz dielectric (cf. [Orfanidis, 2019]).

With equation (6.2.10) we are able to deduce the behaviour of the material parameter in the low-frequency limit, which is then called **nominal dielectric constant** with purely real part:

$$\epsilon_r(0) = 1 + \frac{\omega_p^2}{\omega_0^2}. \tag{6.2.11}$$

6.2.2. Electric field in conductive media

Free charge carriers of conductive materials subjected to an external electric field contribute to the free charge density by ρ_c. The time-varying charge density ρ_c is the source for a related current J_c:

$$\frac{\mathrm{d}}{\mathrm{d}t}\rho_c(t) = -\nabla \cdot J_c(t) \tag{6.2.12}$$

leading to

$$(-\mathrm{i}\omega)\rho_c(\omega) = -\nabla \cdot J_c(\omega) \tag{6.2.13}$$

in the frequency domain, considering again harmonic oscillating fields with frequency ω ($E(t) = Ee^{-\mathrm{i}\omega t}$).

Including Ohm's law ($J_c = \sigma E$) in the deduced equation, we get

$$\rho_c(\omega) = \nabla \cdot (\frac{1}{\mathrm{i}\omega}\sigma(\omega))E(\omega) \tag{6.2.14}$$

with complex-valued frequency-dependent conductivity $\sigma(\omega)$.

As in §6.2.1 a model based on equation (6.2.9)

$$m\ddot{x} = eE - kx - m\gamma\dot{x} = eE - m\gamma\dot{x}, \tag{6.2.15}$$

provides a deeper understanding of the parameter σ. In the case of free charge carriers an electron is not bound to its position, which is phenomenologically expressed by $k = 0$ respectively $\omega_0 = 0$.

Considering again harmonic oscillating fields with frequency ω it is possible to deduce the conductivity

$$\sigma(\omega) = \frac{\epsilon_0\omega_p^2}{\gamma - \mathrm{i}\omega} \tag{6.2.16}$$

with plasma frequency $\omega_p = \frac{N_b e^2}{\epsilon_0 m}$. The model defined by (6.2.16) is called Drude model

[Orfanidis, 2019].
In the low-frequency limit, $\sigma(\omega)$ reduces to the **nominal real-valued conductivity** σ.

6.2.3. Electric field in general media

Based on equation (6.2.8) and (6.2.14), we deduce

$$\nabla \cdot (\epsilon_0 + \epsilon_0\chi(\omega) - \frac{1}{\mathrm{i}\omega}\sigma(\omega))E(\omega) = \rho_{ext}. \tag{6.2.17}$$

in general media with bound and unbound charge carriers.
We combine further the polarization and conductive effects of materials in one generalized complex-valued material parameter $\epsilon = \epsilon' + i\epsilon''$, called the total effective permittivity [Orfanidis, 2019]

$$\epsilon(\omega) = \epsilon_0 + \epsilon_0\chi(\omega) - \frac{1}{\mathrm{i}\omega}\sigma(\omega) \tag{6.2.18}$$

leading to

$$\nabla \cdot (\epsilon(\omega)E(\omega)) = \rho_{ext}. \tag{6.2.19}$$

Equation (6.2.17) respectively (6.2.19) describe the propagation of the electric field in general media with bound and unbound charge carriers. The real part of the total effective permittivity leads to refraction, the imaginary part to absorption of the electromagnetic wave in the material.
As described, the material parameter ϵ combines properties of the material that are due to bound and unbound charge carriers in the material. For frequencies $\omega \neq 0$, the real and imaginary parts account for refraction and absorption of the electromagnetic waves, but since both, real and imaginary part, generally consist of the two components arising from bound and unbound charge carriers they do not allow a direct interpretation as dielectric properties or conductivity of the material. As described, a direct connection between conductivity of the material and the imaginary part of the material parameter can only be established for the low-frequency limit $\omega = 0$.
In the application, we therefore consider the parameter ϵ purely phenomenologically. By means of a larger imaginary part in the sensor material compared to the surrounding material, we enforce a stronger absorption of the field in the sensor.

6.2.4. Equations of electrostatics in general media

In the application, we consider the time-harmonic case for low frequencies ω. In the experiments on which the application is based, the measuring technique is not suitable for measuring magnetic effects. Therefore, we neglect inductive effects in the model. Equation (6.2.19) in combination with description of the electric field as gradient of a scalar electric

potential V leads to the following equations to be solved for V:

$$E(x,\omega) = -\nabla V(x,\omega) \tag{6.2.20}$$

$$-\nabla \cdot (\epsilon(\omega)\nabla V(x,\omega)) = \rho_{ext}. \tag{6.2.21}$$

As described above, the parameter ϵ summarises the contributions due to bound and unbound charge carriers in the material, application of additional boundary conditions in order to model conducting materials as in Part I of this work is no longer necessary.
These equations of electrostatics in general media provide the basis for consideration of the described optimal design problem as a two-phase optimization problem in the context of the homogenization method.

6.3. Relaxation via homogenization

In the following, we briefly outline the idea of how we approach the problem of sensor optimization within the framework of the theory of relaxation via homogenization.
Based on the deduced equations (6.2.20) and (6.2.21) we are interested in the optimal distribution of two materials A (the sensor material) and B (the air) with complex-valued material parameters $\alpha, \beta \in \mathbb{C}$ in a given domain Ω subject to an objective function such as for example the energy measured at the sensor. We proceed as follows: first, we describe the well-known theory of the homogenization method for two-phase design problems with material parameters $\alpha, \beta \in \mathbb{R}$. In order to enable 3d optimization with optimization of the material distribution only on a subdomain, we extend the existing method afterwards. In a further step, we examine the problems involved in extending the method of relaxation via homogenization to complex-valued parameters $\alpha, \beta \in \mathbb{C}$. Despite the problems that arise, certain restrictions still allow the derivation of a optimization method for the complex-valued case which we finally apply in several examples.

7. Homogenization method with real-valued material parameters

This chapter presents the basic concepts of the homogenization method applied to two-phase optimization for material parameters $\alpha, \beta \in \mathbb{R}$. The reader obtains a summary of the important concepts following the contents of [Allaire, 2002] and the structure of [Allaire and Castro, 2001].

The chapter provides the theoretical basis for discussion and extension of the existing theory and method in chapters 8 and 9.

§7.1 provides a short introduction of the setting of the problem. We are interested in the optimal distribution of two isotropic phases A and B of fixed volume in a given domain Ω, such that a given criterion, which depends on the solution of an underlying state equation in Ω, is minimized. In general, this described optimization problem is ill-posed and does not admit a solution in the set of admissible designs. To overcome this drawback, we enlarge the set of admissible designs by allowing for composite materials with their effective (macroscopic) parameters deduced by the homogenization process. This procedure described in §7.2 is called relaxation via homogenization. Given the relaxed problem and the corresponding directional derivative of the objective functional in §7.3, necessary optimality conditions are deduced in §7.4, which provide the basis for the optimality criteria method in §7.5 and the gradient method described in §7.6.

7.1. Setting of the problem

We consider the problem setting as described by Allaire in [Allaire, 2002].

Based on the distribution of two materials A and B with constant isotropic material parameters α respectively β (α, $\beta \in \mathbb{R}$, $0 < \alpha < \beta < +\infty$) in a given domain Ω (bounded open set in $\mathbb{R}^N$), see figure 7.1, the characteristic function

$$\chi(x) = \begin{cases} 1 & \text{phase } A \text{ is present at point } x \\ 0 & \text{phase } B \text{ is present at point } x \end{cases} \tag{7.1.1}$$

defines the part of Ω occupied by phase A.

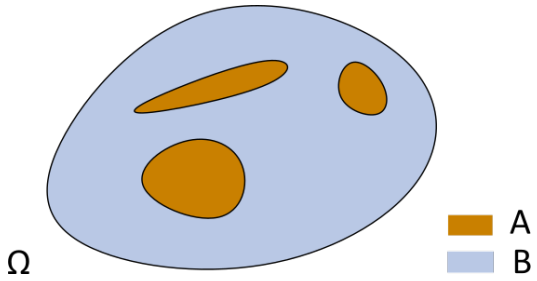

Figure 7.1.: Two-phase domain Ω filled with material B with inclusions of material A.

Hence, the overall material parameter a_χ in Ω is formulated as

$$a_\chi(x) = \alpha\chi(x) + \beta(1 - \chi(x)). \tag{7.1.2}$$

The **state equation** of our optimization in the domain Ω reads

$$\begin{cases} -\mathrm{div}(a_\chi(x)\nabla u_\chi(x)) = f(x) & \text{in } \Omega \\ u_\chi(x) = 0 & \text{on } \partial\Omega, \end{cases} \tag{7.1.3}$$

where u_χ is the unknown function and f a given source term in Ω, which is scalar and independent of χ. The materials A and B are assumed to follow a linear material law and are perfect bonding, which guarantees perfect transmission conditions at the phase boundaries.

Provided that the source term f belongs to $H^{-1}(\Omega)$ we deduce, that the standard weak form of (7.1.3) admits a unique solution u_χ in $H_0^1(\Omega)$ (cf. §7.1.1).

We are interested in the optimal distribution of the two phases subject to an objective functional depending on the solution of the state equation and assume further that the amount of material A is limited by a prescribed volume V_α of A, $0 \leq V_\alpha \leq |\Omega|$, $|\Omega|$ measure or volume of Ω.
An **admissible design** is therefore a function χ such that

$$\chi \in L^\infty(\Omega; \{0, 1\}) \text{ and } \int_\Omega \chi(x)\,\mathrm{d}x = V_\alpha. \tag{7.1.4}$$

We denote by U_{ad} the **set of admissible configurations**:

$$U_{\mathrm{ad}} = \left\{ \chi \in L^\infty(\Omega; \{0; 1\}) \text{ such that } \int_\Omega \chi(x)\,\mathrm{d}x = V_\alpha \right\}. \tag{7.1.5}$$

The quality of the arrangement of material A and B in the domain Ω is measured by an

objective functional formulated as

$$J(\chi) = \int_\Omega [\chi(x) g_\alpha(x, u_\chi(x)) + (1 - \chi(x)) g_\beta(x, u_\chi(x))] \, \mathrm{d}x, \tag{7.1.6}$$

where g_α and g_β are sufficiently smooth Caratheodory functions satisfying suitable growth conditions in order to ensure well-posedness of the later derived relaxed optimization problem (cf. §7.1.2).
In the following, we refer to this setting with two isotropic materials with real-valued material parameters as **real-valued parameter setting**. Furthermore we follow the diction in literature (see §6.1) and refer to the described optimization problem as **0-1-problem** respectively the problem setting as **0-1-setting**.
At this point it must be noted further that here and in the following we follow the notation of [Allaire, 2002], where the described objective functional is denoted by $J(\chi)$. However, the state variable u is still contained in the objective function, which formally results in $J(\chi, u)$. A derivation of the formally reduced objective functional $J(\chi)$ by means of a control-to-state operator as described for example in [Tröltzsch, 2009] is not necessary here. Nevertheless, the dependence on the state u must be taken into account again when computing the directional derivative.

Instead of enforcing the volume constraint $\int_\Omega \chi(x) dx = V_\alpha$ in the set of admissible designs, we introduce a Lagrange Multiplier $l \in \mathbb{R}$ in the objective functional, following the general procedure of eliminating constraints in the calculus of variations ([Tröltzsch, 2009]):

$$J(\chi) = \int_\Omega [\chi(x) g_\alpha(x, u_\chi(x)) + (1 - \chi(x)) g_\beta(x, u_\chi(x))] \, \mathrm{d}x + l \int_\Omega \chi(x) \, \mathrm{d}x.$$

For any value of l, there is a corresponding volume constraint such that the optimization problems are equivalent. Even if the converse assumption is generally not clear, we can couple an optimization routine with a bisection method to update the Lagrange Multiplier to ensure the abidance by the volume constraint in practice (see §8.1 for details).
In the following, we formulate the theory based on the described problem with fixed Lagrange Multiplier l. The complete formulation of our optimal design problem is then stated as:

Find $\tilde{\chi}$ such that

$$\tilde{\chi} = \operatorname*{arg\,inf}_{\chi \in L^\infty(\Omega; \{1;0\})} J(\chi) \tag{7.1.7}$$

where the objective functional J is defined by

$$J(\chi) = \int_\Omega [\chi(x) g_\alpha(x, u_\chi(x)) + (1 - \chi(x)) g_\beta(x, u_\chi(x)))] \, \mathrm{d}x + l \int_\Omega \chi(x) \, \mathrm{d}x, \tag{7.1.8}$$

and u_χ is the solution of the state equation

$$\begin{cases} -\mathrm{div}(a_\chi(x)\nabla u_\chi(x)) = f(x) & \text{in } \Omega \\ u_\chi(x) = 0 & \text{on } \partial\Omega. \end{cases} \tag{7.1.9}$$

When searching for an optimal design the following two questions are of interest: does the problem admit a (unique) solution in the set of admissible designs and what are the associated optimality conditions.
Commonly, the direct method of the calculus of variations provides the tool to answer these questions. But besides knowledge of several counterexamples to the existence of optimal designs in the described 0-1-setting (see for example [Allaire, 2002] for a simple counterexample), one can imagine that a minimizing sequence of nearly optimal designs may generate an increasingly finer mixture of the two separate materials leading to effective material parameters which differ from the ones of the individual phases.
An adjustment of the problem formulation to a so-called **relaxed problem setting** can guarantee the existence of solutions and enable the derivation of optimality conditions:
Extending the space of admissible designs allowing for composite/homogenized designs and adapting the objective function appropriately is called **relaxation**. The new admissible design set U_{ad}^* considered in the relaxed problem corresponds to an extension of U_{ad} by the above mentioned "limit materials", i.e. the microscopic mixtures of the two original constituents by means of composite material tensors. With this adjustment and appropriate adaption of the objective functional to a relaxed formulation J^*, it is possible to employ the direct method of the calculus of variations. In order to justify the method of relaxation via homogenization, it must additionally be verified that the relaxed problem still describes the original physical problem.

7.1.1. Solution of the state equation

The standard weak form of state equation (7.1.9) admits a unique solution $u_\chi \in H_0^1(\Omega)$ by coercivity of a_χ and application of Lax–Milgram theorem and Riesz representation theorem.

7.1.2. Direct method of the calculus of variations

The direct method of the calculus of variations usually provides the tool to answer the question of solution and optimality conditions of a minimization problem. The general procedure as described in [Kielhöfer, 2010] is summarized in the following.
Starting from an objective functional J with finite infimum $m > -\infty$, there exists a

minimizing sequence $(y_n) \subset U_{\text{ad}}$ such that

$$\lim_{n\to\infty} J(y_n) = m.$$

Assume there exists a subsequence (y_{n_k}) of (y_n) which converges to y_∞

$$\lim_{n\to\infty} (y_{n_k}) = y_\infty. \tag{7.1.10}$$

Provided that the objective functional J is continuous or at least lower semi-continuous, i.e.

$$\lim_{n\to\infty} x_n = x_\infty \Rightarrow \lim_{n\to\infty} J(x_n) = J(x_\infty) \text{ (continuity)}$$

respectively

$$\lim_{n\to\infty} x_n = x_\infty \Rightarrow \liminf_{n\to\infty} J(x_n) \geq J(x_\infty) \text{ (lower semi-continuity)},$$

it follows hat y_∞ is minimizer of J. On this basis, one differentiates the objective functional in order to derive optimality conditions.

In summary, successful application of the principle requires on the one hand convergence of a subsequence of a minimizing sequence and on the other hand the continuity respectively lower semi-continuity of the objective functional, both regarding an appropriate concept of convergence.

Based on this description of the general procedure we come back to the problem of interest with $y_n = \chi_n$ and summarize the problems that arise in the present context following the argumentation of [Allaire, 2002]. First of all, the question arises as to which concept of convergence (weak, strong convergence) the convergence of the subsequence (7.1.10) is considered. By uniform boundedness of the characteristic functions $\|\chi_n\|_{L^\infty(\Omega)} \leq 1$ one can deduce existence of a subsequence (χ_{n_k}) that converges weakly* to a limit χ_∞. Weak convergence is therefore the appropriate tool for studying the sequence (χ_n).

Trying to perform the direct method of the calculus of variations in the context of optimal 0-1-design there arise two main problems:

Minimizing sequences of characteristic functions may converge to non-classical designs which means they are not described by a characteristic function any more but rather by a density function θ. In that case there is no minimizer in U_{ad}, i.e. the problem is ill-posed. This problem corresponds exactly to the above mentioned example of increasingly finer mixtures of two separate phases.

Furthermore, the set U_{ad} is not stable with respect to standard variations. The convex combination of two characteristic functions is generally not a characteristic function, what eliminates the possibility of deriving optimality conditions.

Therefore the above stated optimization problem does generally not admit an optimal solution in the given admissible design set U_{ad}. Enlargement of the admissible design set and adjustment of objective functional and state equation to the extended problem is called

relaxation.

Nevertheless, we settle some properties of the functions g_α and g_β in order to guarantee the continuity of the later described relaxed objective functional and thus the solvability (well-posedness) of the relaxed optimization problem. As will be seen below (in §7.2.3), the following choice of properties of g_α and g_β is required: In the following we require (N dimension of Ω)

$$\begin{cases} g_{\alpha,\beta}(x,\lambda) \text{ is } \textbf{measurable} \text{ in } x \text{ for each } \lambda \in \mathbb{R} \\ g_{\alpha,\beta}(x,\lambda) \text{ is } \textbf{continuous} \text{ for a.e. } x \in \Omega \\ |g_{\alpha,\beta}(x,\lambda)| \leq k(x) + C|\lambda|^m \text{ with } k \in L^1(\Omega),\ 1 \leq m < \frac{2N}{N-2}, \end{cases} \tag{7.1.11}$$

whereby we appropriately take $1 \leq m < +\infty$ for dimensions $N = 1, 2$.
Furthermore, we employ additional assumptions on the partial derivatives of g_α and g_β to ensure that the Gâteaux differential of the later described relaxed cost function exists (see §7.3). For this purpose we require further:

$$\begin{cases} \frac{\partial g_{\alpha,\beta}}{\partial \lambda}(x,\lambda) \text{ is } \textbf{measurable} \text{ in } x \text{ for each } \lambda \in \mathbb{R} \\ \frac{\partial g_{\alpha,\beta}}{\partial \lambda}(x,\lambda) \text{ is } \textbf{continuous} \text{ for a.e. } x \in \Omega \\ |\frac{\partial g_{\alpha,\beta}}{\partial \lambda}(x,\lambda)| \leq k' + C'|\lambda|^{m-1} \text{ for } 1 \leq m < \frac{2N}{N-2} \text{ with } k'(x) \in L^q(\Omega),\ q > \frac{2N}{N-2}. \end{cases} \tag{7.1.12}$$

7.2. Relaxation of the problem

To overcome the problems of the non-solvability of the described optimization problem, we make use of the so-called relaxation via homogenization method. We follow again the argumentation of Allaire in [Allaire, 2002].
The principle of the relaxation process is to study the behaviour of minimizing sequences and to define generalized designs that include the possible limits of the minimizing sequences.
Given the introduced optimization problem

Find $\tilde{\chi}$ such that

$$\tilde{\chi} = \underset{\chi \in L^\infty(\Omega;\{1;0\})}{\arg\inf} J(\chi)$$

where the objective functional J is defined by

$$J(\chi) = \int_\Omega [\chi(x) g_\alpha(x, u_\chi(x)) + (1 - \chi(x)) g_\beta(x, u_\chi(x)))] \, \mathrm{d}x + l \int_\Omega \chi(x) \, \mathrm{d}x,$$

and u_χ is the solution of the state equation

$$\begin{cases} -\mathrm{div}(a_\chi(x)\nabla u_\chi(x)) = f(x) & \text{in } \Omega \\ u_\chi(x) = 0 & \text{on } \partial\Omega, \end{cases}$$

we follow the **Homogenization Method** to introduce a corresponding relaxed problem.

One can show that the weak * closure of the space $L^\infty(\Omega;\{0,1\})$ is $L^\infty(\Omega;[0,1])$. This implies that the weak * limit of a sequence of characteristic functions (χ_n) is the density θ of the material A in the domain Ω with values in the whole range $[0,1]$.

For a sequence of characteristic functions (χ_n) with weak limit θ and the sequence of corresponding material properties $A_n(x) = \chi_n(x)\alpha + (1-\chi_n(x))\beta$, we consider the sequence of state equations

$$\begin{cases} -\mathrm{div}(A_n(x)\nabla u_{\chi_n}(x)) = f(x) & \text{in } \Omega \\ u_{\chi_n}(x) = 0 & \text{on } \partial\Omega \end{cases}$$

interested in further information of the resultant limit problem created by χ_n for $n \to \infty$.

The theory of H-convergence provides the basis to derive that the problem of interest is the so-called **homogenized problem**

$$\begin{cases} -\mathrm{div}(A^*(x)\nabla u(x)) = f(x) & \text{in } \Omega \\ u(x) = 0 & \text{on } \partial\Omega \end{cases} \tag{7.2.1}$$

where A^* is denoted as **H-Limit** of the corresponding sequence (A_n) (cf. §7.2.1).

Based on this theory, we are interested in including these limit materials with material parameter A^* in our original problem formulation.

The tensor A^* is called **homogenized tensor** of a two-phase composite material obtained by mixing phase A and B in proportions θ and $1-\theta$ with a microstructure defined by the sequence (χ_n). It reflects the geometry of the mixture represented by the microstructure and is not uniquely defined by the proportion θ; this is why in the following the objective functional J is not only dependent on θ but also on A^*.

The pairs (θ, A^*) are called **generalized / composite admissible designs**. For fixed θ, the homogenized tensor A^* may be any symmetric matrix in the set of all possible homogenized tensors associated with the density θ, called G-closure $\mathcal{G}_\theta$.

In the given setting with two isotropic phases α, $\beta \in \mathbb{R}$, one can show that A^* is element of $\mathcal{G}_\theta$ if the point-wise values $A^*(x)$ belong to the set $G_{\theta(x)}$, which is described as the convex

set of all symmetric matrices with eigenvalues $\lambda_1, \ldots, \lambda_N$ satisfying

$$\begin{aligned} \lambda_\theta^- \leq \lambda_i \leq \lambda_\theta^+,\, 1 \leq i \leq N \\ \sum_{i=1}^{N} \frac{1}{\lambda_i - \alpha} \leq \frac{1}{\lambda_\theta^- - \alpha} + \frac{N-1}{\lambda_\theta^+ + \alpha} \\ \sum_{i=1}^{N} \frac{1}{\beta - \lambda_i} \leq \frac{1}{\beta - \lambda_\theta^-} + \frac{N-1}{\beta - \lambda_\theta^+}, \end{aligned} \tag{7.2.2}$$

with $\lambda_\theta^- = \left(\frac{\theta}{\alpha} + \frac{1-\theta}{\beta}\right)^{-1}$ and $\lambda_\theta^+ = \theta\alpha + (1-\theta)\beta$ the harmonic and arithmetic means of α and β (cf. §7.2.2).

We can extend the original problem to this set of attainable materials:

The **set of generalized admissible configurations** (Composite Designs) is accordingly

$$CD = \left\{(\theta, A^*) \in L^\infty(\Omega; [0,1] \times M_N^{\mathrm{s}}) | A^*(x) \in G_{\theta(x)} \text{ a.e. in } \Omega\right\}. \tag{7.2.3}$$

and the **generalized objective functional** is formulated as:

$$J^*(\theta, A^*) = \int_\Omega [\theta(x) g_\alpha(x, u(x)) + (1 - \theta(x)) g_\beta(x, u(x))]\, \mathrm{d}x + l \int_\Omega \theta(x)\, \mathrm{d}x, \tag{7.2.4}$$

where u is the solution of (7.2.1).

Then the **relaxed optimization problem** reads

$$\text{Find } (\tilde{\theta}, \tilde{A}^*) \text{ such that } (\tilde{\theta}, \tilde{A}^*) = \underset{(\theta, A^*) \in CD}{\arg\min}\ J^*(\theta, A^*). \tag{7.2.5}$$

Theorem 7.2.8 (cf. §7.2.3) justifies what is clear from an intuitive point of view: Relaxation is the reasonable expansion of the given optimization problem preserving the physical meaning of the given problem by extension of the admissible set of materials to composite materials.

7.2.1. H-convergence

In the following, we introduce the initially abstract theory of H-convergence, which provides the theoretical basis for the relaxation processes described above. As already stated we subsume the important details of [Allaire, 2002].

Let M_N be the linear space of real square matrices of dimension N. For two positive constants α, $\beta \in \mathbb{R}$ we define the subspace $M_{\alpha,\beta}$ of coercive matrices with coercive inverses:

$$M_{\alpha,\beta} = \left\{ M \in M_N : \begin{array}{c} M\xi \cdot \xi \geq \alpha |\xi|^2 \\ M^{-1}\xi \cdot \xi \geq \beta |\xi|^2 \end{array} \ \forall \xi \in \mathbb{R}^N \right\} \tag{7.2.6}$$

The theory of H-convergence examines a sequence of problems

$$\begin{cases} -\text{div}(A_n(x)\nabla u_n(x)) = f(x) & \text{in } \Omega \\ u_n(x) = 0 & \text{on } \partial\Omega \end{cases} \tag{7.2.7}$$

with tensors $A_n \in L^\infty(\Omega; M_{\alpha,\beta})$ and source terms $f \in H^{-1}$.

Coercivity of matrix and inverse guarantees existence and uniqueness of the corresponding solutions $u_n \in H_0^1(\Omega)$ by Lax-Milgram theorem and Riesz representation theorem: by coercivity of A_n, the corresponding bilinear form of the weak formulation is coercive, coercivity of the inverse ensures boundedness of A_n and thus continuity of the bilinear form.

For a given sequence of matrices (A_n), there exists a subsequence of the sequence of corresponding solutions u_n of the state equation and a limit $u \in H_0^1(\Omega)$ such that (u_n) converges weakly to u. This is due to the boundedness of (u_n) in $H_0^1(\Omega)$ and by relative compactness of bounded sets for the weak topology of $H_0^1(\Omega)$ (for details see [Allaire, 2002]). Furthermore, for another subsequence, one deduces weak convergence of the flux $\sigma_n = A_n\nabla u_n$ to a $\sigma \in L^2(\Omega)^N$ due to boundedness of (σ_n) in $L^2(\Omega)^N$ and by relative compactness of bounded sets for the weak topology of $L^2(\Omega)^N$. Passing to the limit in the given equation $-\text{div}\sigma_n = f$ one deduces $-\text{div}\sigma = f$ in Ω.

The main task of the theory of H-convergence is to define the equation satisfied by u and the connection between coefficients of this limit equation and the sequence (A_n) by introduction of the homogenized matrix A^*.

Definition 7.2.1.
A sequence of matrices (A_n) in $L^\infty(\Omega; M_{\alpha,\beta})$ is said to **converge in the sense of homogenization** or to **H-converge** to an homogenized limit A^* if for any $f \in H^{-1}(\Omega)$ the sequence (u_n) of solutions of

$$\begin{cases} -\text{div}(A_n(x)\nabla u_n(x)) = f(x) & \text{in } \Omega \\ u_n(x) = 0 & \text{on } \partial\Omega \end{cases} \tag{7.2.8}$$

satisfies

$$\begin{cases} u_n \rightharpoonup u & \text{weakly in } H_0^1 \\ A_n\nabla u_n \rightharpoonup A^*\nabla u & \text{weakly in } L^2(\Omega)^N \end{cases} \tag{7.2.9}$$

with u the solution of the homogenized equation

$$\begin{cases} -\mathrm{div}(A^*(x)\nabla u(x)) = f(x) & \text{in } \Omega \\ u(x) = 0 & \text{on } \partial\Omega. \end{cases} \tag{7.2.10}$$

A^* is then called **H-limit** of the sequence (A_n).

(as formulated by Allaire in [Allaire, 2002])

The following is a brief summary of results in the context of H-convergence, which are necessary for further comprehension of the present work. The theory of H-convergence as first described by Murat and Tartar in 1977/78 (English translation contained in [Cherkaev and Kohn, 1997], see [Murat and Tartar, 1997b]) provides the mathematical framework for analysis of composites. As stated by Cherkaev and Kohn in their introductory words, the theory has "the advantage of being self-contained, elegant, compact, and quite general", which makes it the method of choice especially in the present context.

The homogenization procedure is justified by the famous compactness theorem of H-convergence, which proofs existence of the H-limit A^* for a subsequence of a bounded sequence.

Theorem 7.2.2
For any sequence (A_n) of matrices in $L^\infty(\Omega; M_{\alpha,\beta})$, there exists a subsequence still denoted by (A_n) and an homogenized matrix $A^* \in L^\infty(\Omega; M_{\alpha,\beta})$ such that (A_n) H-converges to A^*.

(as formulated by Allaire in [Allaire, 2002])

This theorem was first proved in full generality by Murat and Tartar (English version [Murat and Tartar, 1997b]) by the so-called oscillating test function method.

The following properties deepen the understanding of the homogenization procedure (see [Allaire, 2002] for details):
The H-limit of a sequence is unique and local, consequently in a region ω, an open subset compactly contained in Ω, A^* does not depend on the values of (A_n) outside of the region. Moreover, the theory of H-convergence can be extended also to problems with different boundary conditions, not only Dirichlet boundary conditions for which it is defined. Furthermore, H-convergence implies local convergence of the energy density and also convergence of total energy.

Nevertheless, these abstract results do not deliver any information about an explicit formulation of the homogenized tensor A^* yet.
For this aim, we consider the special case of H-convergence for symmetric tensors

$$A \in M^{\mathrm{s}}_{\alpha,\beta} := \{A \in M_{\alpha,\beta} \mid A \text{ symmetric } \}.$$

In the literature, H-convergence in the context of symmetric operators is often called G-convergence. G-convergence was first introduced by Spagnolo in [Spagnolo, 1976] (English version) independently of the ideas of Murat and Tartar.
Although H-convergence is the more general formulation for non-symmetric operators, we can restrict ourselves to the case of symmetric tensors A_n and receive useful information about the structure of the set of attainable H-limits based on the symmetry and the consequence

$$(A_n x, x) = \left(x, A_n^T x\right) = (x, A_n x) \quad \forall x \in \mathbb{R}^N. \tag{7.2.11}$$

G-convergence as initially defined by Spagnolo does not include convergence of the flux $(A_n \nabla u)$ in the definition. Nevertheless, one can show that in case of symmetric tensors the two definitions actually coincide. H-convergence for a sequence of symmetric matrices (A_n) to a symmetric limit A^* directly implies G-convergence to the same limit by definition. Conversely one can show that for symmetric (A_n) convergence of the solutions (u_n) in the definition of G-convergence implies convergence of the flux $(A_n \nabla u)$, which then corresponds to the definition of H-convergence.
The compactness theorem 7.2.2 can therefore be formulated equivalently for symmetric tensors A_n, in particular the G-limits are again in the set $M^{\mathrm{s}}_{\alpha,\beta}$.
Besides the ordering of H-limits A^* and B^* for ordered sequences $(A_n) \in M^{\mathrm{s}}_{\alpha,\beta}$ and $(B_n) \in M^{\mathrm{s}}_{\alpha,\beta}$, $(A_n x, x) \leq (B_n x, x)$, we obtain the arithmetic and harmonic mean bounds, which are also often called Voigt–Reuss bounds or Wiener bounds. These bounds will be of great importance in the application of the Homogenization Method.

Theorem 7.2.3
Let (A_n) in $L^\infty(\Omega; M^{\mathrm{s}}_{\alpha,\beta})$ be a sequence that H-converges to an homogenized matrix A^*. Assume furthermore

$$A_n \rightharpoonup \overline{A} \text{ weakly } ^* \text{ in } L^\infty(\Omega; M^{\mathrm{s}}_{\alpha,\beta}) \tag{7.2.12}$$

$$(A_n)^{-1} \rightharpoonup \underline{A}^{-1} \text{ weakly } ^* \text{ in } L^\infty(\Omega; M^{\mathrm{s}}_{\alpha,\beta}). \tag{7.2.13}$$

Then the homogenized limit A^* satisfies

$$(\underline{A}x, x) \leq (A^* x, x) \leq (\overline{A}x, x) \quad \forall x \in \mathbb{R}^N. \tag{7.2.14}$$

(as formulated by Allaire in [Allaire, 2002])

The proof of Theorem 7.2.7 relies heavily on the hermiteness of symmetric matrices and the consequential identity (7.2.11), see for example [Allaire, 2002].
Important results for the argumentation can be derived by considering a special case, namely a sequence of matrices depending only on one single space variable x_1.

Theorem 7.2.4
Let $(A_n) \in L^\infty(\Omega; M_{\alpha,\beta})$ be a sequence with

$$A_n(x) = A_n(x_1).$$

Then, (A_n) H-converges to an homogenized matrix $A^*(x) = A^*(x_1)$ if and only if the following convergences hold in $L^\infty(\Omega)$ weak *:

$$\begin{cases} \frac{1}{A_n^{11}} & \rightharpoonup \frac{1}{A_{11}^*} & \\ \frac{A_n^{1j}}{A_n^{11}} & \rightharpoonup \frac{A_{1j}^*}{A_{11}^*} & 2 \le j \le N \\ \frac{A_n^{i1}}{A_n^{11}} & \rightharpoonup \frac{A_{i1}^*}{A_{11}^*} & 2 \le j \le N \\ \left(A_n^{ij} - \frac{A_n^{1j}A_n^{i1}}{A_n^{11}}\right) & \rightharpoonup \left(A_{ij}^* - \frac{A_{1j}^*A_{i1}^*}{A_{11}^*}\right) & 2 \le i,j \le N \end{cases}, \tag{7.2.15}$$

for the entries of A_n and A^*.

(as formulated by Allaire in [Allaire, 2002])

Following the theorem we deduce that for a scalar sequence of matrices $A_n(x) = a_n(x_1)I$ the homogenized matrix is computed as

$$A^*(x_1) = \operatorname{diag}(\underline{a}(x_1), \overline{a}(x_1), \ldots, \overline{a}(x_1)), \tag{7.2.16}$$

where $\overline{a}$, the weak * limit of a_n in $L^\infty(\Omega)$, is called **arithmetic mean**, and $\underline{a}$, where $\underline{a}^{-1}$ is the weak * limit of a_n^{-1} in $L^\infty(\Omega)$, is called **harmonic** mean (see [Allaire, 2002]).
This leads to an explicit description for so-called **rank-1 laminates**, also often called **simple laminates**, where slices of two phases A and B with material parameters α and β are stacked in proportions θ respectively $(1-\theta)$ in lamination direction x_1. For a simple laminate, the functions $a_n(x_1)$ and $a_n^{-1}(x_1)$ are oscillating functions with period ϵ on Ω. For Y-periodic functions $f_\epsilon(x) = f(\frac{x}{\epsilon})$, where $Y \subset \mathbb{R}^n$ is a periodicity cell, the weak * limit in $L^\infty(\Omega)$ is computed as

$$f_\epsilon \rightharpoonup \frac{1}{|Y|} \int_Y f(y)\,\mathrm{d}y, \tag{7.2.17}$$

see for example [Cioranescu and Donato, 1999]. With this result we derive the homogenised tensor

$$A^* = diag\left(\lambda_\theta^-, \lambda_\theta^+, \ldots, \lambda_\theta^+\right)$$

where $\lambda_\theta^- = \left(\frac{\theta}{\alpha} + \frac{(1-\theta)}{\beta}\right)^{-1}$ and $\lambda_\theta^+ = \theta\alpha + (1-\theta)\beta$ for simple laminates.
The description of a simple laminate with general lamination direction e as displayed in figure 7.2 can then be achieved by multiplication with corresponding rotation matrices, see §7.6.

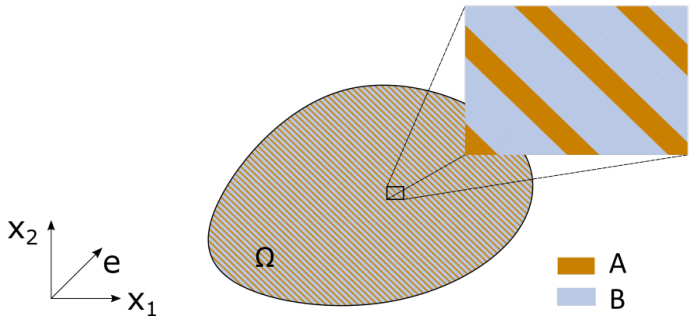

Figure 7.2.: Region Ω occupied by simple rank-1 laminate consisting of two materials A and B in proportions θ and $1-\theta$ and lamination direction e

By successively laminating, always with the same pure phase but with different proportions θ_i and lamination directions e_i, $1 \leq i \leq p$ one receives so-called **sequential laminates of rank** p. In §7.2.2, these materials will be of interest when studying optimal bounds of effective material parameters.
Back to the idea of optimization and relaxation, we now know that we have to extend our set of admissible designs and include the H-limits, which means that we have to concentrate on an explicit characterization of the properties of the H-limits in our specific case (for isotropic materials) if we want to set up a meaningful optimization problem. In the course of this, the H-limits describe precisely the composite materials that can be created from the two individual phases.

7.2.2. Homogenized properties of composite materials

In the following, we consider matrices A, $B \in M^s_{\alpha,\beta}$. We are interested in the homogenized properties of two-phase composites with a microstructure represented by a sequence of characteristic functions (χ_n) and effective properties modelled by the H-limit of the sequence $(\chi_n A + (1-\chi_n)B)$ and follow again the exposition of Allaire in [Allaire, 2002].

Definition 7.2.5.
Let $(\chi_n) \in L^\infty(\Omega; \{0;1\})$ be a sequence of characteristic functions, (A_n) the sequence of tensors defined by

$$A_n(x) = \chi_n A + (1 - \chi_n)B, \tag{7.2.18}$$

with $A, B \in M^{\mathrm{s}}_{\alpha,\beta}$.
Assume there exists $\theta \in L^\infty(\Omega; [0,1])$ and $A^* \in L^\infty(\Omega; M^{\mathrm{s}}_{\alpha,\beta})$ such that

$$\chi_n \rightharpoonup \theta \text{ weakly}^* \text{ in } L^\infty(\Omega, [0,1]) \tag{7.2.19}$$

and

$$(A_n) \text{ H-converges to } A^*. \tag{7.2.20}$$

A^* is said to be the **homogenized tensor of a two-phase composite material** obtained by mixing phases A and B in proportions θ and $1-\theta$ with a microstructure defined by the sequence (χ_n).

(as formulated by Allaire in [Allaire, 2002])

The composite material described by A^* is thus defined not only by the proportion θ of the two phases and their material properties but still dependent of the underlying microstructure represented by the sequence (χ_n).

When dealing with composite materials with effective homogenized tensor A^* the questions of interest are initially manifold. The question of attainable values of effective properties which is commonly referred to as **G-closure problem** is one of these. When an explicit characterization of $\mathcal{G}$, the G-closure of the set $\{A, B\}$ under H-convergence, is not possible (this is only possible in very vew cases) one is at least interested in bounds on the effective properties. In the described setting, we aim for a characterization of the attainable values of the homogenized tensor in terms of bounds or explicit expressions when the proportion θ of the two phases is given. Except in some special cases there is no explicit formula for computing A^*, but since A_n only takes two different values one expects that the homogenized limit can only take certain values. In the present context, when interested in the G-closure of two isotropic phases A and B with material parameters α and β, $\mathcal{G}_\theta$ is actually explicitly known.

Nevertheless, we start with consideration of the mixture of two possibly anisotropic phases A and B in proportions θ and $(1-\theta)$, obtaining information about the general structure

of the G-closure $\mathcal{G}_\theta$

$$\mathcal{G}_\theta = \left\{ A^* \in L^\infty(\Omega; M^{\mathrm{s}}_{\alpha,\beta}) \,\middle|\, \exists A, B, \chi_n : \begin{array}{l} \chi_n \text{ satisfies (7.2.19)} \\ (A_n) \text{ defined by (7.2.18) satisfies (7.2.20)} \end{array} \right\}. \tag{7.2.21}$$

Theorem 7.2.6
For any function $\theta \in L^\infty(\Omega; [0,1])$, the G-closure set $\mathcal{G}_\theta$ is characterized by

$$\mathcal{G}_\theta = \left\{ A^* \in L^\infty(\Omega; M^{\mathrm{s}}_{\alpha,\beta}) | A^*(x) \in G_{\theta(x)} \text{ a.e. in } \Omega \right\}, \tag{7.2.22}$$

where for any real number $\theta \in [0,1]$ the set $G_\theta \subset M^{\mathrm{s}}_{\alpha,\beta}$ is defined as the closure of the set of all constant effective tensors obtained by periodic homogenization of a mixture of A and B in proportions θ and $(1-\theta)$.

(as formulated by Allaire in [Allaire, 2002])

The main benefit from this theorem is the conclusion, that the properties of effective tensors of composite materials are local and obtained by periodic homogenization. We can therefore concentrate on characterization in terms of bounds or explicit formulation of the set G_θ.

There exist several methods to obtain bounds on effective properties of composite designs, L. Gibiansky classifies them in his lecture notes ([Gibiansky, 1993]) as **Hashin-Shtrikman variational principle** (first introduced by Hashin and Shtrikman in [Hashin and Shtrikman, 1963]), **analytical method** (see for example Bergman [Bergman, 1982] and Milton [Milton, 1980]) or **translation method** (introduced in different forms by Murat and Tartar as application of compensated compactness and by Lurie and Cherkaev, both in english version published in [Cherkaev and Kohn, 1997]).

Milton summarizes the idea of all above mentioned methods to characterize G_θ in [Milton, 1990]: the common concept is to find effective tensors on the boundary of G_θ. This is first addressed by characterizing a region (in terms of bounds) which can be proven to contain G_θ and then by looking for composites with micro-structures such that their effective tensor lies on the bounding surface. In this manner, Tartar derives G_θ for two isotropic conductivities $\alpha, \beta \in \mathbb{R}$ as bounded set from confocal ellipsoids (see for example [Tartar, 2009]). It is also possible and in our case most expedient to derive G_θ from the sequential laminates as optimal micro-structures, which was done for example by Allaire in [Allaire, 2002].

Theorem 7.2.7
The set G_θ, the set of all constant effective tensors obtained by homogenization of a mixture of α and β in proportions θ and $(1-\theta)$, is the convex set of all symmetric matrices with eigenvalues $\lambda_1, \ldots, \lambda_N$ satisfying

$$\begin{aligned} \lambda_\theta^- \leq \lambda_i \leq \lambda_\theta^+,\ 1 \leq i \leq N \\ \sum_{i=1}^{N} \frac{1}{\lambda_i - \alpha} \leq \frac{1}{\lambda_\theta^- - \alpha} + \frac{N-1}{\lambda_\theta^+ + \alpha} \\ \sum_{i=1}^{N} \frac{1}{\beta - \lambda_i} \leq \frac{1}{\beta - \lambda_\theta^-} + \frac{N-1}{\beta - \lambda_\theta^+}. \end{aligned} \tag{7.2.23}$$

with $\lambda_\theta^- = \left(\frac{\theta}{\alpha} + \frac{1-\theta}{\beta}\right)^{-1}$ and $\lambda_\theta^+ = \theta\alpha + (1-\theta)\beta$ the harmonic and arithmetic mean of α and β.

(as formulated by Allaire in [Allaire, 2002])

Following the argumentation of Allaire in [Allaire, 2002], there is one composite material that meets the bounds with equality, namely the special case of the simple laminate, characterized by one eigenvalue equal to the harmonic mean $\underline{a} = \lambda_\theta^-$ and all other eigenvalues equal to the arithmetic mean $\bar{a} = \lambda_\theta^+$. This is of major importance for proof of the optimality criteria and for development of an optimization routine.

With characterization of G_θ, we can now specify the extended (relaxed) set of admissible designs

$$CD = \left\{(\theta, A^*) \in L^\infty(\Omega; [0,1] \times M^{\mathrm{s}}_{\alpha,\beta}) | A^*(x) \in G_{\theta(x)} \text{ a.e. in } \Omega\right\}. \tag{7.2.24}$$

Relaxation of the admissible design set entails modification of the objective functional $J(\chi)$, we relax the formulation to

$$J^*(\theta, A^*) = \int_\Omega [\theta(x) g_\alpha(x, u(x)) + (1-\theta(x)) g_\beta(x, u(x))]\, \mathrm{d}x + l \int_\Omega \theta(x)\, \mathrm{d}x. \tag{7.2.25}$$

The complete formulation of our optimization problem reads accordingly

Find $(\tilde{\theta}, \tilde{A^*})$ such that

$$(\tilde{\theta}, \tilde{A^*}) = \underset{(\theta, A^*) \in CD}{\arg\min}\ J^*(\theta, A^*) \tag{7.2.26}$$

with objective functional

$$J^*(\theta, A^*) = \int_\Omega [\theta(x) g_\alpha(x, u(x)) + (1 - \theta(x)) g_\beta(x, u(x))] \, \mathrm{d}x + l \int_\Omega \theta(x) \, \mathrm{d}x, \tag{7.2.27}$$

set of generalized admissible configurations

$$CD = \left\{ (\theta, A^*) \in L^\infty(\Omega; [0,1] \times M^s_{\alpha,\beta}) | A^*(x) \in G_{\theta(x)} \text{ a.e. in } \Omega \right\} \tag{7.2.28}$$

and u the solution of

$$\begin{cases} -\mathrm{div}(A^*(x) \nabla u(x)) = f(x) & \text{in } \Omega \\ u(x) = 0 & \text{on } \partial\Omega \end{cases} . \tag{7.2.29}$$

7.2.3. Justification of relaxation

The following theorem justifies the described relaxation via homogenization theory:

Theorem 7.2.8
The minimization problem (7.2.26) is a true relaxation of the original problem (7.1.7) in the sense that

1. *There exists at least one minimizer of $J^*(\theta, A^*)$ in CD.*
2. *Up to a subsequence, every minimizing sequence of classical designs (χ_n) for J converges weakly * to a density function θ and the associated conductivity $a_{\chi_n} = \alpha\chi_n + (1 - \beta)\chi_n$ H-converges to an homogenized tensor A^* such that (θ, A^*) is a minimizer of $J^*(\theta, A^*)$ in CD.*
3. *Every minimizer (θ, A^*) of $J^*(\theta, A^*)$ in CD is attained by a minimizing sequence of classical designs (χ_n) for J, namely θ is the weak * limit of χ_n in $L^\infty(\Omega; [0,1])$ and A^* is the H-limit of $a_{\chi_n} = \alpha\chi_n + (1 - \beta)\chi_n$.*

(as formulated by Allaire in [Allaire, 2002])

In the proof (see for example [Allaire, 2002]), assumptions (7.1.11) on the functions g_α and g_β ensure the continuity relation of the objective functional.

7.3. Gâteaux differential of the objective functional

In the following, we employ the specific vocabulary of Gâteaux differentiability (a very short introduction can be found in [Tröltzsch, 2009]).
In contrast to the original formulation of the optimization problem, the obtained relaxed formulation allows the deduction of optimality conditions.
With the assumptions (7.1.11) on g_α and g_β and (7.1.12) on the corresponding partial derivatives we are now able to perform the standard calculus of variations procedure.
Following the diction of [Allaire, 2002], the **admissible increment**

$$(\delta\theta, \delta A^*) = \left(\frac{\mathrm{d}\theta}{\mathrm{d}t}(0), \frac{\mathrm{d}A^*}{\mathrm{d}t}(0)\right)$$

is the derivative with respect to a scalar parameter $t \in [0,1]$ at $t = 0$ of a smooth continuously differentiable path $(\theta(t), A^*(t))$ in the set of composite designs CD which coincides for $t = 0$ with the point (θ, A^*), where the derivative of J^* is computed.
The design parameters $(\theta(t), A^*(t))$ provide via solution of the state equation a path $u(t)$ of the state variable, and we accordingly define the **state increment**

$$\delta u = \frac{\mathrm{d}u}{\mathrm{d}t}(0)$$

and the **objective increment**

$$\delta J^* = \frac{\mathrm{d}}{\mathrm{d}t}[J^*(\theta(t), A^*(t))](0).$$

Theorem 7.3.1
The relaxed cost function is Gâteaux differentiable on CD with directional derivative

$$\delta J^*(\theta, A^*) = \int_\Omega \delta\theta(x)[g_\alpha(x, u(x)) - g_\beta(x, u(x)) + l]\,\mathrm{d}x - \int_\Omega \delta A^*(x)\nabla u(x)\cdot\nabla p(x)\,\mathrm{d}x. \quad (7.3.1)$$

$\delta\theta$ and δA^* are admissible increments in CD, u solution of (7.2.29) and p is solution of the adjoint state equation

$$\begin{cases} -\mathrm{div}(A^*(x)\nabla p(x)) = \theta(x)\frac{\partial g_\alpha}{\partial\lambda}(x, u(u)) + (1-\theta(x))\frac{\partial g_\beta}{\partial\lambda}(x, u(x)) & \text{in } \Omega \\ p(x) = 0 & \text{on } \partial\Omega. \end{cases} \quad (7.3.2)$$

(as formulated by Allaire in [Allaire, 2002])

The proof of theorem 7.3.1 follows the standard procedure of eliminating the state increment δu from the directional derivative δJ by introduction of the adjoint problem. For details we

refer to [Allaire, 2002] and the proofs in §8.3.3 and §9.3.2 which follow the same procedure. In the course of this, properties (7.1.12) of the partial derivatives $\frac{\partial g_{\alpha,\beta}}{\partial \lambda}(x,\lambda)$ ensure that the objective functional is differentiable and that the source term of the adjoint equation is in $H^{-1}(\Omega)$.
Following the standard principle of the calculus of variations, we can subsequently deduce the necessary optimality conditions from the variational inequality.

7.4. Optimality conditions

If (θ, A^*) is a minimizer of J^*, the inequality

$$\delta J^*(\theta, A^*) \geq 0 \tag{7.4.1}$$

has to hold for any admissible increment $(\delta\theta, \delta A^*)$.
However, the characterization of the set of admissible increments $(\delta\theta, \delta A^*)$ is not straightforward. A varying θ leads to a varying set G_θ of admissible tensors A^* which complicates the characterization of admissible increments δA^*.
Nevertheless, following [Allaire and Castro, 2001] and considering the special structure of the set of admissible designs CD we can perform the minimization process in two steps:

$$\min_{(\theta,A^*)\in CD} J^*(\theta, A^*) = \min_{0\leq\theta\leq 1} \min_{A^*\in G_\theta} J^*(\theta, A^*). \tag{7.4.2}$$

Following this argumentation the derivation of optimality criteria is performed in two steps as well (see [Allaire, 2002]): first we fix the optimal material density θ and deduce necessary optimality conditions for A^*. In a second step we take an optimal tensor A^* (in the sense that the tensor A^* satisfies the necessary optimality condition derived before) and vary the density θ.

Based on the assumption of optimality in θ we deduce a first necessary condition for A^*. Keeping θ fixed, i.e. $\delta\theta = 0$ the optimality condition $\delta J^*(\theta, A^*) \geq 0$ becomes

$$\delta J^*(\theta, A^*) = -\int_\Omega \delta A^*(x)\nabla u(x) \cdot \nabla p(x)\,\mathrm{d}x \geq 0. \tag{7.4.3}$$

From this necessary condition of optimality the following theorem can be derived, describing the necessary condition for A^* to be optimal.

Theorem 7.4.1
If (θ, A^*) is a minimizer of the objective functional $J^*(\theta, A^*)$, then except at the points where $\nabla u = 0$ or $\nabla p = 0$ we have

$$2A^*\nabla u = \left(\lambda_\theta^+ + \lambda_\theta^-\right)\nabla u + \left(\lambda_\theta^+ - \lambda_\theta^-\right)\frac{|\nabla u|}{|\nabla p|}\nabla p \tag{7.4.4}$$

$$2A^*\nabla p = \left(\lambda_\theta^+ + \lambda_\theta^-\right)\nabla p + \left(\lambda_\theta^+ - \lambda_\theta^-\right)\frac{|\nabla p|}{|\nabla u|}\nabla u, \tag{7.4.5}$$

where u is solution of the state equation, p solution of the adjoint equation, $\lambda_\theta^- = \left(\frac{\theta}{\alpha} + \frac{1-\theta}{\beta}\right)^{-1}$ and $\lambda_\theta^+ = \theta\alpha + (1-\theta)\beta$.
At points where $\frac{\nabla u}{|\nabla u|} \neq \frac{\nabla p}{|\nabla p|}$ the optimal tensor A^* satisfying necessary optimality conditions (7.4.4) and (7.4.5) is unique and corresponds to a simple laminate.
Furthermore there exists another minimizer $(\bar{\theta}, \bar{A}^*)$ which admits the same state u and adjoint state p, such that almost everywhere in Ω the optimal tensor $\bar{A}^*$ is a simple laminate.

(as formulated by Allaire in [Allaire, 2002])

The best about this information is that one no longer has to care about the unmanageable set G_θ but we can restrict our interest to that of rank-1 laminates with their explicit representation based on proportion θ and the direction of the lamination e (see figure 7.2). In the following, we will refer to this circumstance as **optimality of simple laminates**.
For the proof of the optimality criteria (see for example [Allaire, 2002]), hermiteness and the resulting consequences

$$\max_{A^* \in G_\theta} A^*\xi \cdot \xi = \lambda_\theta^+ \xi \cdot \xi$$

and

$$\min_{A^* \in G_\theta} A^*\xi' \cdot \xi' = \lambda_\theta^- \xi' \cdot \xi'$$

are decisive.
Following [Murat and Tartar, 1997a] the proof of the optimality of simple laminates is then due to Raitum (1978) who prooved that one can change A^* in the region where $|\nabla u||\nabla p| = 0$ without changing $A^*\nabla u$ and thus without changing the solution u.
For fixed density θ, theorem 7.4.1 provides the necessary optimality condition for the lamination direction e.

We now assume that A^* is optimal, which means it meets the deduced necessary optimality condition. Therefore, following theorem 7.4.1, we find A^* as simple laminate with (7.4.4) and (7.4.5).

Introducing the angle ϕ via

$$\nabla u \cdot \nabla p = |\nabla u||\nabla p| \cos\phi \tag{7.4.6}$$

and defining

$$Q(x) = g_\alpha(x, u(x)) - g_\beta(x, u(x)) + l + \frac{\beta - \alpha}{\alpha\beta}|\nabla u||\nabla p| \left(\alpha\beta \cos^2 \frac{\phi}{2} - (\lambda_\theta^-)^2 \sin^2 \frac{\phi}{2} \right), \tag{7.4.7}$$

one derives necessary optimality conditions for the density θ.

Theorem 7.4.2
If (θ, A^*) is a minimizer of the objective functional $J^*(\theta, A^*)$, then the optimal density satisfies almost everywhere in Ω

$$\theta(x) = 0 \quad \text{if } Q(x) > 0 \tag{7.4.8}$$
$$\theta(x) = 1 \quad \text{if } Q(x) < 0 \tag{7.4.9}$$
$$0 \leq \theta(x) \leq 1 \quad \text{if } Q(x) = 0 \tag{7.4.10}$$

and conversely it holds

$$Q(x) \geq 0 \quad \text{if } \theta(x) = 0 \tag{7.4.11}$$
$$Q(x) \leq 0 \quad \text{if } \theta(x) = 1 \tag{7.4.12}$$
$$Q(x) = 0 \quad \text{if } 0 \leq \theta(x) \leq 1. \tag{7.4.13}$$

(as formulated by Allaire in [Allaire, 2002])

In the proof of theorem 7.4.2, one considers a smooth continuous differentiable path $(\theta(t), A^*(t))$ in CD that takes the optimal value (θ, A^*) for $t = 0$. Due to theorem 7.4.1 one can assume without loss of generality that A^* describes a rank-1 laminate where $\nabla u \neq 0$ and $\nabla p \neq 0$ with direction of lamination defined by the derived necessary optimality condition. Further, $A^*(t)$ is required to belong to $G_{\theta(t)}$ almost everywhere in Ω for $t \in [0, 1]$, where $\nabla u \neq 0$ and $\nabla p \neq 0$. One can show that the admissible increment δA^* satisfies

$$\delta A^* \nabla u \cdot \nabla p = \left[\frac{\alpha - \beta}{\alpha\beta}|\nabla u||\nabla p| \left(\alpha\beta \cos^2 \frac{\phi}{2} - (\lambda_\theta^-)^2 \sin^2 \frac{\phi}{2} \right) \right] \delta\theta. \tag{7.4.14}$$

Inserting (7.4.14) into the formulation of the directional derivative (7.3.1), one obtains the desired result, for details see [Allaire, 2002].

These two steps form the basis for an optimality criteria algorithm. On the grounds of theorem 7.4.1 and theorem 7.4.2, one can perform the update of lamination direction e and density θ point-wise and separately both on basis of u and p.

Moreover, the information on the optimality of simple laminates provides the basis for a gradient method based on the formulation of the objective functional subject to the two design variables density θ and lamination direction e.

7.5. Optimality criteria method

The optimality criteria derived in the last chapter and in particular the optimality of simple rank-1 laminates provide the basis for an optimality criteria based algorithm.

Based on given design parameters θ_k and e_k with associated state solutions u_k and p_k, we update the design parameters as described below, see [Allaire, 2002].

Update lamination direction

One obtains the lamination direction e of an optimal A^* for $|\nabla u| \cdot |\nabla p| \neq 0$ as the eigenvector of A^* to the eigenvalue λ_θ^- as:

$$e = \frac{\nabla u}{|\nabla u|} - \frac{\nabla p}{|\nabla p|}, \tag{7.5.1}$$

since

$$A^* e = \lambda_\theta^- e. \tag{7.5.2}$$

by theorem 7.4.1.

Accordingly, we update

$$e_k = \frac{\nabla u_k}{|\nabla u_k|} - \frac{\nabla p_k}{|\nabla p_k|}, \tag{7.5.3}$$

where $|\nabla u| \cdot |\nabla p| \neq 0$.

Furthermore, one can show that in cases where $\frac{\nabla u_k}{|\nabla u_k|} = \frac{\nabla p_k}{|\nabla p_k|}$, one finds the lamination direction orthogonal to $\frac{\nabla u_k}{|\nabla u_k|} + \frac{\nabla p_k}{|\nabla p_k|}$ (see [Allaire, 2002] for details).

Update density

From the optimality criteria deduced in theorem 7.4.2, we know that an optimal density θ, $0 < \theta < 1$ satisfies

$$g_\alpha(x,u) - g_\beta(x,u) + l + \frac{\beta - \alpha}{\alpha\beta} |\nabla u||\nabla p| \left(\alpha\beta \cos^2(\frac{\phi}{2}) - (\lambda_\theta^-)^2 \sin^2(\frac{\phi}{2}) \right) = 0$$

with ϕ being the angle between ∇u and ∇p:

$$\nabla u \cdot \nabla p = |\nabla u||\nabla p| \cos(\phi).$$

To compute θ_{k+1}, we consequently look for the root of

$$F(\theta) = g_\alpha(x,u_k) - g_\beta(x,u_k) + l + \frac{\beta-\alpha}{\alpha\beta}|\nabla u_k||\nabla p_k| \left(\alpha\beta\cos^2(\frac{\phi_k}{2}) - (\lambda_\theta^-)^2\sin^2(\frac{\phi_k}{2})\right),$$

with ϕ_k the corresponding angle between ∇u_k and ∇p_k.

One considers the two cases $\sin(\frac{\phi_k}{2}) \neq 0$ and $\sin(\frac{\phi}{2}) = 0$.

For $\sin(\frac{\phi_k}{2}) \neq 0$, $F(\theta)$ is strictly increasing for θ on $[0,1]$. Consequently we compute θ_{k+1} as follows:

$$\begin{cases} \text{for } F(1) < 0: & \theta_{k+1} = 1 \\ \text{for } F(0) > 0: & \theta_{k+1} = 0 \\ \text{otherwise:} & \text{compute } \theta_{k+1} \text{ such that } F(\theta_{k+1}) = 0. \end{cases}$$

For $\sin(\frac{\phi}{2}) = 0$ (or at least very small), one cannot derive θ as root of F. Nevertheless, one can show that the optimality condition for θ can be rewritten in terms of fluxes $\sigma = A^*\nabla u$ and $\tau = A^*\nabla p$ (for details see [Allaire, 2002]):

$$g_\alpha(x,u) - g_\beta(x,u) + l + (\beta-\alpha)|\sigma||\tau| \left((\lambda_\theta^+)^{-2}\cos^2(\frac{\varphi}{2}) - (\alpha\beta)^{-1}\sin^2(\frac{\varphi}{2})\right) = 0,$$

and φ defined by

$$\sigma \cdot \tau = |\sigma||\tau|\cos(\varphi).$$

Due to the fact that $\phi = 0$ implies $\varphi = 0$, one can compute θ_{k+1} accordingly as root of $\tilde{F}$ with $\sigma_k = A^*\nabla u_k$, $\tau_k = A^*\nabla p_k$ and φ_{k+1} the angle between σ_k and τ_k:

$$\tilde{F}(\theta) = g_\alpha(x,u_k) - g_\beta(x,u_k) + l + (\beta-\alpha)|\sigma_k||\tau_k| \left((\lambda_\theta^+)^{-2}\cos^2(\frac{\varphi_k}{2}) - (\alpha\beta)^{-1}\sin^2(\frac{\varphi_k}{2})\right).$$

With this information the algorithm is described as follows

Optimality criteria method:

Initialization: Initialize θ_0 and e_0 and compute A^* as simple rank-1 laminate tensor. For simplicity, choose constant θ_0 and constant lamination direction e_0.

Iteration for $k \geq 0$: until convergence

1. Compute state u_k and adjoint state p_k as solutions of the corresponding problems with the previous design parameters θ_k and e_k.
2. Update parameters by using optimality conditions to obtain θ_{k+1} and e_{k+1}. Compute corresponding A^*_{k+1}.

7.6. Gradient method in 2d

Although the algorithm via optimality criteria succeeds in certain cases (see for example [Allaire, 2002]), an algorithm with guaranteed improvement of the objective functional and guaranteed convergence at least to a local minimum is preferable in more complex applications, for which the optimality criteria algorithm does not automatically correspond to a descent method.
Deducing the gradient of the objective functional, we can implement such a gradient method, which is described for example in [Allaire and Castro, 2001].

As before, our design parameters are the density θ and the lamination direction of the composite e, which corresponds to the rotation angle φ of the rank-1 laminate tensor:

$$A^*(\theta,\varphi) = R(\varphi)\begin{pmatrix}\lambda_\theta^- & 0\\ 0 & \lambda_\theta^+\end{pmatrix}R^{-1}(\varphi) \tag{7.6.1}$$

with rotation matrix

$$R(\varphi) = \begin{pmatrix}\cos(\varphi) & -\sin(\varphi)\\ \sin(\varphi) & \cos(\varphi)\end{pmatrix}. \tag{7.6.2}$$

At this point we use the tensor described in equation (7.2.16) for a simple laminate with lamination direction x_1. Accordingly, our rotation matrices look different from those described by Allaire in [Allaire, 2002], due to the fact that the tensor used by Allaire describes a laminate with lamination direction x_2. A short calculation confirms the equivalence of the formulations.
A simple but lengthy computation shows that the directional derivative of the objective functional $J^*(\theta,\varphi)$ with respect to the admissible increment $(\delta\theta,\delta\varphi)$ is then given by

$$\delta J^*(\theta,\varphi) = -\int_\Omega \frac{\partial A^*}{\partial\varphi}\nabla u\cdot\nabla p\,\delta\varphi\,\mathrm{d}x + \int_\Omega Q(x)\delta\theta\,\mathrm{d}x, \tag{7.6.3}$$

where

$$\begin{aligned} Q(x) = {} & g_\alpha(x,u) - g_\beta(x,u) + l \\ & -\frac{d\lambda_\theta^-}{d\theta}\left[\cos^2(\varphi)\frac{\partial u}{\partial x_1}\frac{\partial p}{\partial x_1} + \sin^2(\varphi)\frac{\partial u}{\partial x_2}\frac{\partial p}{\partial x_2} + \cos(\varphi)\sin(\varphi)\left(\frac{\partial u}{\partial x_2}\frac{\partial p}{\partial x_1} + \frac{\partial u}{\partial x_1}\frac{\partial p}{\partial x_2}\right)\right] \\ & -\frac{d\lambda_\theta^+}{d\theta}\left[\sin^2(\varphi)\frac{\partial u}{\partial x_1}\frac{\partial p}{\partial x_1} + \cos^2(\varphi)\frac{\partial u}{\partial x_2}\frac{\partial p}{\partial x_2} - \cos(\varphi)\sin(\varphi)\left(\frac{\partial u}{\partial x_1}\frac{\partial p}{\partial x_2} + \frac{\partial u}{\partial x_2}\frac{\partial p}{\partial x_1}\right)\right]. \end{aligned}$$

On this basis we formulate the gradient method as follows.

Gradient method:

Initialization: Initialize θ_0 and φ_0 and compute A^*. For simplicity, choose constant θ_0 and constant angle φ_0.

Iteration for $k \geq 0$: until convergence

1. Compute state u_k and adjoint state p_k as solutions of the corresponding problems with the previous design parameters θ_k and φ_k.
2. Update parameters by

$$\varphi_{k+1} = \varphi_k + t_k \frac{\partial A^*}{\partial \varphi}(\theta_k, \varphi_k) \nabla u_k \cdot \nabla p_k$$

$$\theta_{k+1} = \max(0, \min(1, \theta_k - t_k Q_k))$$

with t_k a small step such that $J^*(\theta_{k+1}, \varphi_{k+1}) < J^*(\theta_k, \varphi_k)$

The projection applied on θ_{k+1} ensures θ_{k+1} to belong to the set of admissible densities in $[0, 1]$.

8. Extensions of existing theory and methods with real-valued material parameters

The theory and gradient method introduced in chapter 7 provide the basis for further development of the described theory and methods in the context of sensor optimization. In §8.1, we present important aspects of the implementation of the gradient method based on cooperation of MATLAB® and COMSOL® via LiveLink™ for MATLAB®. This implementation forms the basis for all enhancements of the implementation described below both in chapter 8 and chapter 10. After validation of the implementation of the gradient method in 2d in §8.2, we extend the theory to optimization of the material distribution in a subdomain of Ω in §8.3. In §8.4, we expand the gradient method described in §7.6 to 3d problems.

8.1. Implementation aspects

Implementation of the described gradient method includes on the one side adjustment of step size t_k and updating of the design parameters θ_k and e_k in every iteration step, on the other side computation of the solution u_k and adjoint solution p_k by solving the corresponding problems on the given domain Ω. In addition, compliance with the volume constraint must be ensured by adaptation of the introduced Lagrange Multiplier l_k in each iteration step.

The implementation of all application examples based on the gradient method has basically the following structure.

Initialize:
$\theta_0 = 0$; $e_0 = 0$;
Compute u_0 and p_0 with design parameters θ_0 and e_0;
Compute objective functional value $J(\theta_0, e_0)$;
$J_0 = J(\theta_0, e_0)$;
$k = 0$;

while *(convergence criterion not fulfilled)* **do**
  $J_{k+1} = J_k$;

  while $J_{k+1} \geq J_k$ **do**
    adjust stepsize t_k;

    while *(volume constaint not fulfilled)* **do**
      adjust l_k via bisection method;
      update design parameters θ_{k+1}, e_{k+1}
    end

    Compute u_{k+1} and p_{k+1} with design parameters θ_{k+1} and e_{k+1};
    Compute objective functional value $J_{k+1}(\theta_{k+1}, e_{k+1})$;
    $J_{k+1} = J_{k+1}(\theta_{k+1}, e_{k+1})$;
  end
  $k = k + 1$;
end

The lamination direction e is described by one corresponding angle φ (see §7.6) in two dimensions, in three dimensions, we extend the formulation accordingly to two angles ψ and φ (see §8.4).

Since COMSOL® allows close cooperation with MATLAB® via corresponding LiveLink™, we divide the implementation in two different parts. The optimization routine, including update process of material parameters based on the design parameters density θ_k and lamination direction e_k, step size adjustment and adaptation of the Lagrange Multiplier l_k is performed in MATLAB®. Numerical approximation of the solution of the corresponding PDE and adjoint PDE with state u_k and adjoint state p_k is outsourced in COMSOL Multiphysics®(highlighted in blue). We profit in particular from the 3d-capabilities and simple model generation in COMSOL®, whilst the basic structure of the implementation of the optimization routine in MATLAB® remains unaffected.

To ensure the correct data exchange between COMSOL® and MATLAB®, the corresponding information on updated material parameters and updated solutions u_k and p_k in all Lagrange and Gauss points relevant for the Finite Element Method is temporarily stored in text files.

We start with a stepszize of $t_k = 1$ in every iteration step and reduce the step size by

powers of ten until the objective functional decreases accordingly.
In order to ensure the compliance with the volume constraint the algorithm includes adaptation of the Lagrange Multiplier performed by the inner loop adjusting l_k for every step size t_k. Following the argumentation of Allaire [Allaire, 2002], we use the bisection method since the volume of phase A is a non-increasing function of l.
In the presented applications we use the exceeding of a fixed number of iteration steps as convergence criterion.

8.2. Gradient method in 2d: Application and verification of the implementation

The following example provides the basis for verification of the implementation in comparison with the corresponding results from [Glowinski, 1983] and [Allaire, 2002]. We compare further our simulation results derived by application of the optimality criteria method with our results of the implemented gradient method.
We consider the self-adjoint optimization problem

$$\min_{(\theta,A^*)\in CD} J^*(\theta, A^*) = \min_{(\theta,A^*)\in CD} -\int_\Omega u(x)\,\mathrm{d}x + l\int_\Omega \theta(x)\,\mathrm{d}x,$$

with u solution of

$$\begin{cases} -\mathrm{div}(A^*(x)\nabla u(x)) = 1 & \text{in } \Omega \\ u(x) = 0 & \text{on } \partial\Omega \end{cases} \tag{8.2.1}$$

and adjoint state $p = -u$ on $\Omega = (0,1)^2$ with $\alpha = 1$, $\beta = 2$ and a volume constraint of 50% of phase A, which is controlled by adaptation of the Lagrange Multiplier l as described in §8.1.
The problem can be interpreted as a design problem seeking for the worst conducting respectively best isolating design of the two materials α and β based on stationary heat conduction with uniform source term.
We initialize the problem with a constant volume fraction $\theta = 0.5$ and constant lamination direction $e = (1,0)^T$. The 2d simulations are performed on a triangular mesh with quadratic Lagrange elements resulting in 12765 DOF.
Figure 8.1 shows initialization ($k = 0$) and status of the optimization after steps 1, 3, 5 and 50 of the optimality criteria method. The volume fraction θ is shown in the left column, lamination direction e in the middle and state u is shown in the right column. The results serve as a basis for the verification of the gradient method used in the following.
Figure 8.2 shows initialization ($k = 0$) and status of the optimization after steps 1, 20, 50 and 200 of the gradient method. θ is again shown in the left column, lamination direction e in the middle and state u in the right column.

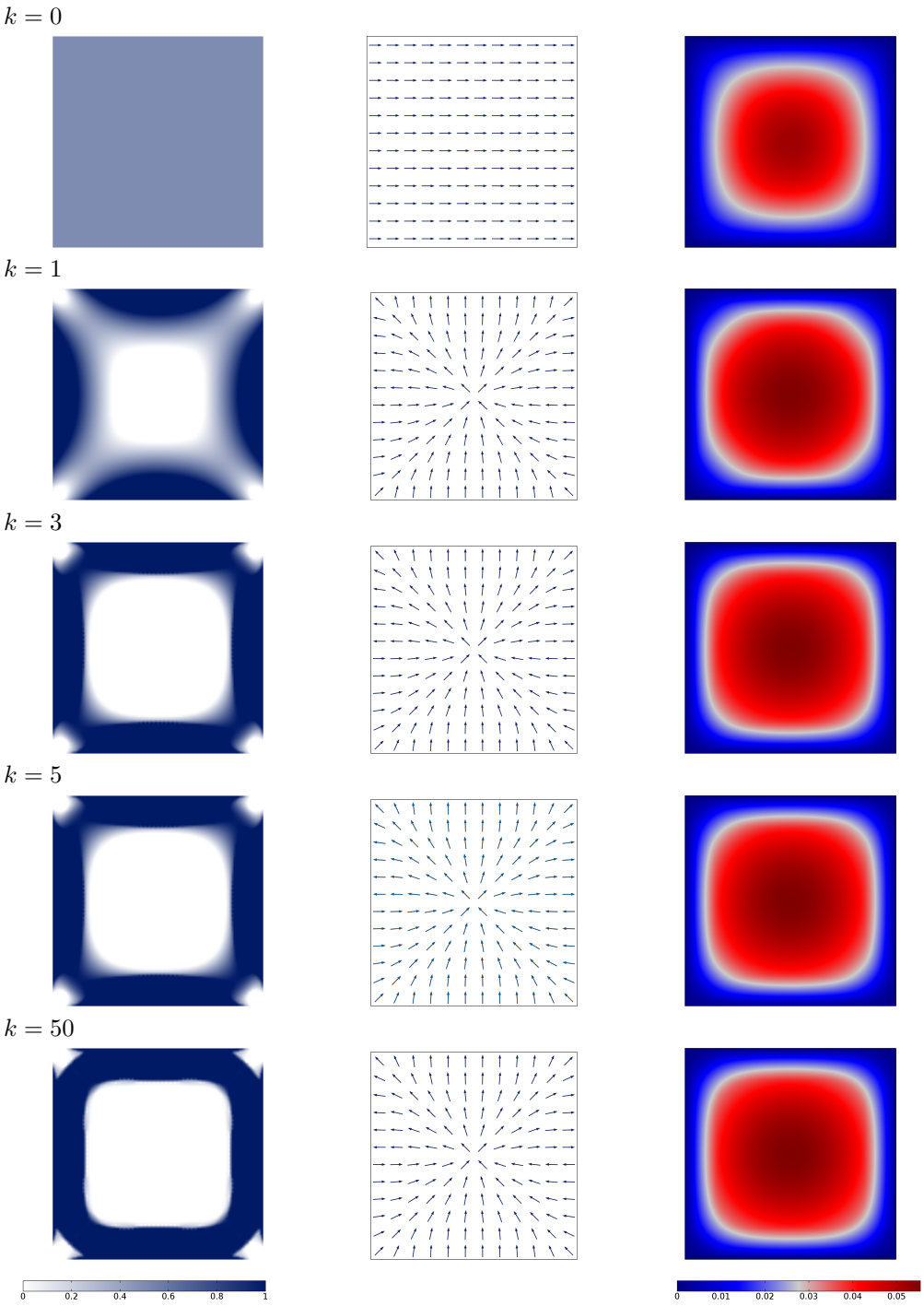

Figure 8.1.: Optimality criteria method: volume fraction θ, direction of lamination e and optimal state solution u for iteration steps k.

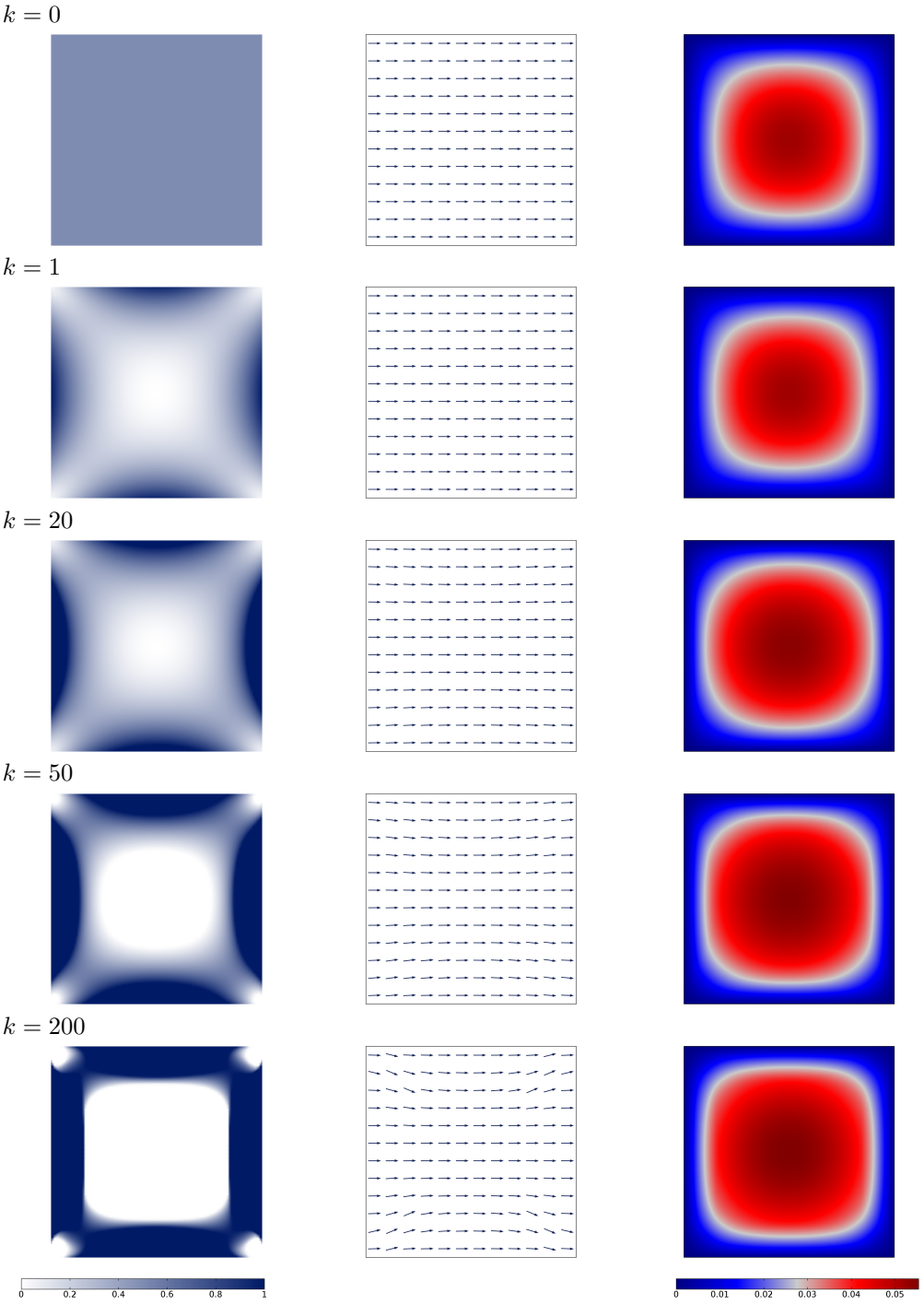

Figure 8.2.: Gradient Method: volume fraction θ, direction of lamination e and optimal state solution u for iteration steps k.

As Allaire states in [Allaire, 2002], for the given self-adjoint problem the optimality criteria method turns out to be a double minimization algorithm. For this reason, it is expected that the optimality criteria method converges faster than the gradient method. This is exactly what we see in the conducted simulations. The optimality criteria method yields almost a 0-1 design after only 50 steps (cf. figure 8.1). The gradient method on the other hand is not able to reach similarly good results after 50 iteration steps and requires 133 steps to achieve a comparably good objective function value, see figure 8.3.

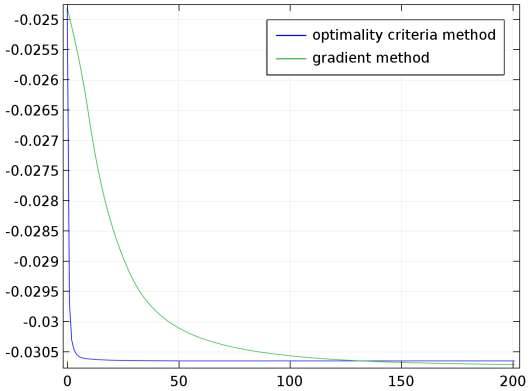

Figure 8.3.: Comparison of objective functional value in optimality criteria method (50 iteration steps and extrapolation) and gradient method (200 iteration steps)

The direct comparison of both methods also shows that the optimization for the problem proceeds differently.

After just one optimization step with the optimality criteria method, a large part of Ω already has adopted density values of 0 and 1. In the first iteration step, the lamination direction is aligned accordingly and does not change noticeably until step 50. After the third iteration step the optimal 0-1-design can be clearly identified. With step 5, it can also be seen in the objective functional in figure (8.3) that most of the optimization is completed and afterwards only a fine tuning in transition areas of the two individual phases is performed, which does not significantly change the objective functional value. The solution and observed behaviour of the implemented optimality gradient method matches the results from [Glowinski, 1983] and [Allaire, 2002] and thus serves as a starting point for validation of the implemented gradient method.

Considering the behaviour of the gradient method in figure 8.2, one observes that not only the optimization of the volume fraction θ develops very differently, that is a significantly slower development of the density to a 0-1-design, but also the optimization of the lamination direction e behaves differently. Not before the 0-1 design is clearly formed in step 50, a significant change in the lamination direction can be detected in regions of intermediate values of θ. At first view, the plot of the maintained optimal lamination direction after iteration step 200 differs from the one obtained by the optimality criteria method. Never-

theless, one has to take into account that in regions where $\theta = 1$ or $\theta = 0$ the lamination direction is completely irrelevant. In regions of interest, where the algorithm achieves a composite material, the lamination directions of both algorithms in step 50 respectively 200 are identical.
The simulation with optimality criteria method provide the same results as those presented in [Allaire, 2002]. Comparison of both methods verifies the implementation of the gradient method, which forms the basis for all subsequent enhancements. In the following we concentrate on the further development and application of the gradient method, because especially in chapter 9 the use of the gradient method is expedient.

8.3. Optimization in subdomain

To apply the described optimization methods to the problem of sensor optimization, we have to adopt the problem formulation. The new setting has to allow for optimization of the material in a subdomain of the given domain while we allow for various other not changing materials, not only consisting of composite materials of phase α and β, in the remaining part. According to our application, we further require that the adjusted objective functional is exclusively related to the to-be-optimized-part of the domain.
We adapt the setting of the 0-1-problem formulation in §8.3.1 and deduce the corresponding relaxed formulation in §8.3.2. On this basis, we derive the directional derivative of the relaxed objective functional in §8.3.3.

8.3.1. Setting of the problem

Unless stated otherwise, all definitions given above and requirements (7.1.11) and (7.1.12) on $g_{\alpha,\beta}$ and the partial derivatives $\frac{\partial g_{\alpha,\beta}}{\partial \lambda}$ apply.
Let Ω denote a fixed domain (bounded open set in R^n) and $\Omega_1 \subset \Omega$, $\Omega_2 \subset \Omega$ open subdomains of Ω such that $\Omega_1 \cup \Omega_2 \cup \Gamma_1 = \Omega$, $\Omega_1 \cap \Omega_2 = \emptyset$ and $\mu(\Gamma_1) = 0$ (see figure 8.4).

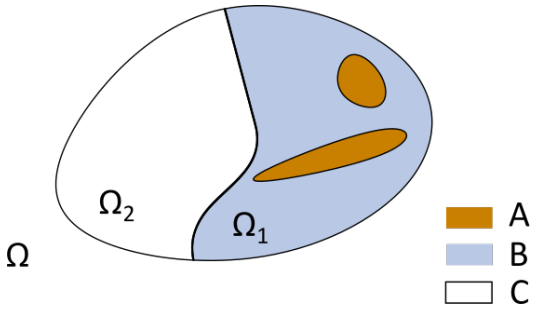

Figure 8.4.: Example for a domain Ω consisting of subdomains Ω_1 and Ω_2 and Γ_1. Ω_1 is filled with material B with inclusions of material A.

We optimize the material distribution of two isotropic materials A and B with material

parameters $0 < \alpha < \beta < +\infty$ in Ω_1, $\alpha, \beta \in \mathbb{R}$, whilst the arrangement of regions Ω_1 and Ω_2 and material C in Ω_2 with material parameter $\gamma(x) \in \mathbb{R}$, $0 < \gamma(x) < +\infty$ remains unaffected. For this aim, we introduce the characteristic functions

$$\chi_{\Omega_1}(x) = \begin{cases} 1 & x \in \Omega_1 \\ 0 & x \in \Omega \setminus \Omega_1 \end{cases} \tag{8.3.1}$$

and

$$\chi_\alpha(x) = \begin{cases} 1 & \text{phase } \alpha \text{ in } x \\ 0 & \text{phase } \beta \text{ in } x. \end{cases} \tag{8.3.2}$$

for phases $0 < \alpha < \beta < +\infty$.

Then the characteristic function $\chi(x)$

$$\chi(x) = \chi_{\Omega_1}(x)\chi_\alpha(x)$$

describes the part of Ω_1 occupied by phase α.

The overall material parameter is accordingly defined as

$$a_\chi(x) = \chi_{\Omega_1}(x)[\chi_\alpha(x)\alpha + (1 - \chi_\alpha(x))\beta] + (1 - \chi_{\Omega_1}(x))\gamma(x)$$

where $0 < \gamma < +\infty$ is the material parameter in Ω_2 not affected by the optimization. We assume again, that the materials follow a linear material law and are perfect bonding.

The state equation in Ω is consequently given by

$$\begin{cases} -\operatorname{div}(a_\chi(x)\nabla u_\chi(x)) = f(x) & \text{in } \Omega \\ u_\chi(x) = 0 & \text{on } \partial\Omega. \end{cases} \tag{8.3.3}$$

Furthermore, we assume that the amount of material A in Ω_1 is limited by a prescribed volume V_α of A, $0 \leq V_\alpha \leq |\Omega_1|$, $|\Omega_1|$ measure of Ω_1. This volume constraint is again included in the objective functional by introduction of the Lagrange Multiplier l. The objective functional evaluating the distribution of materials A and B in Ω_1 reads

$$J(\chi_\alpha) = \int_{\Omega_1} \chi_\alpha(x) g_\alpha(x, u_\chi(x)) + (1 - \chi_\alpha(x)) g_\beta(x, u_\chi(x)) \,\mathrm{d}x + l \int_{\Omega_1} \chi_\alpha(x) \,\mathrm{d}x. \tag{8.3.4}$$

We will derive at a later stage that a formulation of the objective functional respectively all included functions on Ω instead of Ω_1 is expedient. With $\tilde{g}_\alpha$ and $\tilde{g}_\beta$ defined by

$$\tilde{g}_\alpha(x, u(x)) = \chi_{\Omega_1}(x) g_\alpha(x, u(x)) \tag{8.3.5}$$

$$\tilde{g}_\beta(x, u(x)) = \chi_{\Omega_1}(x) g_\beta(x, u(x)). \tag{8.3.6}$$

and the definition of $\chi(x)$ we achieve a expression of the objective functional similar to (7.1)

$$J(\chi) = \int_\Omega \chi(x)\tilde{g}_\alpha(x, u_\chi(x)) + (1-\chi(x))\tilde{g}_\beta(x, u_\chi(x))\,\mathrm{d}x + l\int_\Omega \chi(x)\,\mathrm{d}x. \tag{8.3.7}$$

The complete optimal design problem reads

Find $\tilde{\chi}$ such that

$$\tilde{\chi} = \underset{\substack{\chi\in L^\infty(\Omega;\{0,1\})\\ \chi(x)=\chi_{\Omega_1}(x)\chi_\alpha(x)}}{\arg\inf} J(\chi).$$

with objective functional defined by

$$J(\chi) = \int_\Omega \chi(x)\tilde{g}_\alpha(x, u_\chi(x)) + (1-\chi(x))\tilde{g}_\beta(x, u_\chi(x))\,\mathrm{d}x + l\int_\Omega \chi(x)\,\mathrm{d}x \tag{8.3.8}$$

and u_χ is the solution of the state equation

$$\begin{cases} -\mathrm{div}(a_\chi(x)\nabla u_\chi(x)) = f(x) & \text{in } \Omega \\ u_\chi(x) = 0 & \text{on } \partial\Omega. \end{cases} \tag{8.3.9}$$

Conditions of $g_{\alpha,\beta}$ (7.1.11) and their partial derivatives (7.1.12) concerning measurability, continuity a.e. and growth conditions transfer to $\tilde{g}_{\alpha,\beta}$ and their partial derivatives, provided that Γ_1 has measure zero.
According to the argumentation in chapter 7, one cannot expect to find an optimal solution of the described optimization problem in the set of admissible designs. For this reason, we follow the theory of relaxation via homogenization.

8.3.2. Relaxation

We enlarge the set of admissible designs in Ω_1 to the set CD of composite designs and accordingly adopt the problem formulation. We now allow for composite materials in region Ω_1 whilst the material distribution in Ω_2 remains unaffected.
The relaxed problem formulation is

$$\min_{(\theta,A^*)\in CD} J^*(\theta, A^*) \tag{8.3.10}$$

with objective functional

$$J^*(\theta, A^*) = \int_{\Omega_1} [\theta(x)g_\alpha(x, u(x)) + (1-\theta(x))g_\beta(x, u(x)))]\,\mathrm{d}x + l\int_{\Omega_1} \theta(x)\,\mathrm{d}x, \tag{8.3.11}$$

with set of generalized admissible configurations in Ω_1

$$CD = \left\{(\theta, A^*) \in L^\infty(\Omega_1; [0,1] \times M_N^s | A^*(x) \in G_{\theta(x)} \text{ a.e. in } \Omega_1\right\} \tag{8.3.12}$$

and u the solution of

$$\left\{ \begin{array}{rll} -\mathrm{div}(\tilde{A}^*(x)\nabla u(x)) &= f(x) & \text{in } \Omega \\ u(x) &= 0 & \text{on } \partial\Omega \end{array} \right. , \tag{8.3.13}$$

where

$$\tilde{A}^*(x) = \chi_{\Omega_1} A^*(x) + (1 - \chi_{\Omega_1})\gamma(x). \tag{8.3.14}$$

Again it is expedient for the derivation of the directional derivative in §8.3.3 to strive for a formulation of the objective functional on Ω.

Therefore we define the adjusted set of composite designs

$$CD = \{(\tilde{\theta}, \tilde{A}^*) \in L^\infty(\Omega; [0,1] \times M_N^s) \mid \tilde{A}^*(x) \in G_{\tilde{\theta}(x)} \text{ a.e. in } \Omega_1\}$$

with modified $\tilde{\theta}(x)$

$$\tilde{\theta}(x) = \chi_{\Omega_1}\theta(x). \tag{8.3.15}$$

The objective functional is generalized to a formulation similar to (7.2.27) obtained in chapter 7

$$J^*(\tilde{\theta}, \tilde{A}^*) = \int_\Omega \tilde{\theta}(x)\tilde{g}_\alpha(x, u(x)) + (1 - \tilde{\theta}(x))\tilde{g}_\beta(x, u(x))\,\mathrm{d}x + l\int_\Omega \tilde{\theta}(x)\,\mathrm{d}x, \tag{8.3.16}$$

where $u(x)$ is the unique solution of

$$\left\{ \begin{array}{rll} -\mathrm{div}(\tilde{A}^*(x)\nabla u(x)) &= f(x) & \text{in } \Omega \\ u(x) &= 0 & \text{on } \partial\Omega. \end{array} \right. \tag{8.3.17}$$

The proposed relaxed problem is then

$$\min_{(\tilde{\theta}, \tilde{A}^*) \in CD} J^*(\tilde{\theta}, \tilde{A}^*). \tag{8.3.18}$$

Since the requirements for g_α and g_β and their partial derivatives are transferred directly to $\tilde{g}_\alpha$ and $\tilde{g}_\beta$ and the corresponding partial derivatives, the arguments of chapter 7 apply to the deduced relaxed problem setting.

8.3.3. Gâteaux differential of the relaxed objective functional

By introduction of the corresponding adjoint problem we eliminate again the dependency of the Gâteaux differential on δu.

The adjoint problem is given by

$$\begin{cases} -\mathrm{div}(\tilde{A}^*(x)\nabla p(x)) = \tilde{\theta}(x)\frac{\partial \tilde{g}_\alpha}{\partial \lambda}(x,u(x)) + (1-\tilde{\theta}(x))\frac{\partial \tilde{g}_\beta}{\partial \lambda}(x,u(x)) & \text{in } \Omega \\ p(x) = 0 & \text{on } \partial\Omega. \end{cases} \tag{8.3.19}$$

Theorem 8.3.1
The relaxed cost function is Gâteaux differentiable on CD with directional derivative

$$\delta J^*(\tilde{\theta},\tilde{A}^*) = \int_{\Omega_1} \delta\theta(x)\left[g_\alpha(x,u(x)) - g_\beta(x,u(x)) + l\right]\mathrm{d}x - \int_{\Omega_1} \delta A^*(x)\nabla u(x)\cdot\nabla p(x)\,\mathrm{d}x.$$

$\delta\tilde{\theta}$ and $\delta\tilde{A}^*$ are admissible increments in CD, u solution of the state equation (8.3.17) and p solution of the adjoint state equation (8.3.19)

Proof. Als already stated, we follow the diction in literature ([Allaire, 2002]) and denote the relaxed objective functional by $J^*(\theta, A^*)$ although we consider an objective functional which is still dependent on u. This dependence of the objective functional on the state u must be taken into account again when computing the directional derivative. We note once again that design parameters $(\theta(t), A^*(t))$ provide via solution of the state equation a path $u(t)$ of the state variable introducing the state increment δu.

On this basis we compute the directional derivative of J^*:

$$\begin{aligned} \delta J^*(\tilde{\theta},\tilde{A}^*) = \frac{\mathrm{d}}{\mathrm{d}t} J^*(\tilde{\theta}(t),\tilde{A}^*(t),u(t))\Big|_0 = \\ \int_\Omega \delta\tilde{\theta}(x)\left[\tilde{g}_\alpha(x,u(x)) - \tilde{g}_\beta(x,u(x)) + l\right]\mathrm{d}x \\ + \int_\Omega \delta u(x)\left[\tilde{\theta}(x)\frac{\partial \tilde{g}_\alpha}{\partial\lambda}(x,u(x)) + (1-\tilde{\theta}(x))\frac{\partial \tilde{g}_\beta}{\partial\lambda}(x,u(x))\right]\mathrm{d}x \end{aligned}$$

By definition of $\tilde{\theta}$ we can conclude

$$\begin{aligned}\int_\Omega \delta\tilde{\theta}(x)\left[\tilde{g}_\alpha(x,u(x))) - \tilde{g}_\beta(x,u(x)) + l\right] \mathrm{d}x &= \int_{\Omega_1} \delta\tilde{\theta}(x)\left[\tilde{g}_\alpha(x,u(x)) - \tilde{g}_\beta(x,u(x)) + l\right] \mathrm{d}x \\ &= \int_{\Omega_1} \delta\theta(x)\left[g_\alpha(x,u(x))) - g_\beta(x,u(x)) + l\right] \mathrm{d}x\end{aligned}$$

We can now eliminate the dependence of the directional derivative on the state increment δu.

By differentiating the state equation (8.3.17) we obtain δu as unique solution of

$$\begin{cases} -\mathrm{div}(\tilde{A}^*(x)\nabla\delta u(x)) = \mathrm{div}(\delta\tilde{A}^*(x)\nabla u(x)) & \text{in } \Omega \\ \delta u(x) = 0 & \text{on } \partial\Omega. \end{cases} \tag{8.3.20}$$

Multiplying (8.3.20) by p and integrating by parts yields

$$\begin{aligned}\int_\Omega \langle\tilde{A}^*(x)\nabla\delta u(x), \nabla p(x)\rangle \,\mathrm{d}x &= \int_\Omega \langle\delta\tilde{A}^*(x)\nabla u(x), \nabla p(x)\rangle \,\mathrm{d}x \\ &+ \int_{\partial\Omega} \langle\tilde{A}^*(x)\nabla\delta u(x)\cdot\nu, p(x)\rangle \,\mathrm{d}\sigma_x \\ &+ \int_{\partial\Omega} \langle\delta\tilde{A}^*(x)\nabla u(x)\cdot\nu, p(x)\rangle \,\mathrm{d}\sigma_x.\end{aligned}$$

Multiplying the adjoint equation (8.3.19) by δu and integrating by parts yields

$$\begin{aligned}\int_\Omega \langle\tilde{A}^*(x)\nabla p(x), \nabla\delta u(x)\rangle \,\mathrm{d}x &= \int_\Omega \left[\tilde{\theta}(x)\frac{\partial\tilde{g}_\alpha}{\partial\lambda}(x,u(x)) + (1-\tilde{\theta}(x))\frac{\partial\tilde{g}_\beta}{\partial\lambda}(x,u(x))\right]\delta u(x)\,\mathrm{d}x \\ &+ \int_{\partial\Omega} \langle\tilde{A}^*(x)\nabla p(x)\cdot\nu, \delta u\rangle \,\mathrm{d}x.\end{aligned}$$

With the corresponding boundary conditions we deduce

$$\int_\Omega \delta u(x)\left[\theta(\tilde{x})\frac{\partial\tilde{g}_\alpha}{\partial\lambda}(x,u(x)) + (1-\tilde{\theta})\frac{\partial\tilde{g}_\beta}{\partial\lambda}(x,u(x))\right]\mathrm{d}x = -\int_\Omega \delta\tilde{A}^*(x)\nabla u(x)\cdot\nabla p(x)\,\mathrm{d}x.$$

With the definition of $\tilde{A}^*$ we get

$$-\int_\Omega \delta\tilde{A}^*(x)\nabla u(x)\cdot\nabla p(x)\,\mathrm{d}x = -\int_{\Omega_1} \delta\tilde{A}^*(x)\nabla u(x)\cdot\nabla p(x)\,\mathrm{d}x = -\int_{\Omega_1} \delta A^*(x)\nabla u(x)\cdot\nabla p(x)\,\mathrm{d}x,$$

which finally leads to

$$\delta J^*(\tilde{\theta}, \tilde{A}^*) = \int_{\Omega_1} \delta\theta(x) \left[g_\alpha(x, u(x)) - g_\beta(x, u(x)) + l \right] \mathrm{d}x - \int_{\Omega_1} \delta A^*(x) \nabla u(x) \cdot \nabla p(x) \, \mathrm{d}x.$$

□

The derived formulation of $\delta J^*(\tilde{\theta}, \tilde{A}^*)$ completely matches the formulation of $\delta J^*(\theta, A^*)$ in chapter 7, except for the difference that it is confined to the region Ω_1. The derivation of optimality criteria in Ω_1 and the optimality of simple laminates can therefore directly be transferred as well as the formulation of the gradient algorithm.

8.3.4. Application

To validate the derived gradient method on a subdomain, we slightly modify the problem formulated in §8.2 above. This procedure has the advantage that the optimal design can be predicted by experience and thus the functionality of the algorithm can be easily validated.

We now consider the minimization problem

$$\min_{(\theta, A^*) \in CD} J^*(\theta, A^*) = \min_{(\theta, A^*) \in CD} - \int_{\Omega_1} u(x) \, \mathrm{d}x + l \int_{\Omega_1} \theta(x) \, \mathrm{d}x,$$

on the subdomain $\Omega_1 = (0.5, 1) \times (0, 1)$ of $\Omega = (0, 1)^2$ with u solution of

$$\begin{cases} -\mathrm{div}(A^*(x) \nabla u(x)) = 1 & \text{in } \Omega \\ u(x) = 0 & \text{on } \partial\Omega \end{cases} . \tag{8.3.21}$$

We choose material parameters $\alpha = 1$, $\beta = 2$ and a volume constraint of 50% of phase A in Ω_1, which is again controlled by adaptation of the Lagrange Multiplier l as described in §8.1. The material parameter in the not-to-be-optimized region Ω_2 equals $\beta = 2$.

As before we initialize the problem with a constant volume fraction $\theta = 0.5$ and constant lamination direction $(1, 0)^T$.

The simulation is performed on a triangular mesh with quadratic Lagrange elements resulting in 12765 DOF.

Based on the optimization results in §8.2 it is expected that material A is again distributed along the edges leaving out the corners. Nevertheless, one expects an influence of the change of the optimization area on the resulting design especially in areas close to the interface between Ω_1 and Ω_2.

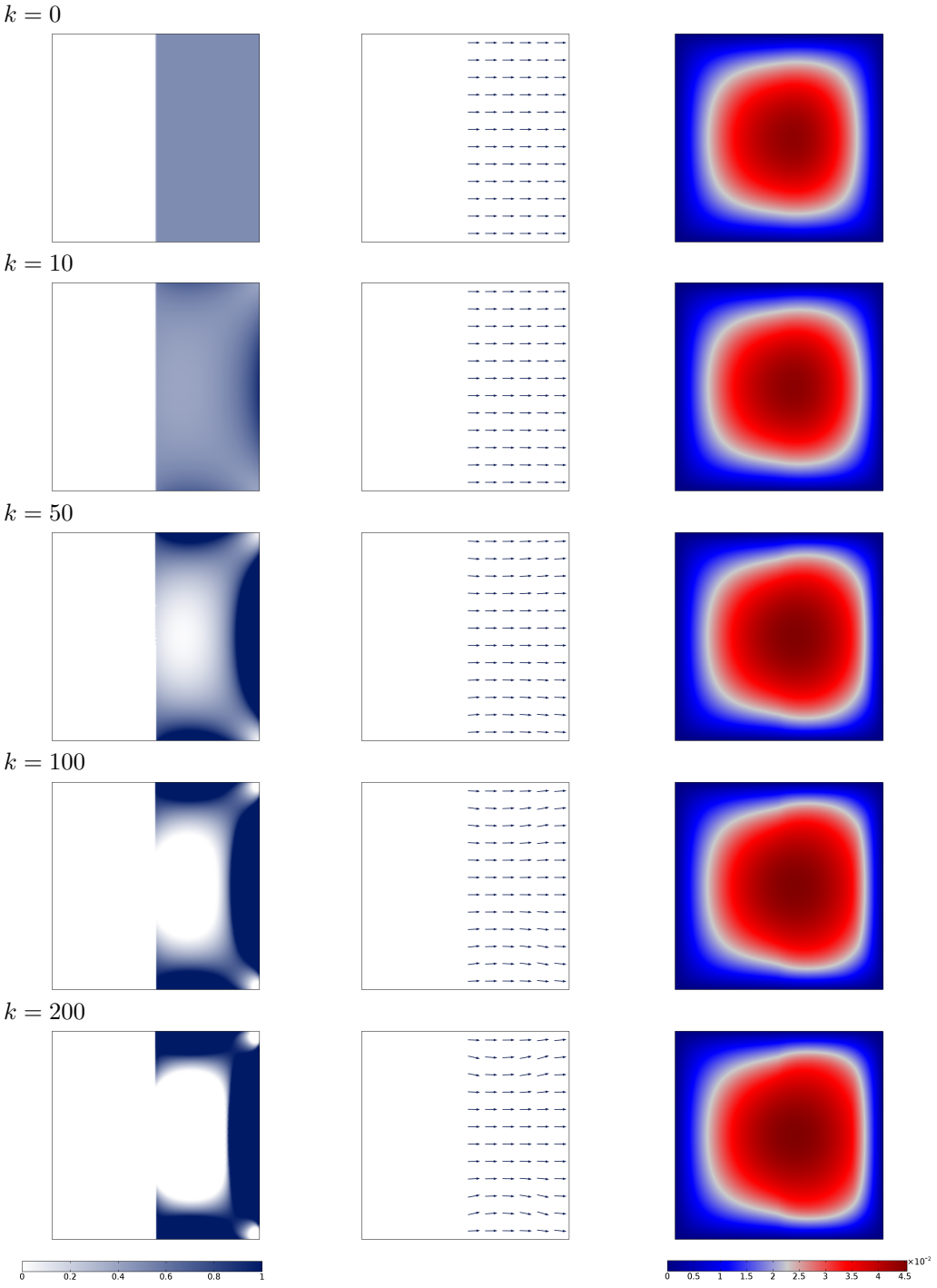

Figure 8.5.: Gradient Method in subdomain: volume fraction θ, direction of lamination e and optimal state solution u for iteration steps k.

Figure 8.5 illustrates the process of the gradient method for the given problem. Starting with constant density θ and lamination direction e for $k = 0$, the optimal design develops as expected. Interpreting the design problem again in the context of the best possible insulating design in stationary heat conduction, material A, with better isolating properties, is distributed successively as in the corresponding problem of §8.2, namely along the edges leaving out the corners. Just like in the optimization process from §8.2, the laminate direction is gradually adjusted only in regions where intermediate densities are present.

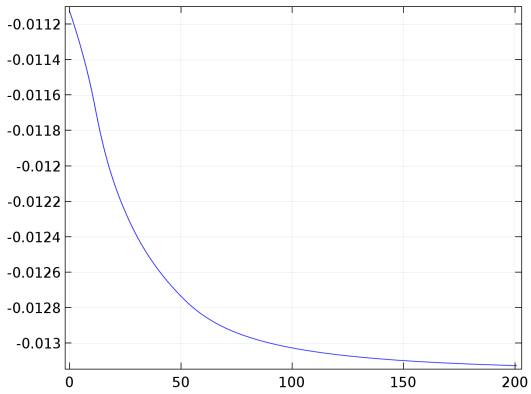

Figure 8.6.: Objective functional value for gradient method on subdomain.

The fact that the optimization only takes place on the sub-domain becomes clear at the interface between Ω_1 and Ω_2. Here the optimal design differs significantly from the one from §8.2 both in density θ and lamination direction e.
Figure 8.6 confirms again that the method minimizes the objective functional on the sub-domain Ω_1.

8.4. Gradient method in 3d

To make the described method useful for applications where a three dimensional setup cannot easily be reduced to a model in 2d and the full 3d modelling of the setup is required, as for example in models containing dipole sources or non-symmetric experimental setups, we extend the algorithm to 3d applications. In the course of this, we formulate the gradient method in 3d in §8.4.1 which is still based on design parameters θ and lamination direction e, in three dimensions determined by two rotation angles φ and ψ. In §8.4.2, we verify our implementation by 3d-modification of the example of §8.2.

8.4.1. Algorithm

In three dimensions, our design parameters are the density θ and the lamination direction e of the composite, which corresponds to two rotation angles φ and ψ of the rank-1 laminate

tensor. An optimal tensor is thus given by

$$A^*(\theta,\psi,\varphi) = R_1(\psi)R_2(\varphi)\begin{pmatrix}\lambda_\theta^- & 0 & 0\\ 0 & \lambda_\theta^+ & 0\\ 0 & 0 & \lambda_\theta^+\end{pmatrix}R_2^{-1}(\varphi)R_1^{-1}(\psi)$$

with rotation matrices

$$R_1(\psi) = \begin{pmatrix}\cos(\psi) & -\sin(\psi) & 0\\ \sin(\psi) & \cos(\psi) & 0\\ 0 & 0 & 1\end{pmatrix}$$

and

$$R_2(\varphi) = \begin{pmatrix}\cos(\varphi) & 0 & \sin(\varphi)\\ 0 & 1 & 0\\ -\sin(\varphi) & 0 & \cos(\varphi)\end{pmatrix}.$$

At this point it must be noted that in the following we use the so-called Z-Y-X Euler angles (see [Craig, 1986] for details), where the position of a body-fixed frame B in space is determined by the three angles ψ_E, θ_E and φ_E. Starting with the frame B which coincides with the spatial frame with axes x, y and z, B is first rotated about z by the angle ψ_E which transforms the frame to x', y' and $z' = z$. In a next step, B is rotated about y' by the angle θ_E providing x'', $y'' = y'$ and z'' and in a last step about x'' by the angle φ_E, leading to $x''' = x''$, y''' and z'''.

In order to avoid confusion and since we need only two rotation angles to describe the lamination direction e, we deviate from the usual notation at this point and define the two angles describing the lamination direction by $\psi = \psi_E$ and $\varphi = \theta_E$.

The directional derivative δJ^* of the objective functional $J^*(\theta,\psi,\varphi)$ with respect to an admissible increment $(\delta\theta,\delta\psi,\delta\varphi)$ is then computed as

$$\begin{aligned}\delta J^*(\theta,\psi,\varphi) = &\int_\Omega \left(\frac{\partial A^*}{\partial\psi}(x)\nabla u(x)\cdot\nabla p(x)\right)\delta\psi(x)\,\mathrm{d}x\\ &+\int_\Omega \left(\frac{\partial A^*}{\partial\varphi}(x)\nabla u(x)\cdot\nabla p(x)\right)\delta\varphi(x)\,\mathrm{d}x\\ &+\int_\Omega Q(x)\delta\theta\,\mathrm{d}x,\end{aligned}$$

with

$$Q(x) = g_\alpha(x,u(x)) - g_\beta(x,u(x)) + l - \left(\frac{\partial A^*}{\partial\theta}(x)\nabla u(x)\cdot\nabla p(x)\right).$$

The gradient method for the given minimization problem is defined accordingly.

Gradient method:

Initialization: Initialize θ_0, ψ_0 and φ_0 and compute A^*.
For simplicity choose constant θ_0 and constant angles ψ_0 and φ_0.

Iteration for $k \geq 0$: until convergence

1. Compute state u_k and adjoint state p_k as solutions of the corresponding problems with the previous design parameters θ_k, ψ_k and φ_k.
2. Update parameters by

$$\begin{aligned}
\psi_{k+1} &= \psi_k - t_k \left(\frac{\partial A^*}{\partial \psi}(\theta_k, \psi_k, \varphi_k) \nabla u_k \cdot \nabla p_k \right) \\
\varphi_{k+1} &= \varphi_k - t_k \left(\frac{\partial A^*}{\partial \varphi}(\theta_k, \psi_k, \varphi_k) \nabla u_k \cdot \nabla p_k \right) \\
\theta_{k+1} &= \max(0, \min(1, \theta_k - t_k Q_k))
\end{aligned}$$

with t_k a small step such that $J^*(\theta_{k+1}, \psi_{k+1}, \varphi_{k+1}) < J^*(\theta_k, \psi_k, \varphi_k)$.

8.4.2. Application

In order to validate the derived and implemented gradient method in 3d we choose an application that corresponds to the 2d application.
We consider again the optimization problem

$$\min_{(\theta, A^*) \in CD} J^*(\theta, A^*) = \min_{(\theta, A^*) \in CD} - \int_\Omega u(x) \, \mathrm{d}x + l \int_\Omega \theta(x) \, \mathrm{d}x,$$

with u solution of

$$\begin{cases} -\mathrm{div}(A^*(x) \nabla u(x)) = 1 & \text{in } \Omega \\ u(x) = 0 & \text{on } \partial\Omega \end{cases} \tag{8.4.1}$$

and adjoint state $p = -u$, now on $\Omega = (0,1)^3$ with $\alpha = 1$, $\beta = 2$ and a volume constraint of 50% of phase A, again controlled by l as described in §8.1.
According to the application in 2d, we expect as result of the optimization routine a 0-1-design, distributing material A along the edges of Ω leaving void the corners.
We initialize the problem with a constant volume fraction $\theta = 0.5$ and constant lamination direction $(1,0,0)^T$. The 3d simulations are performed on a tetrahedral mesh with quadratic

Lagrange elements resulting in 23191 DOF.

Figures 8.7 and 8.8 illustrate the optimization process after iteration steps 10, 20, 50, 100 and 200 of the described algorithm based on 3d-plots of the density θ and the solution u. Figures 8.9 and 8.10 deepen the insight into the optimization process through 2d-extracts of the same process after the same iteration steps. We display density θ and lamination direction e exemplary in the xy-cut-plane of Ω for $z = 0.5$.

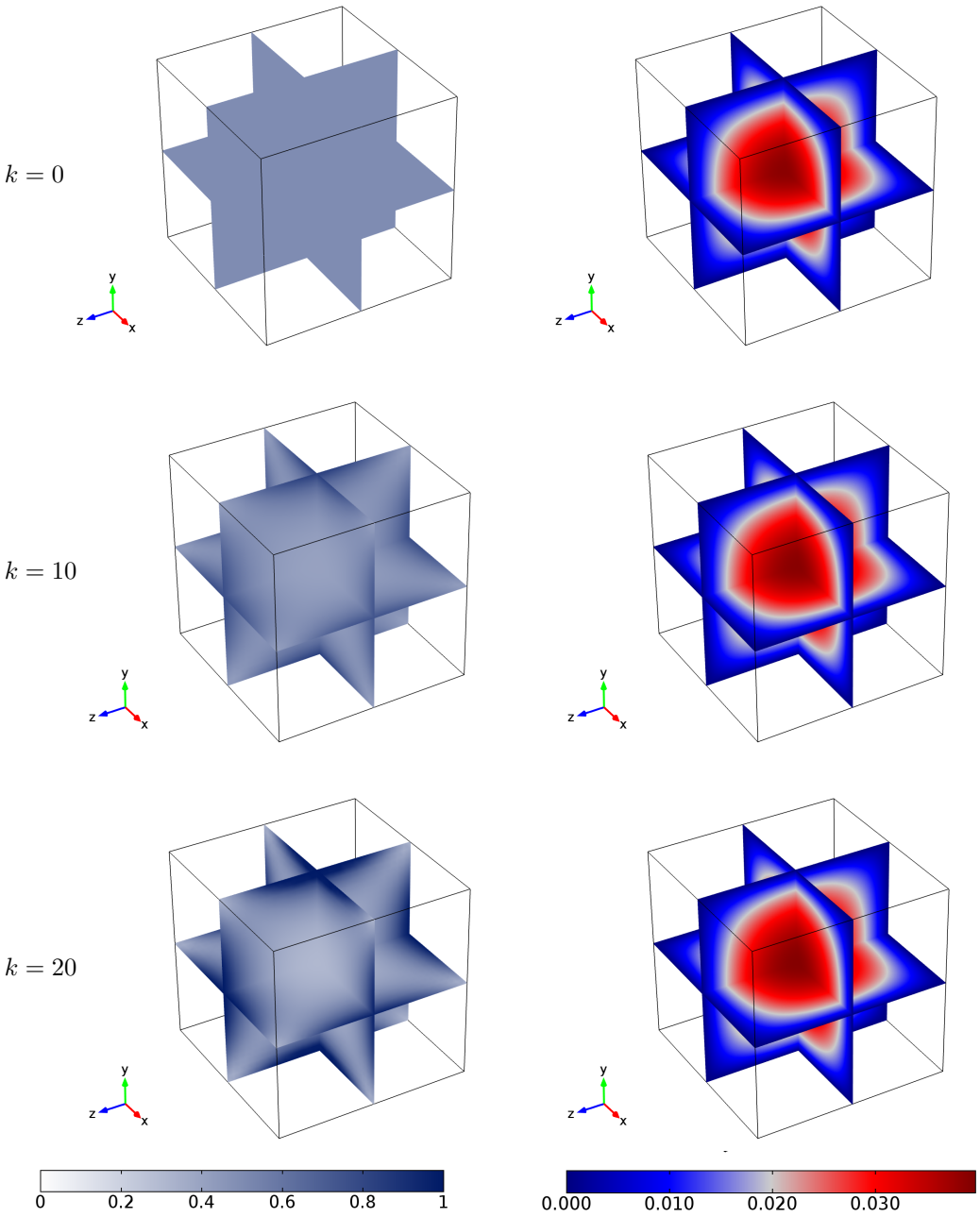

Figure 8.7.: Initialization ($k = 0$) and optimization status after $k = 10$ and $k = 20$ steps of the gradient method in 3d. Density θ (left) and solution u (right).

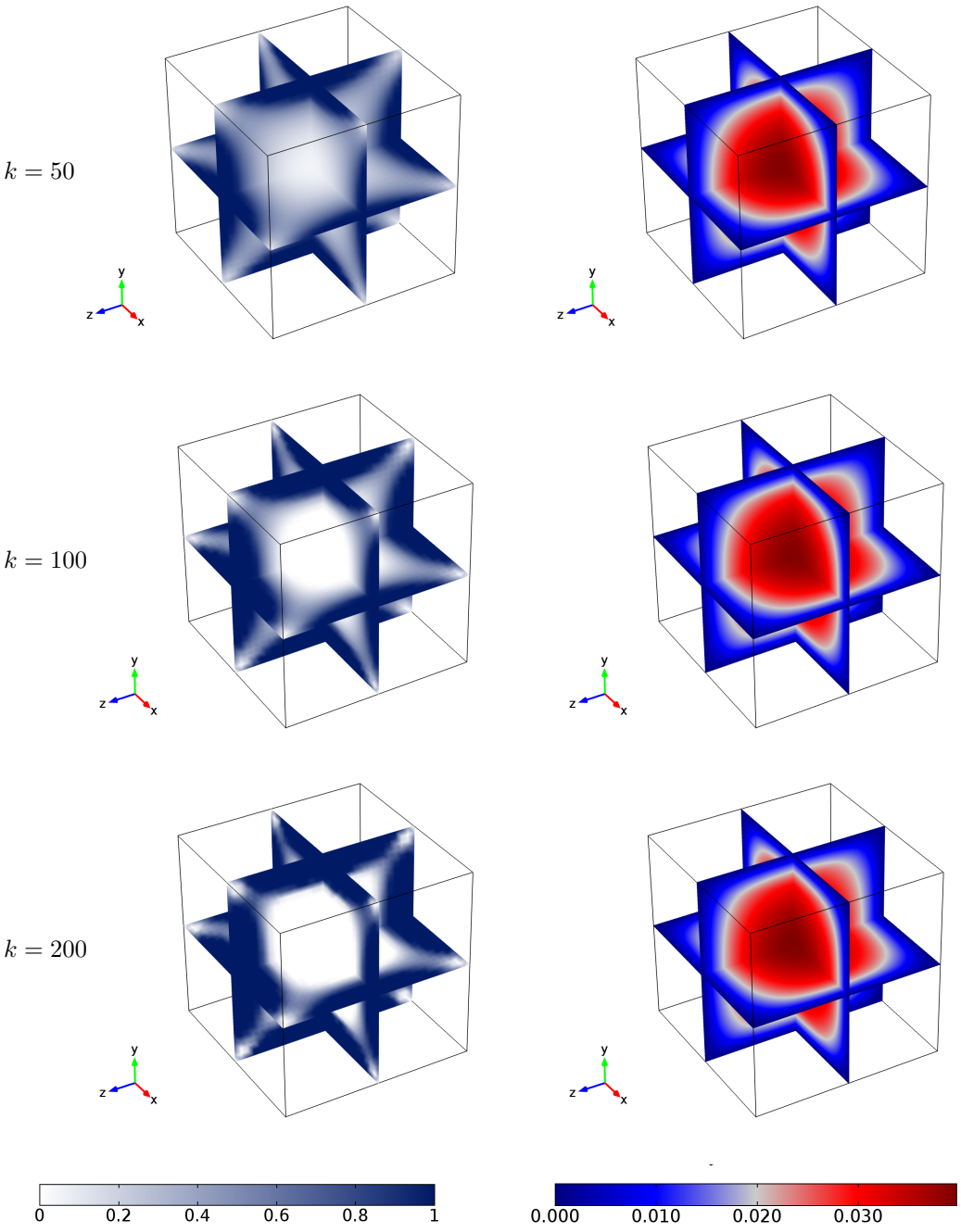

Figure 8.8.: Optimization status after $k = 50$, $k = 100$ and $k = 200$ steps of the gradient method in 3d. Density θ (left) and solution u (right).

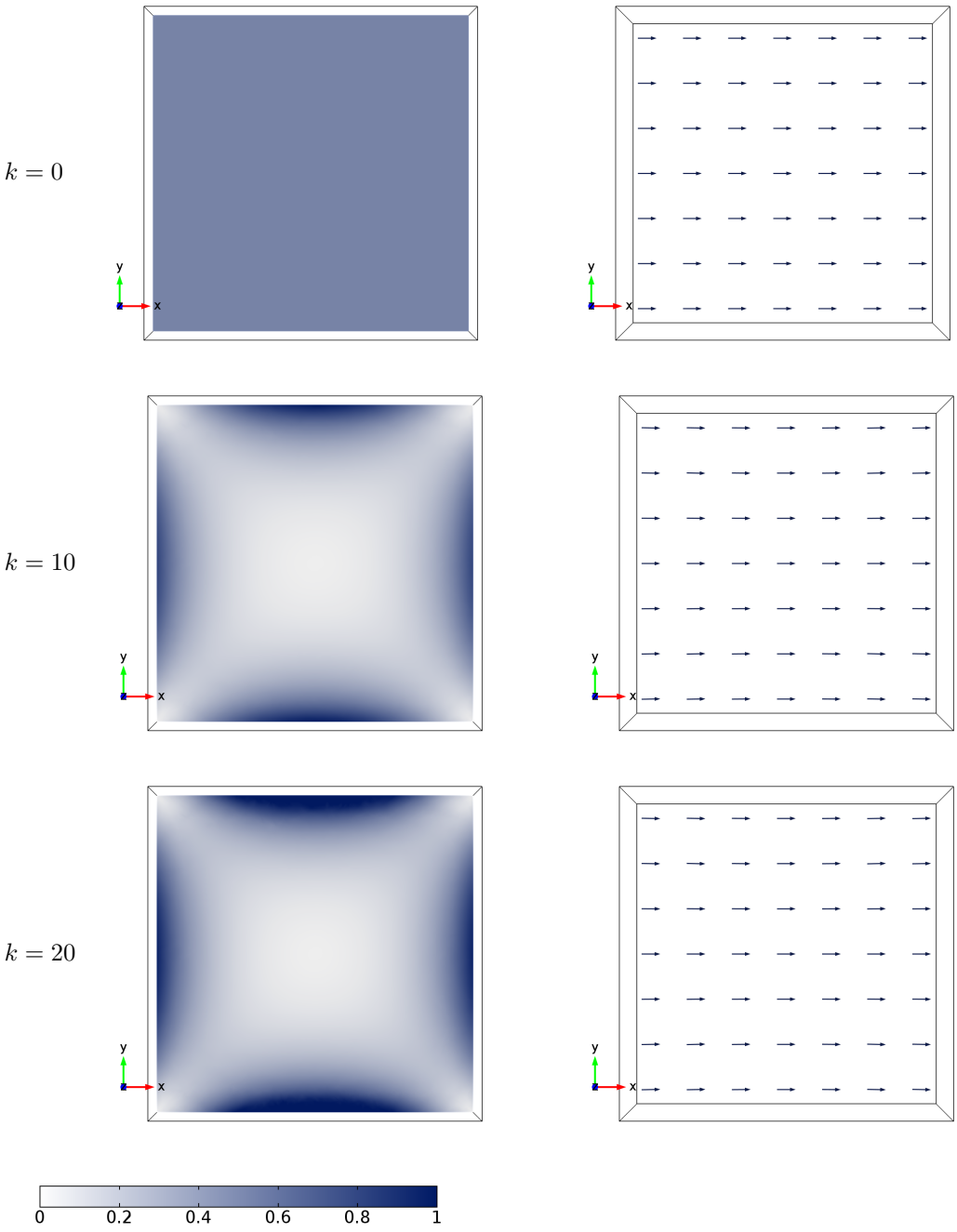

Figure 8.9.: Initialization ($k = 0$) and optimization status after $k = 10$ and $k = 20$ steps of the gradient method in 3d. Density θ (left) and lamination direction e (right) in xy-cutplane at $z = 0.5$.

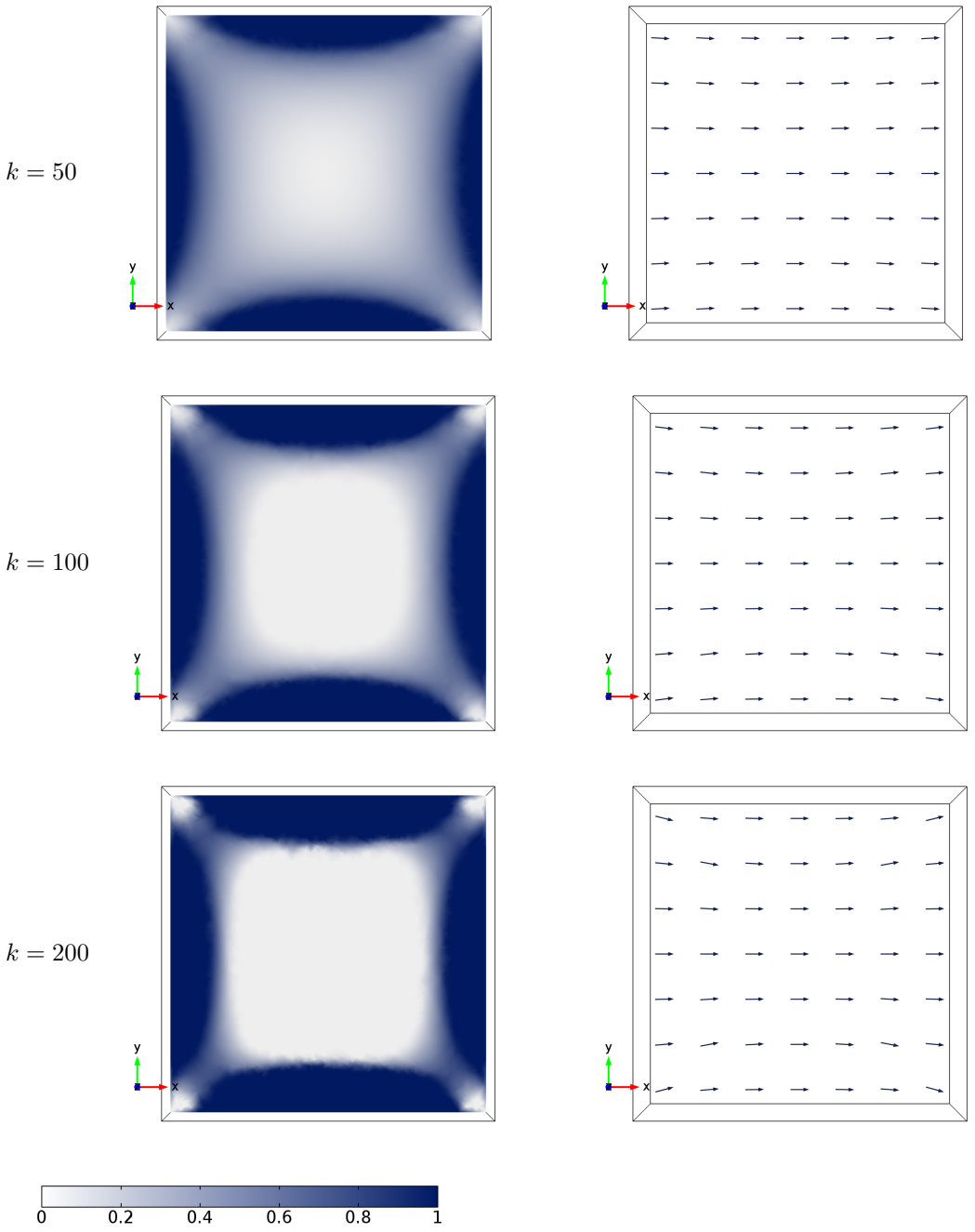

Figure 8.10.: Optimization status after $k = 50$, $k = 100$ and $k = 200$ steps of the gradient method in 3d. Density θ (left) and lamination direction e (right) in xy-cutplane at $z = 0.5$

The pictures show that the method works as expected. After 200 iteration steps, we almost achieve a 0-1 design with few regions of intermediate densities (see figures 8.7 and 8.8 left). Figures 8.9 and 8.10 illustrate again that the optimization process is analogous to the 2d case. While already from the beginning one can see a clear progress in the optimization of the density, at the earliest from step 50 on, one can see a significant optimization of the lamination direction. As in 2d, the lamination direction is only optimized in areas of intermediate densities.

9. Homogenization method with complex-valued material parameters

Based on the explanations in §6.2 we aim at extension of the established theory of chapter 7 to the case of complex material parameters α, $\beta \in \mathbb{C}$ in order to make the theory suitable for the setting of sensor optimization. We describe the adjusted problem setting in §9.1. A procedure along the lines of the argumentation of chapter 7 would involve relaxation via homogenization of the introduced optimization problem including characterization of the set of composite materials. In §9.2 we state why this is not readily possible in the described setting. Nevertheless, assuming the existence of a suitable relaxed problem formulation, we derive the directional derivative of the objective functional in §9.3. Based on a further adjusted problem setting introduced in §9.4 we are able to deduce a gradient method in §9.5.

9.1. Setting of the problem

We now consider the distribution of two materials A and B with constant isotropic material parameters $\alpha = \alpha_r + \mathrm{i}\alpha_i$ and $\beta = \beta_r + \mathrm{i}\beta_i$, $\alpha, \beta \in \mathbb{C}$ in the given domain Ω. We further demand $\alpha_r, \beta_r > 0$ and $\alpha_i, \beta_i \geq 0$ in order to set up a physically reasonable problem.
The characteristic function

$$\chi(x) = \begin{cases} 1 & \text{phase } A \text{ is present at point } x \\ 0 & \text{phase } B \text{ is present at point } x \end{cases} \tag{9.1.1}$$

defines the part of Ω occupied by phase A and the overall material parameter is accordingly formulated as

$$a_\chi = \alpha\chi(x) + \beta(1 - \chi(x)). \tag{9.1.2}$$

The **state equation** of our optimization problem models now the electric potential u_χ in the domain Ω

$$\begin{cases} -\mathrm{div}(a_\chi(x)\nabla u_\chi(x)) = f(x) & \text{in } \Omega \\ u_\chi(x) = 0 & \text{on } \partial\Omega, \end{cases} \tag{9.1.3}$$

where u_χ is the unknown function, which is now complex-valued, f a given source term in Ω, scalar and independent of χ, and the materials A and B are linear and perfect bonding.

Provided that the source term f belongs to $H^{-1}(\Omega)$ we deduce that the standard weak form of (9.1.3) admits a unique solution u_χ in $H_0^1(\Omega)$ (cf. §9.1.1).

We assume again that the amount of material A is limited by a prescribed volume V_α of A, $0 \leq V_\alpha \leq |\Omega|$, $|\Omega|$ measure or volume of Ω.
An **admissible design** is therefore a function χ such that

$$\chi \in L^\infty(\Omega; \{0,1\}) \text{ and } \int_\Omega \chi(x)\,\mathrm{d}x = V_\alpha. \tag{9.1.4}$$

We denote by U_{ad} the **set of admissible configurations**:

$$U_{\text{ad}} = \left\{ \chi \in L^\infty(\Omega; \{0;1\}) \text{ such that } \int_\Omega \chi(x)\,\mathrm{d}x = V_\alpha \right\}. \tag{9.1.5}$$

The objective functional is universally formulated as

$$J(\chi) = \int_\Omega \chi(x) g_\alpha(x, u_\chi(x), \bar{u}_\chi(x)) + (1-\chi(x)) g_\beta(x, u_\chi(x), \bar{u}_\chi(x))\,\mathrm{d}x.$$

In this formulation g_α and g_β are not only dependent on the solution u_χ of the state equation, but also on its complex conjugate $\bar{u}_\chi$. As the objective functional $J(\chi)$ is commonly a real-valued function depending on the complex-valued u it is also implicitly dependent on $\bar{u}$.
For example, the objective functional in our applications in chapter 10

$$J(\chi) = \int_\Omega \chi(x) |u_\chi(x)|^2\,\mathrm{d}x,$$

a proxy for the energy captured at a sensor made of material A, must be understood as follows: we interpret the function g_β depending on x, u_χ and additionally on $\bar{u}_\chi$ with

$$g_\beta(x, u(x)) = |u_\chi(x)|^2 = u(x)\bar{u}(x) = g_\beta(x, u_\chi(x), \bar{u}_\chi(x)). \tag{9.1.6}$$

Then, the objective functional for the applications reads

$$J(\chi) = \int_\Omega \chi(x) g_\beta(x, u_\chi(x), \bar{u}_\chi(x))\,\mathrm{d}x. \tag{9.1.7}$$

Instead of enforcing the volume constraint $\int_\Omega \chi(x)\,\mathrm{d}x = V_\alpha$ in the set of admissible designs, we introduce a Lagrange Multiplier $l \in \mathbb{R}$ in the objective functional, as before.
The complete formulation of our optimal design problem is then stated as:

Find $\tilde{\chi}$ such that

$$\tilde{\chi} = \arg\inf_{\chi \in U_{ad}} J(\chi),$$

where the real-valued objective functional J is defined by

$$J(\chi) = \int_\Omega \chi(x) g_\alpha(x, u_\chi(x), \bar{u}_\chi(x)) + (1 - \chi(x)) g_\beta(x, u_\chi(x), \bar{u}_\chi(x)) \, \mathrm{d}x + l \int_\Omega \theta(x) \, \mathrm{d}x$$

and u_χ is the solution of the state equation

$$\begin{cases} -\mathrm{div}(a_\chi(x) \nabla u_\chi(x)) = f(x) & \text{in } \Omega \\ u_\chi(x) = 0 & \text{on } \partial\Omega. \end{cases} \tag{9.1.8}$$

9.1.1. Solution of the state equation

Solvability and uniqueness of the solution $u_\chi \in H_0^1(\Omega)$ for the standard weak form of the state equation (9.1.8) follows again from application of Riezs representation theorem and a less familiar version of Lax–Milgram theorem for coercive sesquilinear forms that we state here for the sake of completeness:

Lemma 9.1.1
Let V be a Hilbert space over $\mathbb{C}$ and let $a : V \times V \to \mathbb{C}$ be a sesquilinear form satisfying for all $x, y \in V$

$$|a(x, y)| \leq C_0 \|x\|_V \|y\|_V \tag{9.1.9}$$

$$\Re\{a(x, x)\} \geq c_0 \|x\|_V^2 \tag{9.1.10}$$

with real constants C_0 and c_0.
Then there exists a unique operator $A : V \to V$ satisfying for all $x, y \in V$

$$a(y, x) = (y, Ax)_V. \tag{9.1.11}$$

In particular A is invertible and satisfies

$$A \in L(V, V^*),\ A^{-1} \in L(V^*, V),\ \|A\| \leq C_0 \text{ and } \|A^{-1}\| \leq \frac{1}{c_0}. \tag{9.1.12}$$

9.1.2. Direct method of the calculus of variations

The properties of the functions $g_{\alpha,\beta}$ and partial derivatives $\frac{\partial g_{\alpha,\beta}}{\partial \lambda}$ ensure continuity of the relaxed objective functional and existence of the Gâteaux differential in the real-valued

parameter setting.
Careful consideration of the proof of continuity of Nemytskii operators in [Showalter, 1997], using Lebesgue's dominated convergence theorem, which is formulated in $\mathbb{C}$ in [Alt, 2012] confirms, that the equivalent properties of $g_{\alpha,\beta}$, i.e. Caratheodory conditions and growth conditions

$$\begin{cases} g_{\alpha,\beta}(x,\lambda) \text{ is } \textbf{measurable} \text{ in } x \text{ for each fixed } \lambda \in \mathbb{C} \\ g_{\alpha,\beta}(x,\lambda) \text{ is } \textbf{continuous} \text{ for a.e. } x \in \Omega \\ |g_{\alpha,\beta}(x,\lambda)| \leq k(x) + C|\lambda|^m \text{ with } k \in L^1(\Omega),\ 1 \leq m < \frac{2N}{N-2}. \end{cases} \tag{9.1.13}$$

are required in the same way for the complex-valued parameter case.
We have not yet used the implicit dependence of the functions $g_{\alpha,\beta}(x,u(x))$ on the complex conjugate $\bar{u}$ here. This dependency becomes relevant when considering the partial derivatives. However, since this requires the definition of the so-called Wirtinger derivatives, which is discussed in §9.3.1, we refer to §9.3.2 for the requirements for the partial derivatives.

9.2. Towards relaxation of the problem

Based on the problems of solvability of the optimization problem stated above, we strive for adaptation of the relaxation via homogenization method used in chapter 7 to the more general case of complex-valued material parameters α, $\beta \in \mathbb{C}$.
From a descriptive point of view, the argumentation of relaxation via homogenization runs completely along the argumentation in the real-valued parameter setting. Naturally, one expects that consideration of composite materials in the set of admissible designs and a corresponding adaptation respectively relaxation of the objective functional solves the above-mentioned problems.
In order to approach a relaxation via homogenization procedure in the context of the complex-valued parameter setting, we recap the essential details for the success of the optimization by homogenization process in chapter 7 and then point out the challenges that arise in the more general case of complex material parameter input.
For isotropic materials with parameters α, $\beta \in \mathbb{R}$, an explicit description of the G-closure $\mathcal{G}_\theta$ can be achieved based on the theory of H-convergence. This explicit characterization of the set of composite materials enables the successful derivation of the directional derivative and necessary optimality conditions. Main ingredient of many of the proofs in the relaxation process, among those the proofs of arithmetic and harmonic mean bounds and the necessary optimality criteria, is the hermiteness of symmetric matrices in $\mathbb{R}^{N\times N}$ and the subsequent symmetry of the bilinear form (Ax,x). Simple laminates consisting of two isotropic materials with parameters α, $\beta \in \mathbb{R}$ have one eigenvalue equal to the harmonic mean λ_θ^- and all other eigenvalues equal to the arithmetic mean λ_θ^+. This fact finally

provides equality in harmonic and arithmetic mean bounds for simple laminates with lamination in direction of the eigenvector corresponding to λ_θ^- and leads to the conclusion that finding the point-wise optimal composite material boils down to finding an optimal rank-1 laminate.

Even though some properties of the homogenized tensor of composite materials in $\mathbb{C}$ are already described in literature, a closed chain of argumentation as in chapter 7 is not yet possible.

It is obvious that in the case of complex material parameters we cannot claim hermiteness of the tensors, rank-1 laminates are simple counterexamples. For this reason, the argumentation can certainly not be completely analogous to the real-valued parameter setting. From general considerations on Maxwell's equations and the complex dielectric constant, Milton claims symmetry of the tensors and positive semi-definiteness of the imaginary part for positive real frequencies ω [Milton, 2002]. Apart from that, several bounds on the coefficients of homogenized tensors are known. The equivalent to the Wiener bounds (7.2.14) of the real-valued parameter setting is the restriction of the diagonal elements of the complex tensor to lens-shaped regions in the complex plane as for example described in [Milton, 1980].

However, starting point for an application along the lines of the argumentation of chapter 7 would be an explicit characterization of the set of admissible homogenized tensors, i.e. the set of composite designs. As already seen in chapter 7, this boils down to solving the G-closure problem, i.e. to characterize completely the set $\mathcal{G}_\theta$ in terms of coupled bounds. This is inextricably linked with characterization of the micro-geometries that correspond to the optimal bounds of $\mathcal{G}_\theta$. L. Gibiansky states in his lecture notes [Gibiansky, 1993] that these microstructures are most probably the best candidates for use in structural design. Nevertheless, in general there are just few examples where the G-problem is solved explicitly (among those the G-closure of two- and three-dimensional two-phase composites with isotropic material parameters in $\mathbb{R}$).

In [Cherkaev, 2000], A. Cherkaev points out that the G-closure problem for complex conductivity is similar to the problem of coupled bounds for two conductivities with the difference that the initial equations are coupled. Furthermore, he states that the problem is very similar to the problem addressed in [Cherkaev and Gibiansky, 1992] and a derivation can most probably be made along this work.

Personal correspondence with Graeme Milton and Andrej Cherkaev (2017) confirms further that apart from improvement of aforementioned bounds, no one has obtained an explicit characterization of the G-closure of two isotropic phases α, $\beta \in \mathbb{C}$ until then - even in 2d, and to the best of the author's knowledge that has remained unchanged until now. G. Milton emphasises in the correspondence that in 2d one knows at least that the optimal geometries are those of sequential laminates, which are created by successively laminating by adding layers of the pure phases, as these solve the deeper problem of completely characterizing all possible matrix-valued conductivity functions, but in 3d far less is known. Evidently, this is an extensive topic of its own and beyond the scope of this work.

Returning to the argumentation from above, we cannot ascertain whether the essential conclusion of optimality of simple laminates can be applied to the case of interest.

Nevertheless, we henceforth assume based on the considerations above for further application that we can find a relaxed admissible design set $CD := CD_{\mathbb{C}}$ of composite designs, although an explicit characterization is unknown, and a relaxed objective functional $J^* := J^*_{\mathbb{C}}(\theta, A^*)$, which makes the relaxed problem well-posed and enables application of the direct method of Calculus of Variations. Our adapted problem formulation reads

Find $(\tilde{\theta}, \tilde{A}^*)$ such that

$$(\tilde{\theta}, \tilde{A}^*) = \underset{(\theta, A^*) \in CD}{\arg\min}\ J^*(\theta, A^*). \tag{9.2.1}$$

$$J^*(\theta, A^*) = \int_\Omega \theta(x) g_\alpha(x, u(x), \bar{u}(x)) + (1 - \theta(x)) g_\beta(x, u(x), \bar{u}(x))\,\mathrm{d}x + l \int_\Omega \theta(x)\,\mathrm{d}x, \tag{9.2.2}$$

where u is the solution of

$$\begin{cases} -\mathrm{div}(A^*(x)\nabla u(x)) = f(x) & \text{in } \Omega \\ u(x) = 0 & \text{on } \partial\Omega. \end{cases} \tag{9.2.3}$$

9.3. Gâteaux differential of the objective functional

Computation of the directional derivative is not straightforward for objective functionals, which are not only dependent on a complex variable z but also explicitly or implicitly dependent on its complex conjugate $\bar{z}$. Objective functionals of that type occur frequently mainly in the context of signal processing (see for example [Johnson and Dudgeon, 1993]).

In general, the derivative with respect to a complex-valued variable cannot be evaluated directly when the function depends on the variable's conjugate, these functions are called non-analytic functions and are not complex differentiable ([Rudin, 1986]). One possibility to overcome this problem is to define the formal partial derivatives, first introduced by W. Wirtinger in [Wirtinger, 1926] and to treat variable and complex conjugate as independent, each considered to be constant with respect to the other. A very compact and clearly arranged summary of the important aspects concerning differentials of real-valued functions having complex-valued arguments can be found in [Hunger, 2020].

On the basis of the formal partial derivatives (see §9.3.1), it is possible to derive the directional derivative of the objective functional in §9.3.2. This includes introduction of the appropriately adapted adjoint problem in order to eliminate the dependence of the derivative on the state increment.

9.3.1. Formal partial derivatives

Considering a function F with $F(x,y) = u(x,y) + \mathrm{i}v(x,y) = f(z)$ with $z = x + \mathrm{i}y$, the total differential is given as

$$\mathrm{d}F(x,y) = \frac{\partial F}{\partial x}\,\mathrm{d}x + \frac{\partial F}{\partial y}\,\mathrm{d}y \tag{9.3.1}$$

with the partial derivatives

$$\frac{\partial F}{\partial x} = \frac{\partial u}{\partial x} + \mathrm{i}\frac{\partial v}{\partial x}, \tag{9.3.2}$$

$$\frac{\partial F}{\partial y} = \frac{\partial u}{\partial y} + \mathrm{i}\frac{\partial v}{\partial y}. \tag{9.3.3}$$

Inserting the relations

$$\mathrm{d}x = \frac{1}{2}(\,\mathrm{d}z + \,\mathrm{d}\bar{z}), \tag{9.3.4}$$

$$\mathrm{d}y = \frac{1}{2\mathrm{i}}(\,\mathrm{d}z - \,\mathrm{d}\bar{z}). \tag{9.3.5}$$

we get

$$\mathrm{d}F = \frac{1}{2}\left(\frac{\partial F}{\partial x} - \mathrm{i}\frac{\partial F}{\partial y}\right)\,\mathrm{d}z + \frac{1}{2}\left(\frac{\partial F}{\partial x} + \mathrm{i}\frac{\partial F}{\partial y}\right)\,\mathrm{d}\bar{z} \tag{9.3.6}$$

By definition of the formal derivatives, also often called Wirtinger derivatives

$$\frac{\partial F}{\partial z} = \frac{1}{2}\left(\frac{\partial F}{\partial x} - \mathrm{i}\frac{\partial F}{\partial y}\right), \tag{9.3.7}$$

$$\frac{\partial F}{\partial \bar{z}} = \frac{1}{2}\left(\frac{\partial F}{\partial x} + \mathrm{i}\frac{\partial F}{\partial y}\right) \tag{9.3.8}$$

we deduce

$$\mathrm{d}F = \frac{\partial F}{\partial z}\,\mathrm{d}z + \frac{\partial F}{\partial \bar{z}}\,\mathrm{d}\bar{z}. \tag{9.3.9}$$

Besides the validity of common real-valued differentiation rules for sum, product and composition of functions a very useful property of the Wirtinger derivative is

$$\frac{\partial}{\partial z}\bar{z} = \frac{\partial}{\partial \bar{z}}z = 0, \tag{9.3.10}$$

which allows to treat $\bar{z}$ as constant when differentiating with respect to z and vice versa.

On the basis of this formal definition, one obtains for any real-valued function f with complex-valued argument z the differential $\mathrm{d}f$ as

$$\mathrm{d}f = 2\Re\left\{\frac{\partial f(z)}{\partial z}dz\right\} = 2\Re\left\{\frac{\partial f(z)}{\partial \bar{z}}d\bar{z}\right\}. \tag{9.3.11}$$

9.3.2. Derivation of the directional derivative

Initially, the objective functional and thus the corresponding directional derivative is, besides the dependence on the increments of the design variables $\delta\theta$ and δA^*, still dependent on the state increment δu and $\delta\bar{u}$. By introduction of the corresponding adjoint problem, we are able to eliminate this dependency of the directional derivative on δu respectively $\delta\bar{u}$.

This result can be achieved by using the formal Lagrange technique, as is usual done in optimal control of partial differential equations ([Tröltzsch, 2009]). The necessary optimality conditions are then derived by formally equating to zero the derivatives with respect to the optimization variables of the appropriately formulated Lagrangian in the complex case, see for example [Agrawal and Hoppe, 2017], [von Winckel et al., 2009] or [von Winckel and Borzì, 2008] for Lagrange functions with complex-valued state variables. Nevertheless, by proper definition of the adjoint problem and application of the Wirtinger calculus, determination of the Gâteaux differential of the objective functional follows the argumentation of [Allaire, 2002] in the real-valued parameter setting.

The adjoint problem is given by

$$\begin{cases} -\mathrm{div}(A^{*H}(x)\nabla p(x)) = \theta(x)\frac{\partial g_\alpha}{\partial \bar{u}}(x,u,\bar{u}) + (1-\theta(x))\frac{\partial g_\beta}{\partial \bar{u}}(x,u,\bar{u}) & \text{in } \Omega \\ p(x) = 0 & \text{on } \partial\Omega, \end{cases} \tag{9.3.12}$$

where the derivatives $\frac{\partial g_\alpha}{\partial \bar{u}}(x,u,\bar{u})$ and $\frac{\partial g_\beta}{\partial \bar{u}}(x,u,\bar{u})$ must be understood as derivatives in the sense of Wirtinger calculus, we differentiate with respect to the complex conjugate of u, treating u as constant.

We require

$$\begin{cases} \frac{\partial g_{\alpha,\beta}}{\partial \bar{u}}(x,u,\bar{u}) \text{ is } \textbf{measurable} \text{ in } x \text{ for each fixed } u,\bar{u}\in\mathbb{C} \\ \frac{\partial g_{\alpha,\beta}}{\partial \bar{u}}(x,u,\bar{u}) \text{ is } \textbf{continuous} \text{ in } u,\bar{u} \text{ for each fixed } x\in\Omega \\ |\frac{\partial g_{\alpha,\beta}}{\partial \bar{u}}(x,\bar{u})| \le k'(x) + C'|\bar{u}|^{m-1} \text{ for } 1\le m < \frac{2N}{N-2} \text{ with } k'(x)\in L^q(\Omega),\ q > \frac{2N}{N-2}, \end{cases} \tag{9.3.13}$$

which again ensures differentiability of the objective functional and that the source term of the adjoint equation (9.3.12) is in $H^{-1}(\Omega)$.

Theorem 9.3.1
The objective functional $J^*(\theta, A^*)$ is Gâteaux differentiable on the space of admissible composite designs with directional derivative

$$\delta J^*(\theta, A^*) = \int_\Omega \delta\theta(x)(g_\alpha(x, u(x), \bar{u}(x)) + l - g_\beta(x, u(x), \bar{u}(x)))\,\mathrm{d}x - 2\Re\left\{\int_\Omega \langle \delta A^*(x)\nabla u(x), \nabla p(x)\rangle\,\mathrm{d}x\right\}.$$

$\delta\theta$ and δA^* are admissible increments in CD, u solution of the state equation (9.2.3) and p is solution of the adjoint state equation (9.3.12).

Proof. We consider again the objective functional $J^*(\theta, A^*)$, which is formally still dependent on the state u and the complex conjugate of the state $\bar{u}$.

$$\begin{aligned}\delta J^*(\theta, A^*) &= \frac{\mathrm{d}}{\mathrm{d}t} J^*(\theta(t), A^*(t), u(t), \bar{u}(t))\Big|_0 = \\ &= \frac{\mathrm{d}}{\mathrm{d}t}\left[\int_\Omega \theta(t) g_\alpha(x, u(t), \bar{u}(t)) + (1-\theta(t)) g_\beta(x, u(t), \bar{u}(t))\,\mathrm{d}x + l\int_\Omega \theta(t)\,\mathrm{d}x\right]\Bigg|_0\end{aligned}$$

Applying Wirtinger calculus, we consequently receive

$$\begin{aligned}\delta J^*(\theta, A^*) = &\int_\Omega \delta\theta(x)\Big(g_\alpha(x, u(x), \bar{u}(x)) - g_\beta(x, u(x), \bar{u}(x)) + l\Big)\,\mathrm{d}x + \\ &+ 2\Re\left\{\int_\Omega \left(\theta(x)\frac{\partial g_\alpha}{\partial \bar{u}}(x, u(x), \bar{u}(x)) + (1-\theta(x))\frac{\partial g_\beta}{\partial \bar{u}}(x, u(x), \bar{u}(x))\right)\delta\bar{u}(x)\,\mathrm{d}x\right\},\end{aligned}$$

where the derivatives $\frac{\partial g_\alpha}{\partial \bar{u}}(x, u, \bar{u})$ and $\frac{\partial g_\beta}{\partial \bar{u}}(x, u, \bar{u})$ must be understood as formal Wirtinger derivatives.
It remains to show

$$\begin{aligned}2\Re\left\{\int_\Omega \left(\theta(x)\frac{\partial g_\alpha}{\partial \bar{u}}(x, u(x), \bar{u}(x)) + (1-\theta(x))\frac{\partial g_\beta}{\partial \bar{u}}(x, u(x), \bar{u}(x))\right)\delta\bar{u}(x)\,\mathrm{d}x\right\} \\ = -2\Re\left\{\int_\Omega \langle \delta A^{*H}(x)\nabla u(x), \nabla p(x)\rangle\,\mathrm{d}x\right\},\end{aligned}$$

to eliminate the state increment in the directional derivative.

Differentiating the state equation, we obtain δu as unique solution of

$$\begin{cases} -\mathrm{div}(A^*(x)\nabla\delta u(x)) &= \mathrm{div}(\delta A^*(x)\nabla u(x)) \quad \text{in } \Omega \\ \delta u(x) &= 0 \quad \text{on } \partial\Omega. \end{cases} \tag{9.3.14}$$

Multiplying equations (9.3.14) by p and integrating by parts, we get for the left hand side

$$-\int_\Omega \langle \mathrm{div}(A^*(x)\nabla\delta u(x)), p(x)\rangle \,\mathrm{d}x = \int_\Omega \langle A^*(x)\nabla\delta u(x), \nabla p(x)\rangle \,\mathrm{d}x - \int_{\partial\Omega} \langle A^*(x)\nabla\delta u(x)\cdot\nu, p(x)\rangle \,\mathrm{d}\sigma_x$$

and for the right hand side

$$\int_\Omega \langle \mathrm{div}(\delta A^*(x)\nabla u(x)), p(x)\rangle \,\mathrm{d}x = -\int_\Omega \langle \delta A^*(x)\nabla u(x), \nabla p(x)\rangle \,\mathrm{d}x + \int_{\partial\Omega} \langle \delta A^*(x)\nabla u(x)\cdot\nu\,, p(x)\rangle \,\mathrm{d}\sigma_x$$

Combination of both leads to

$$\begin{aligned} \int_\Omega \langle A^*(x)\nabla\delta u(x), \nabla p(x)\rangle \,\mathrm{d}x = &-\int_\Omega \langle \delta A^*(x)\nabla u(x), \nabla p(x)\rangle \,\mathrm{d}x \\ &+ \int_{\partial\Omega} \langle \delta A^*(x)\nabla u(x)\cdot\nu, p(x)\rangle \,\mathrm{d}\sigma_x + \int_{\partial\Omega} \langle A^*(x)\nabla\delta u(x)\cdot\nu, p(x)\rangle \,\mathrm{d}\sigma_x. \end{aligned} \tag{9.3.15}$$

Multiplying the adjoint equation (9.3.12) by δu and integrating by parts leads to

$$\begin{aligned} \int_\Omega \langle A^{*H}(x)\nabla p(x), &\nabla\delta u(x)\rangle \,\mathrm{d}x = \\ &\int_\Omega \langle \theta(x)\frac{\partial g_\alpha}{\partial\bar{u}}(x, u(x), \bar{u}(x)) + (1-\theta(x))\frac{\partial g_\beta}{\partial\bar{u}}(x, u(x), \bar{u}(x)), \delta u(x)\rangle \,\mathrm{d}x \\ &-\int_{\partial\Omega} \langle A^{*H}(x)\nabla p(x), \nabla\delta u(x)\rangle \,\mathrm{d}\sigma_x. \end{aligned} \tag{9.3.16}$$

Considering

$$\int_\Omega \langle A^{*H}(x)\nabla p(x), \nabla\delta u(x)\rangle \,\mathrm{d}x = \int_\Omega \langle \nabla p(x), A^*(x)\nabla\delta u(x)\rangle \,\mathrm{d}x = \int_\Omega \overline{\langle A^*(x)\nabla\delta u(x), \nabla p(x)\rangle} \,\mathrm{d}x,$$

combination of (9.3.15) and (9.3.16) leads to

$$\begin{aligned}\int_\Omega \langle \theta(x)\frac{\partial g_\alpha}{\partial \bar{u}}(x,u(x),\bar{u}(x)) + (1-\theta(x))\frac{\partial g_\beta}{\partial \bar{u}}(x,u(x),\bar{u}(x)), \delta u(x)\rangle \,\mathrm{d}x \\ = \int_{\partial\Omega} \langle A^{*H}(x)\nabla p(x), \nabla \delta u(x)\rangle \,\mathrm{d}\sigma_x - \int_\Omega \overline{\langle \delta A^*(x)\nabla u(x), \nabla p(x)\rangle}\,\mathrm{d}x \\ + \int_{\partial\Omega} \overline{\langle \delta A^*(x)\nabla u(x)\cdot\nu, p(x)\rangle}\,\mathrm{d}\sigma_x + \int_{\partial\Omega} \overline{\langle A^*(x)\nabla\delta u(x)\cdot\nu, p(x)\rangle}\,\mathrm{d}\sigma_x\end{aligned} \tag{9.3.17}$$

and with consideration of boundary conditions this shows

$$\begin{aligned}\int_\Omega \langle \theta(x)\frac{\partial g_\alpha}{\partial \bar{u}}(x,u(x),\bar{u}(x)) + (1-\theta(x))\frac{\partial g_\beta}{\partial \bar{u}}(x,u(x),\bar{u}(x)), \delta u(x)\rangle \,\mathrm{d}x \\ = -\int_\Omega \overline{\langle \delta A^*(x)\nabla u(x), \nabla p(x)\rangle}\,\mathrm{d}x\end{aligned}$$

leading to to

$$\begin{aligned}2\Re\left\{\int_\Omega \langle \theta(x)\frac{\partial g_\alpha}{\partial \bar{u}}(x,u(x),\bar{u}(x)) + (1-\theta(x))\frac{\partial g_\beta}{\partial \bar{u}}(x,u(x),\bar{u}(x)), \delta u(x)\rangle \,\mathrm{d}x\right\} \\ = -2\Re\left\{\int_\Omega \langle \delta A^*(x)\nabla u(x), \nabla p(x)\rangle \,\mathrm{d}x\right\},\end{aligned}$$

which completes the proof. □

9.4. Adjusted problem setting: Restriction to simple laminates

We computed the directional derivative of the relaxed objective functional assuming existence of a relaxed admissible design set and relaxed problem formulation, which transfers the problem of interest into a well-posed relaxed problem setting. Without any further information or assumption on the set $CD_{\mathbb{C}}$, an argumentation along the lines of the real-valued case such as for example derivation of necessary optimality criteria is not possible. As already stated in §9.2, the explicit characterization of the G-closure, i.e. the set of composite designs $CD_{\mathbb{C}}$, is still an unsolved problem. However, for real-valued material parameter input, the structure of this set directly contributes to the proof of the optimality of simple laminates, which forms the basis for further application of the theory. For material parameter input in $\mathbb{C}$, a conclusion along the argumentation of §7.4 is not possible

at this point.
Nevertheless, Graeme Milton pointed out in personal correspondence that at least in 2d one knows that the optimal geometries, i.e. the composite materials with effective tensors on the boundary of G_θ, are those of sequential laminates. In §7.2.2 we stated that also for real-valued material parameters Allaire derives G_θ and the optimality of simple laminates from the sequential laminates as optimal microstructures. This parallel at least gives the hint and starting point to consider simple laminates as the materials of interest even in the complex-valued material parameter case.
Assuming that corresponding results as for the real-valued parameter setting, where a rigorous mathematical derivation is possible, also apply to the complex-valued parameter setting we restrict the design set to simple rank-1 laminates.
A rank-1 laminate consisting of two isotropic materials with material parameters $\alpha, \beta \in \mathbb{C}$ in proportion θ and $1-\theta$ with lamination direction $e = (1,0)^T$ respectively $e = (1,0,0)^T$ is described by eigenvalues equal to the harmonic and arithmetic mean (see [Milton, 2002]):

$$A^*_{2d} = \begin{pmatrix} \lambda^-_\theta & 0 \\ 0 & \lambda^+_\theta \end{pmatrix}, \; A^*_{3d} = \begin{pmatrix} \lambda^-_\theta & 0 & 0 \\ 0 & \lambda^+_\theta & 0 \\ 0 & 0 & \lambda^+_\theta \end{pmatrix}$$

$$\text{with } \lambda^-_\theta = \left(\frac{\theta}{\alpha} + \frac{1-\theta}{\beta} \right)^{-1} \text{ and } \lambda^+_\theta = \theta\alpha + (1-\theta)\beta.$$

Simple laminates with lamination direction e are accordingly described by rotation angle φ and density θ respectively rotation angles φ, ψ and density θ in three dimensions.
Restriction of the design set to simple laminates and formulation of the derived directional derivative with regard to the admissible increments $\delta\theta$ and $\delta\varphi$ respectively $\delta\theta$, $\delta\varphi$ and $\delta\psi$ in three dimensions forms then the basis for application of a gradient method.
Although no rigorous mathematical justification of the restriction of the design set to simple laminates in the framework of relaxation via homogenization can be provided so far, it will turn out that this approach seems to yield very useful results – at least for the applications of interest.

9.5. Gradient method

We present the gradient method for the two-dimensional case in order to point out the differences of the gradient method with complex material parameters α and $\beta \in \mathbb{C}$ in comparison to the method of §7.6. A formulation in three dimensions with the corresponding rotation matrices $R_1(\psi)$ and $R_2(\varphi)$ as described in §8.4 then works analogously.
Based on the class of homogenized tensors

$$A^*(\theta, \varphi) = R(\varphi) \begin{pmatrix} \lambda^-_\theta & 0 \\ 0 & \lambda^+_\theta \end{pmatrix} R^{-1}(\varphi) \tag{9.5.1}$$

with rotation matrix

$$R(\varphi) = \begin{pmatrix} \cos(\varphi) & -\sin(\varphi) \\ \sin(\varphi & \cos(\varphi) \end{pmatrix}, \tag{9.5.2}$$

the gradient of the objective functional $J^*(\theta, \varphi)$ with respect to an admissible increment $(\delta\theta, \delta\varphi)$ is given by

$$\delta J^*(\theta,\varphi) = -2\Re\left\{\int_\Omega \delta\varphi(x)\left\langle \frac{\partial A^*}{\partial \varphi}(\theta(x),\varphi(x))\nabla u(x), \nabla p(x)\right\rangle \mathrm{d}x\right\} \tag{9.5.3}$$

$$-2\Re\left\{\int_\Omega \delta\theta(x)\left\langle \frac{\partial A^*}{\partial \theta}(\theta(x),\varphi(x))\nabla u(x), \nabla p(x)\right\rangle \mathrm{d}x\right\} \tag{9.5.4}$$

$$+\int_\Omega \delta\theta(x)(g_\alpha(x,u(x),\bar{u}(x)) + l - g_\beta)(x,u(x),\bar{u}(x))\,\mathrm{d}x. \tag{9.5.5}$$

A gradient method for the given minimization problem is then given by

Gradient method:

Initialization: Initialize θ_0 and φ_0 and compute A^*. For simplicity, choose constant θ_0 and constant angle φ_0.

Iteration for $k \geq 0$: until convergence

1. Compute state u_k and adjoint state p_k as solutions of the corresponding problems with the previous design parameters θ_k and φ_k.
2. Update parameters by

$$\varphi_{k+1}(x) = \varphi_k(x) + t_k \cdot 2\Re\left\{\left\langle \frac{\partial A^*}{\partial \varphi}(\theta_k(x),\varphi_k(x))\nabla u_k(x), \nabla p_k(x)\right\rangle\right\}$$

$$\theta_{k+1}(x) = \max(0, \min(1, \theta_k(x) - t_k Q_k(x)))$$

with t_k a small step such that $J^*(\theta_{k+1}, \varphi_{k+1}) < J^*(\theta_k, \varphi_k)$ and

$$\begin{aligned} Q_k(x) =& (g_\alpha(x,u(x),\bar{u}(x)) + l - g_\beta(x,u(x),\bar{u}(x))) \\ & - 2\Re\left\{\left\langle \frac{\partial A^*}{\partial \theta}(\theta_k(x),\varphi_k(x))\nabla u(x), \nabla p(x)\right\rangle\right\}. \end{aligned}$$

Derivation of the gradient method in a subdomain Ω_1 is analogous to the real-valued parameter case in §8.3.

10. Application

All application examples presented in the following are based on corresponding extensions of the implementation described in chapter 8. Details of the structure of the code and further remarks are summarized in §8.1.

We first examine the functionality of the method for complex material parameters in two simple examples for 2d and 3d application in §10.1 and §10.2. After that, we approach the application for sensor optimization further by studying the influences of different parameters on the optimization in §10.3.

The parameter describing the material properties derived in §6.2 represents for frequencies $\omega \neq 0$ a joint parameter of electric permittivity and conductivity. In this description, the influence of bound and free charge carriers can no longer be distinguished. Hence, we proceed phenomenologically and distinguish in the following two materials in terms of their ability to absorb the electric field, which is reflected in different imaginary parts of the material parameter. This approach is based on the assumption that the sensor made of material A has significantly stronger capability for absorption compared to the surrounding material B and allows qualitative studies on the influences of the beforementioned parameters on the optimization.

In all following applications, we consider the optimization problem searching for the design maximizing the energy measured at a sensor built of material A. The following choice of objective functional serves as a proxy for the energy:

$$\min_{(\theta,A^*)\in CD} J^*(\theta, A^*) = \min_{(\theta,A^*)\in CD} -\int_{\Omega_1} \theta(x)(u(x)\bar{u}(x))\,\mathrm{d}x + l\int_{\Omega_1} \theta(x)\,\mathrm{d}x$$

on a subdomain Ω_1 with u solution of

$$\begin{cases} -\mathrm{div}(A^*(x)\nabla u(x)) = F & \text{in } \Omega \\ u(x) = 0 & \text{on } \partial\Omega. \end{cases}$$

Unless otherwise stated, we choose material parameters $\alpha = 1+2\mathrm{i}$, $\beta = 1+1\mathrm{i}$ and a volume constraint of 50%, the material parameter in Ω_2 equals $\beta = 1 + 1\mathrm{i}$.

The geometric setting, source term and any special features are specified in each section separately. In each case, the optimization area Ω_1 is displayed in blue, Ω_2 in grey and the location of the source in red.

Since we limit ourselves to qualitative comparisons, no units are given below.

When we refer to an "optimal design" in the following, we always refer to the improved design after the application of the optimization routine. As already mentioned, the method provides an improvement of the objective functional value, but it is not guaranteed that the result also corresponds to a global optimum of the optimization problem.

10.1. Point source application in 2d

The problem definition for the application problem with point source in 2d is already based on the idea of sensor optimization. For a given point source with strength of 1 in the point $(0.4, 0.25)^T$ in Ω, we want to place a sensor made material A in the given subdomain Ω_1 in a way, that we capture the maximum energy in the sensor. Figure 10.1 specifies the geometrical arrangement.

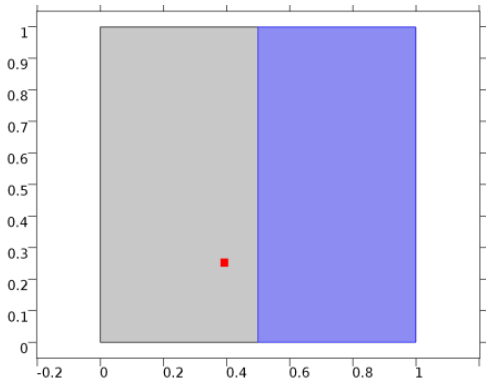

Figure 10.1.: Domain Ω consisting of $\Omega_1 = (0.5, 1) \times (0, 1)$ (blue) and $\Omega_2 = (0, 0.5) \times (0, 1)$ (grey) with point $(0.4, 0.25)^T$ (red).

Simulations are performed on a triangular mesh with quadratic Lagrange Elements resulting in 3289 DOF. We initialize with constant density $\theta = 0.5$ and constant lamination direction $e = (1, 0)^T$ in Ω_1. Figure 10.2 describes the progress of the gradient method for the described optimization problem.

As a result of the optimization it is expected that the sensor will form as close as possible to the source and that the position of the source will influence the optimal design.

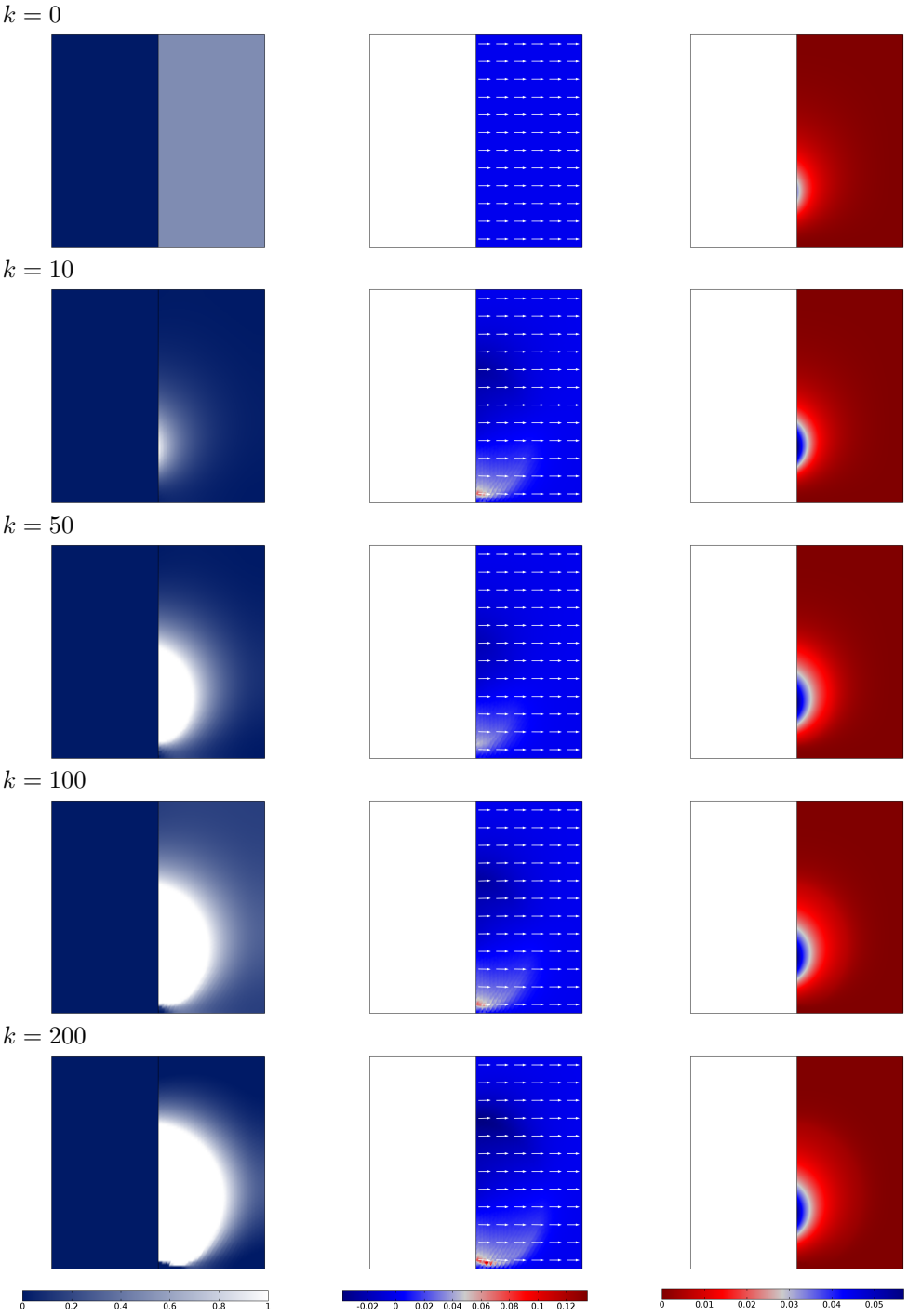

Figure 10.2.: Gradient Method for complex-valued parameter setting: volume fraction θ (left), lamination direction e respectively rotation angle φ (middle) and integrand of objective functional value $\theta(x,y)(u(x,y)\bar{u}(x,y))$ (right) for iteration steps $k = 0$, $k = 10$, $k = 50$, $k = 100$ and $k = 200$.

To check the functionality of the gradient method for complex-valued material parameters, the first 200 optimization steps were conducted analogous to the test cases for the real-valued parameters. In the course of these 200 steps, a clear formation of a 0-1 design is observed in the density plots (see figure 10.2 left), which, however, in this case is not yet finished at step 200. Considering the lamination direction shown as white arrows in the plots in the middle of Figure 10.2, no major development can be seen in these 200 steps. In addition to the arrow plot, we therefore included the rotation angle in the plots as surface plot. It can be seen that the change of the rotation angle in displayed steps starting with 0 degrees for $k = 0$ extends only over a range from $-2.15°$ to $7.73°$. In the right column of Figure 10.2, the development of the integrand of the objective functional value $\theta(x, y)(u(x, y)\bar{u}(x, y))$ throughout the 200 optimization steps is displayed. You can see that at the beginning of the optimization the objective functional changes significantly, whereas the improvement of the objective functional in the last 100 steps is not clearly visible. This behaviour is also apparent in the objective functional value plot (see figure 10.3). Significant improvement of the objective functional takes place within the first 100 steps.

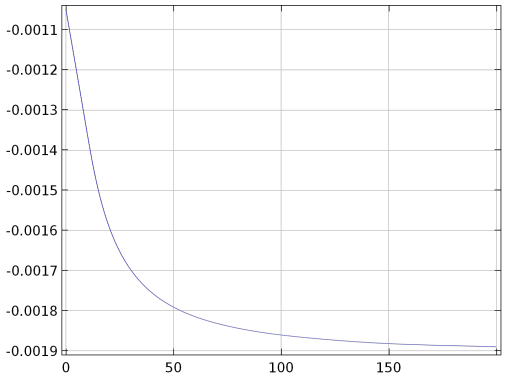

Figure 10.3.: Objective functional for point source application in 2d.

Despite the fact that only 200 steps have been performed, the implemented method shows the correct mode of operation of the algorithm in the complex-valued material parameter setting. As expected, the material in which the energy is measured, is positioned in a semicircle closest possible to the source and the choice of position of the point source is reflected in the optimization.

Especially in the two left columns of figure 10.2, a clear influence of the zero boundary condition on the optimization can be seen. This is an aspect of optimization that needs to be examined in more detail, at this point we refer to §10.3.3.

On the basis of the presented functional test in 2d, we conduct further plausibility tests in 3d.

10.2. Dipole application in 3d

In Part I of this work we address in particular the highly directional nature of the described EME source. In order to approach an application of the optimization method for sensor optimization in this context, we consider point dipole sources in a 3d geometry. To investigate the effect of the directed source on the optimization, we consider two different cases. These differ only in the direction of the dipole moments of the sources, which is expected to have a significant influence on the behaviour of the optimization method.
We consider the optimization problem searching for the design maximising the energy measured at a sensor built of material A. The source term F is described by an electrostatic point dipole in the point $p = (0.25, 0.5, 0.5)^T$. Figure 10.4 displays the geometry. We consider two cases for the direction of the electric dipole moment: $n_p = (0, 1, 0)^T$ and $n_p = (1, 1, 1)^T$, the magnitude of the electric dipole moment is in both cases 1000.

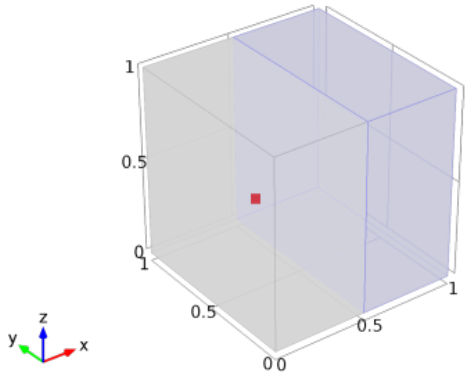

Figure 10.4.: Domain Ω consisting of $\Omega_1 = (0.5, 1) \times (0, 1) \times (0, 1)$ (blue) and $\Omega_2 = (0, 0.5) \times (0, 1) \times (0, 1)$ (grey) with Point $(0.25, 0.5, 0.5)^T$ (red).

Simulations are performed on a triangular mesh with quadratic Lagrange Elements resulting in 31044 DOF. When using a dipole source, the mesh in the vicinity of the source must be generated accordingly fine, which explains the higher number of degrees of freedom in comparison to the mesh applied in §8.4.2. We initialize with constant density $\theta = 0.5$ and constant lamination direction $e = (1, 0, 0)^T$ in Ω_1.
Especially in the comparison of the two considered optimization scenarios, one expects to see the influence of the directed source on the optimization. For the source with dipole moment $n_p = (0, 1, 0)^T$ an optimal design symmetrical to the xz-cut-plane for $y = 0.5$ is expected. Accordingly we expect an asymmetrical design that reflects the directional character of the source for the optimization with dipole moment $n_p = (1, 1, 1)^T$.

We first consider the case for $n_p = (0, 1, 0)^T$. A total of eight steps of the algorithm are

performed until no further improvement of the objective functional can be achieved by the implemented method. After step 8, no step size t_k can be found for which an improvement respecting the volume restriction is achieved. This can have several reasons. In the best possible case, the approximate global optimum is found by the achieved design, which is most likely the case here, as the obtained design looks exactly as theoretically expected. However, it is also possible that only a local minimum was found and the algorithm is stuck in this minimum. In any case, the optimization procedure has led to an improvement of the objective functional and furthermore, what is not to be expected, a nearly 0-1 design was created in only eight steps of the algorithm.
Figure 10.5 displays initialization of the method ($k = 0$, first row) and solution of the optimization routine for $k = 8$ (second row). As before, we show the density plots in the left column using plots in corresponding cut-planes. For a clearer presentation, we switch to isosurface-plots for the integrand of the objective functional, where points with the same distinct values of $\theta(x, y, z)u(x, y, z)\bar{u}(x, y, z)$ are combined to surfaces.

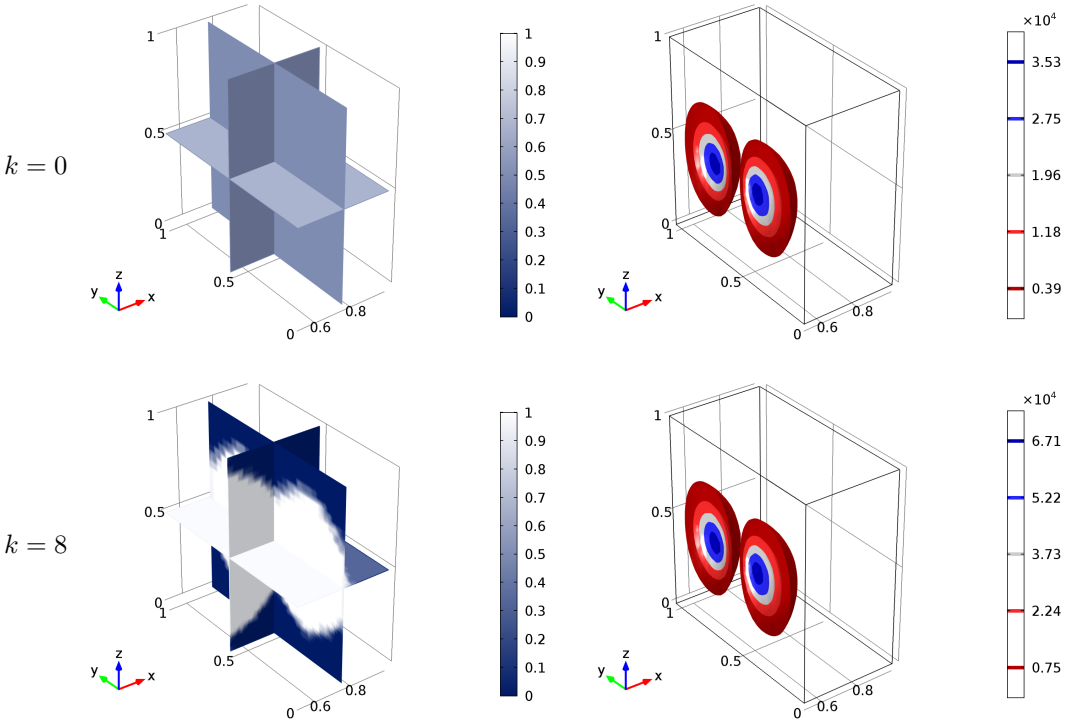

Figure 10.5.: Initialization ($k = 0$) and solution ($k = 8$) of the gradient method for $n_p = (0, 1, 0)^T$: $\theta(x, y, z)$ (left) and $\theta(x, y, z)u(x, y, z)\bar{u}(x, y, z)$ (right).

The plots in the left column show that after step 8, a 0-1 design has been created. The plots in the right column confirm that the objective functional increases significantly. As one would expect from symmetry of the dipole source, a symmetrical design emerges.

Figure 10.6 shows the corresponding values for $k = 8$ in different cut planes for $x = 0.75$, $y = 0.5$ and $z = 0.5$. You can clearly see the symmetry of the optimal design and also that there are only few areas of intermediate densities. Especially in these 2d plots, artefacts from the used mesh become apparent. We use a mesh for which several hundred steps of the optimization routine can be performed without excessive computational cost. For a further optimization it would be conceivable to use the achieved solution as a starting point for a further run of the optimization on finer mesh.
We now consider the case for $n_p = (1, 1, 1)^T$, where we expect a significant change in the optimal design compared to the first considered case due to the changed direction of the electric dipole moment. Also, in this case, the algorithm needs (with a total of 9 steps) comparatively few steps to generate an approximate 0-1-design (see figure 10.7). The asymmetrical character of the resulting design is clearly visible in the slice plots in figure 10.8. The clear development of this asymmetric design, which follows the dipole properties, confirms that the algorithm also works correctly in the 3d case as this again resembles the theoretically expected design.

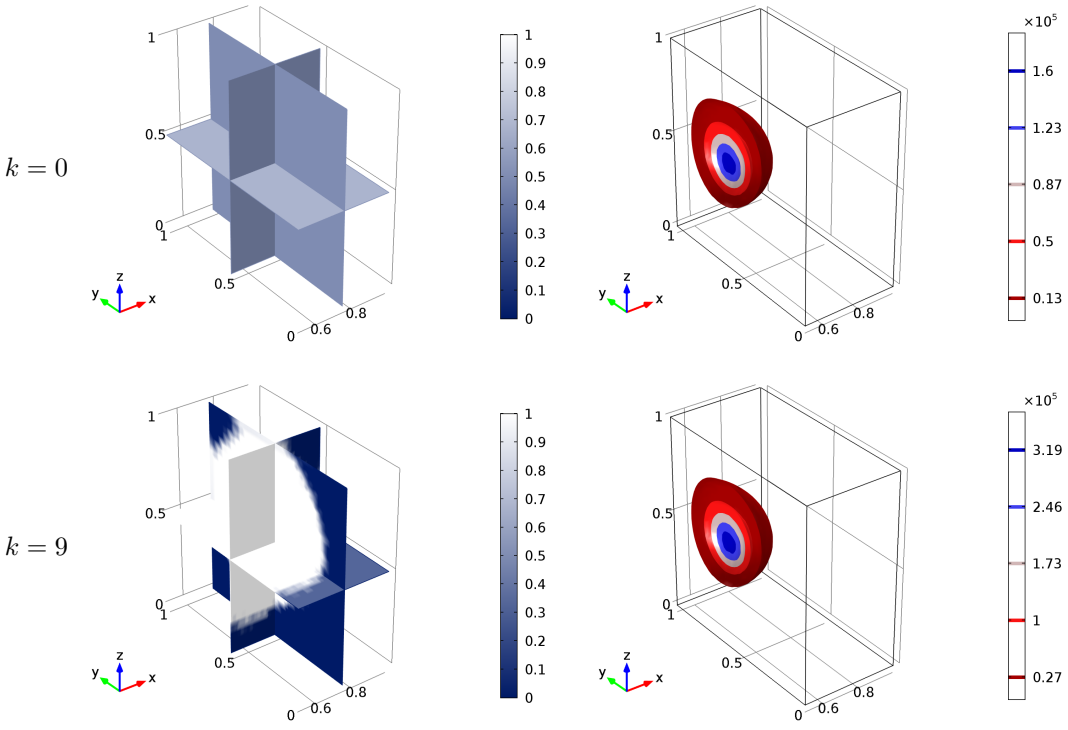

Figure 10.7.: Initialization ($k = 0$) and solution ($k = 9$) of the gradient method for $n_p = (1, 1, 1)^T$: $\theta(x, y, z)$ (left) and $\theta(x, y, z)u(x, y, z)\bar{u}(x, y, z)$ (right).

It is noticeable that, in comparison to the previous applications, only a few steps are conducted to generate the optimal design. This is most probably due to the applied source

$x = 0.75$

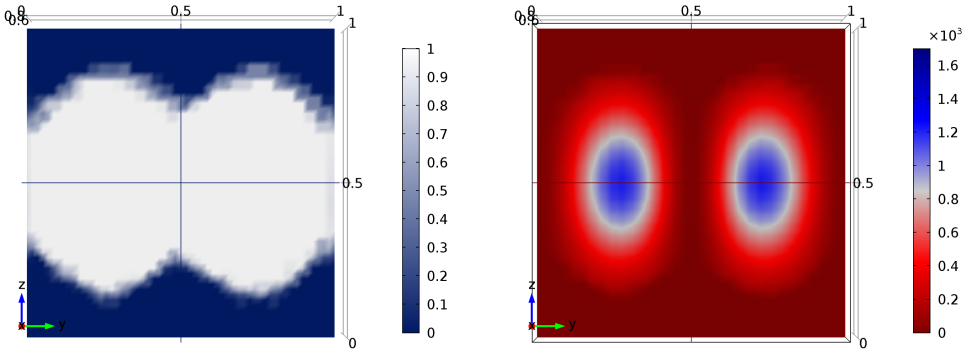

$y = 0.5$

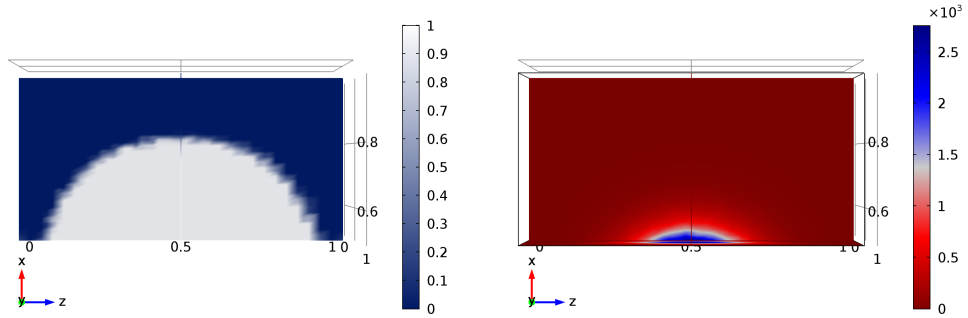

$z = 0.5$

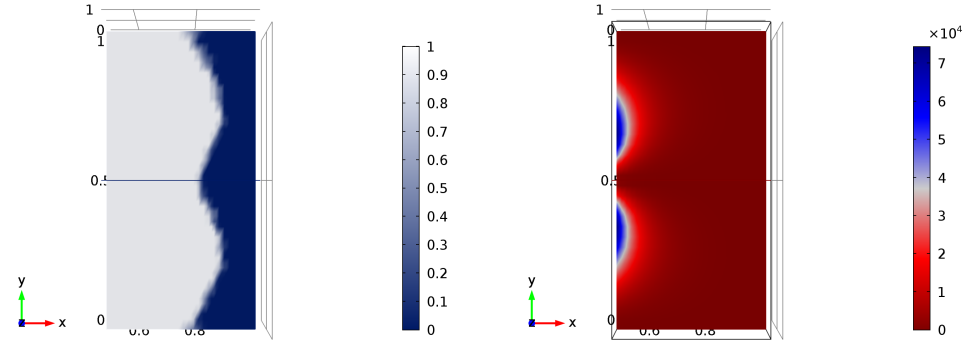

Figure 10.6.: Solution of the gradient method for $n_p = (0, 1, 0)^T$ in cut planes $x = 0.75$, $y = 0.5$ and $z = 0.5$: $\theta(x, y, z)$ (left) and $\theta(x, y, z)u(x, y, z)\bar{u}(x, y, z)$ (right).

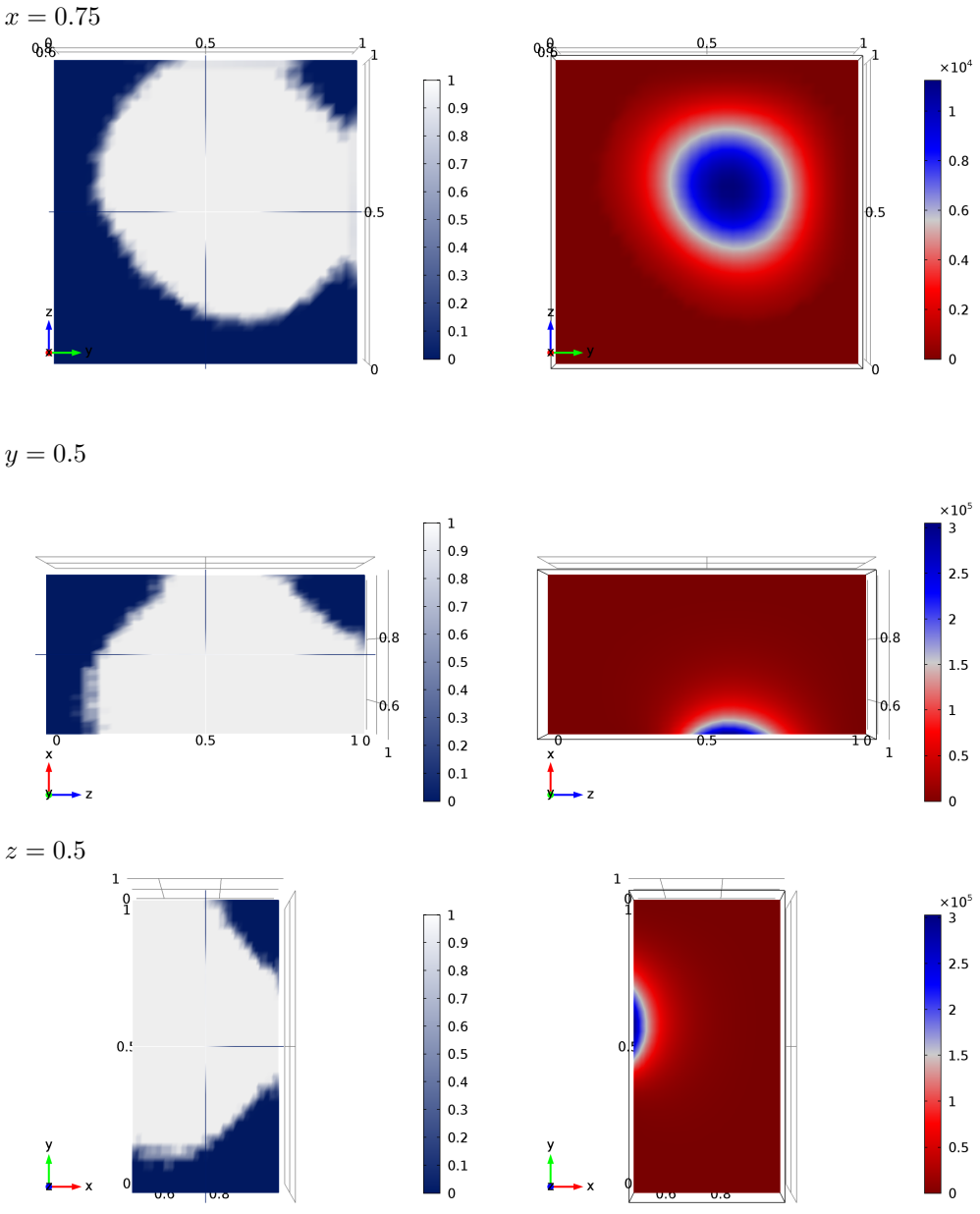

Figure 10.8.: Solution of the gradient method for $n_p = (1, 1, 1)^T$ in cut planes $x = 0.75$, $y = 0.5$ and $z = 0.5$: $\theta(x, y, z)$ (left) and $\theta(x, y, z)u(x, y, z)\bar{u}(x, y, z)$ (right).

strength, §10.3.1 examines this influence in detail.

10.3. Investigation of the influence of selected parameters on the optimization

In the following we study the influences of different parameters on the optimization. In addition to the investigation of the the influence of the source strength on the optimization process in §10.3.1 and the functionality of the method for areas with obstacles in §10.3.2, we consider questions that arise in direct connection with the experimental setup described in Part I of this work. In particular, we investigate whether and how a grounded obstacle in close vicinity to the source influences the optimal sensor shape and position (see §10.3.2) and the impact of boundary conditions on the optimal sensor design (§10.3.3).

10.3.1. Influence of source strength

Within the scope of the simulations it was noticed that depending on the source strength, the optimization comes to a result after a significantly different number of iteration steps. The following example illustrates this very clearly. For the displayed geometry in figure 10.9 we consider three scenarios with point sources of different strength 1, 1000 respectively 1000000. For the direct comparison all simulations were conducted with the same triangular mesh resulting in 3281 DOF.

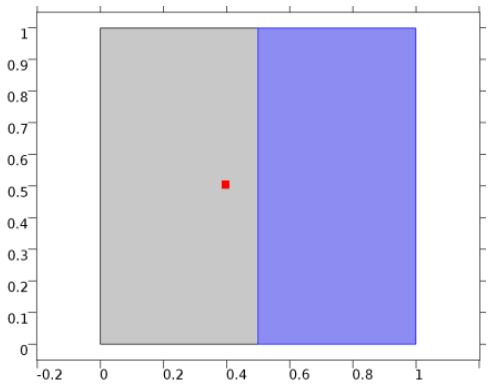

Figure 10.9.: Geometric arrangement for optimization with different source strength.

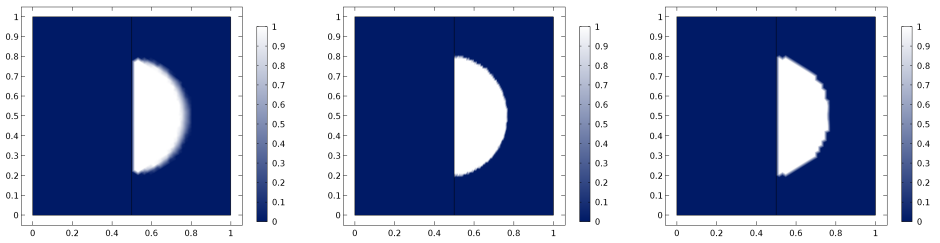

Figure 10.10.: Optimization with point source. Result of optimization with point source of 1 after 200 iteration steps (left), point source of 1000 after 29 iteration steps (middle) and point source of 1000000 after 7 iteration steps (right)

Figure 10.10 displays the result of the optimization. For the first simulation with source strength 1 (simulation A) the optimization process is terminated after 200 steps. A design with only a few areas of intermediate densities has emerged. The second simulation with point source of 1000 (simulation B) only needs 29 iteration steps to create a final 0-1 design, for simulation with point source of 1000000 (simulation C) 7 iteration steps are conducted. After that, no further improvement of the objective functional can be achieved by the implemented method.
Although the derived optimal design for simulations A and B look much smoother, while simulation C shows noticeable mesh artefacts, it can be seen clearly in all simulations what the optimal design should look like, namely a semicircle that forms near the source. Simulation C needs comparatively few iteration steps, but to achieve a similarly smooth result as in Simulation A or B it is expected that a much finer mesh is required, which in turn results in increased computational effort.
The example shows impressively that a simulation with extreme scenarios can be helpful for deduction of a first idea regarding the optimal design. The procedure is suitable here because an influence of boundary conditions on the optimization result can be excluded by the position of the source and by the imposed volume restriction of phase A. In this way, an approach with optimization in an extreme scenario, i.e. for example with high source strength, can be used as starting point for an optimization in the actual scenario. An application for optimization of 3d structures would be conceivable, where such an approach can drastically reduce the computation time, always provided that previously mentioned influences can be excluded.

10.3.2. Influence of obstacles

In the following, we investigate the influence of an obstacle in the optimization area on the optimization result, the geometry is displayed in figure 10.11. The source term F is described by an electric potential of 1 in $p = (0.4, 0.25)^T$.
The investigation of the influence of obstacles on the optimization is interesting for two reasons. On the one hand, we are interested in whether the method produces useful results even in more complicated geometric initial situations. On the other hand, based on the

experimental setup described in Part I of the work, we are interested in whether grounded components in the vicinity of source and sensor (such as for example the AE sensor in the experiments) have an influence on the optimal sensor design.

Consequently we consider two cases:

- For obstacles of material B we compare the result of the optimization for different volume fractions of 25%, 10% and 5% of material A.

- We investigate the influence of a grounded obstacle on the optimization with volume fraction of 25% of phase A.

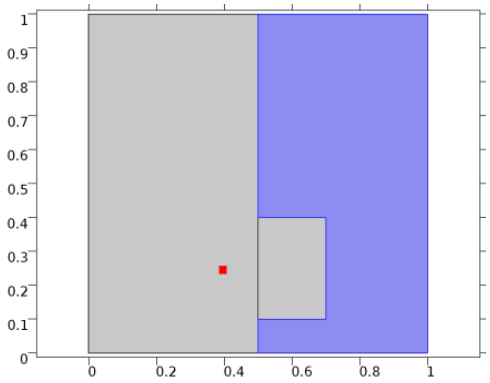

Figure 10.11.: Geometric arrangement for optimization with obstacle. Point source applied in $(0.4, 0.25)^T$ (red), subdomain Ω_1 for optimization in blue.

Simulations are performed on a triangular mesh with quadratic Lagrange Elements resulting in 3312 DOF. We initialize with constant lamination direction $e = (1, 0)^T$ in Ω_1 and and constant volume fraction corresponding to the values specified in the following.

Obstacles of material B

The special form of the optimization domain Ω_1 with an obstacle of material B prevents the optimal sensor from forming where it would form according to the example in §10.1. The application examines whether the method also achieves a meaningful result for more complicated initial situations.

We perform 200 steps of the gradient method each for the specification of 25%, 10% and 5% of material A. Figure 10.12 displays the result of the optimization routine.

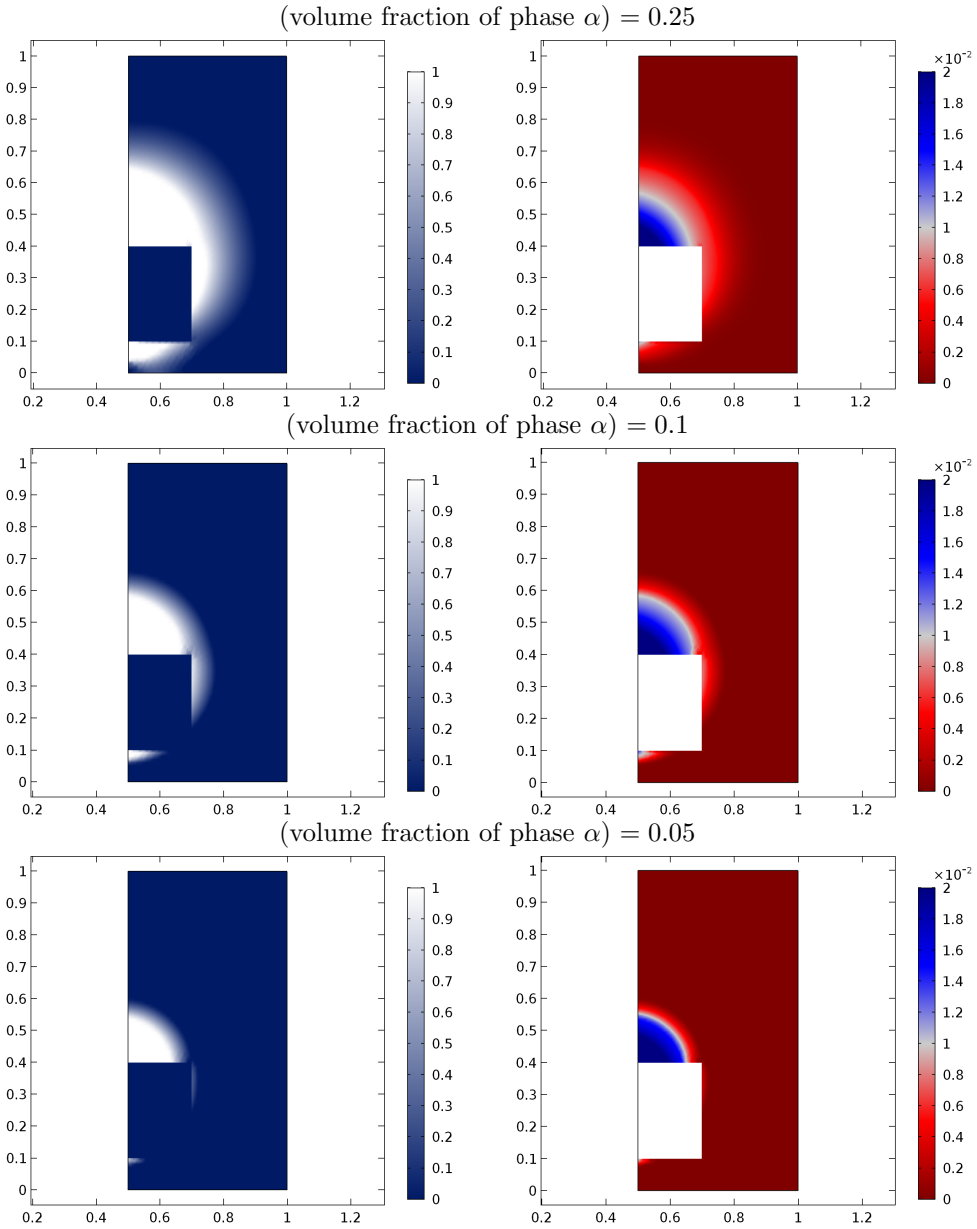

Figure 10.12.: Optimization with point source and obstacle with different volume fraction: $\theta(x, y, z)$ (left) and $\theta(x, y, z)u(x, y, z)\bar{u}(x, y, z)$ (right).

The simulations confirm once again that the method works and the optimal design is formed as expected. The sensor is established around the obstacle. After 200 steps almost a 0-1-design has been created with few areas of intermediate densities for all investigated cases. There are clear differences in the optimal design depending on the volume fraction of material A, the less material is provided, the smaller the sensor is designed which is seen

from comparison of the density plots in figure 10.12 left.

Grounded obstacle

In the following we investigate the influence of a grounded obstacle near the source on the optimization. Therefore, all boundaries of the obstacle are grounded (see figure 10.13).

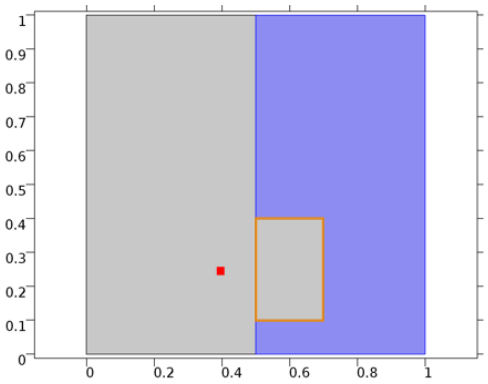

Figure 10.13.: Arrangement for optimization: grounded boundaries of the obstacle in orange.

We examine the setting with two different source strengths, namely with source strength of 1 and 1000. Figures 10.14 and 10.15 show the result of the optimization for source strength 1 and 1000 after 200 iteration steps of the optimization for a volume fraction of 25% of phase A.

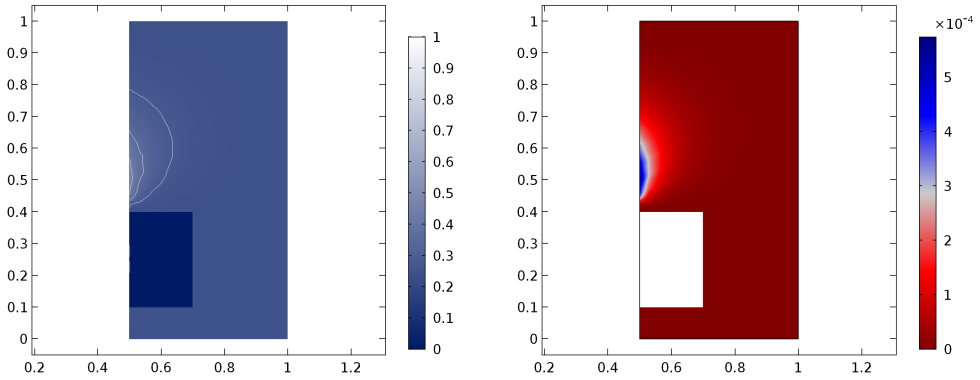

Figure 10.14.: Optimization with point source of 1 and grounded obstacle: $\theta(x, y, z)$ (left) and $\theta(x, y, z)u(x, y, z)\bar{u}(x, y, z)$ (right).

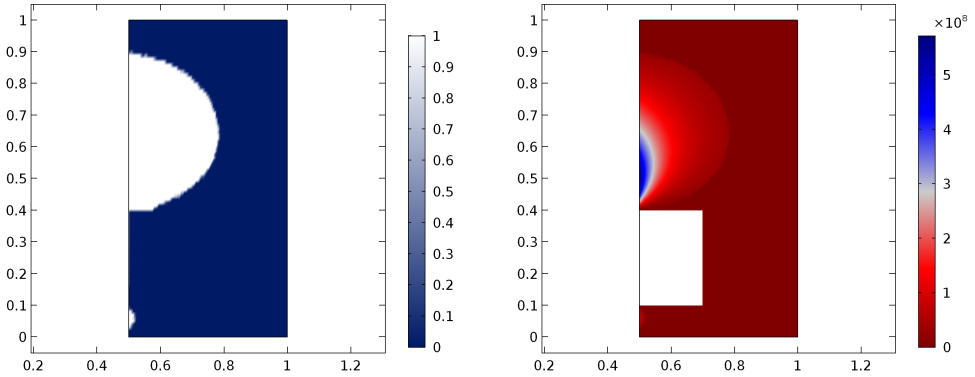

Figure 10.15.: Optimization with point source of 1000 and grounded obstacle: $\theta(x, y, z)$ (left) and $\theta(x, y, z)u(x, y, z)\bar{u}(x, y, z)$ (right).

First of all, it is noticeable that the optimization is for source strength 1 progresses considerably slower than in the cases considered so far. After 200 iteration steps, there are still only areas of intermediate densities visible in Ω_1. Nevertheless, it is felt that the optimal design to be striven for can already be guessed, for better representation isolines for $\theta = 0.28$, 0.36 and 0.44 are included in the plot (see figure 10.14). From this figure it would be concluded that the sensor forms as a semicircle above the grounded obstacle.

In comparison with the clearly developed optimal sensor design in the optimization with source strength 1000, it becomes clear that this first assumption is not entirely correct in case of doubt. In this second simulation, in addition to the described large sensor component, a small component is also formed below the grounded obstacle (see figure 10.15). There are two possible explanations for this difference in the deduced results: one possibility is that the formation of the second sensor part is not yet visible after 200 steps in the simulation with source strength 1. But it is also possible that the changed source strength in combination with the boundary conditions actually changes the optimization scenario in such a way that the optimal design looks different. This emphasizes that the correct interaction between geometric setting, source strength and boundary conditions must be ensured in order to describe an optimization problem that reflects reality. In §10.3.3 we therefore examine the influence of boundary conditions on the optimization in more detail.

In both simulations it is clear that by enclosing the grounded obstacle in the problem, the complete setting changes and the sensor is created in a completely different position compared to the simulations with non-grounded obstacles of material B. This confirms, that grounded components in too close proximity to source and sensor have significant influence on the setting and the optimal position of the sensor.

10.3.3. Influence of boundary condition

In the last application, we are interested in the influence of the boundary conditions on the optimization process. More specifically, we investigate the influence and interaction of source position and zero boundary condition in the optimization process. In this context, we also examine the possibility of coupling the optimization routine with the use of infinite element domains in surrounding domains that are not subject of optimization (see §4.2 for details on infinite element domains). This coupling enables reduction of the model to essential components in order to increase model efficiency.
An application for the previously used square geometry is possible but requires further adjustments, especially the corners of the geometry can cause numerical problems for the infinite element domain, consequently we adapt the geometry accordingly.
To cause influence of the boundary condition on the optimization intentionally we use the corresponding setting from §10.3.1 with strong point source of 1000000. In addition to different geometric settings, in the following referred to as setting A-D, we investigate the difference between different parameters for material B, i.e. $\beta = 1$ and $\beta = 1 + 1\mathrm{i}$, the material parameter of A remains $\alpha = 1 + 2\mathrm{i}$.

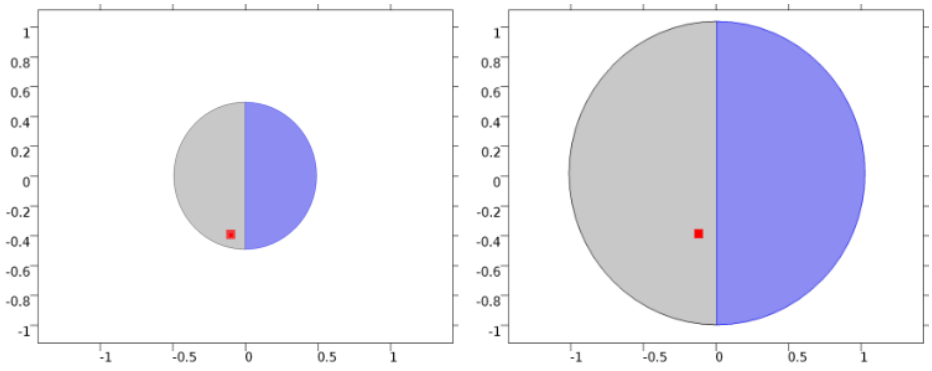

Figure 10.16.: Geometries A (left) and B (right).

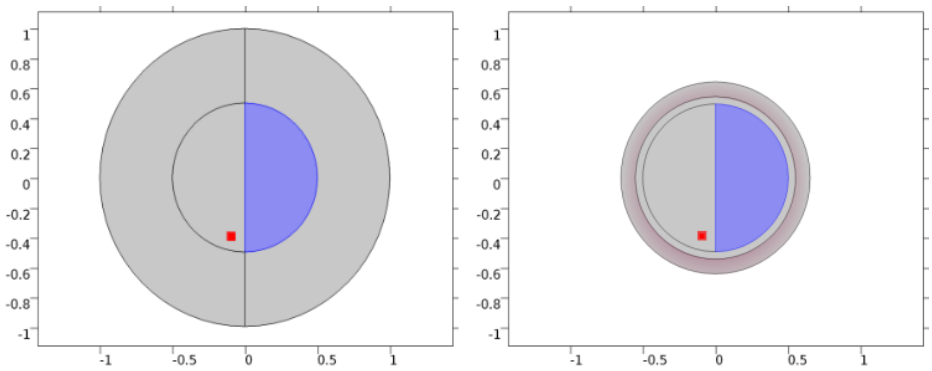

Figure 10.17.: Geometries C (left) and D (right).

Figures 10.16 and 10.17 display the geometries of the conducted simulations A-D.

The simulation with geometry A (see figure 10.16 left), in which the source is located close to the boundary in order to generate influence of the boundary condition on the sensor design, is the starting point for comparison. Altogether, we consider four different geometric arrangements, in which the same amount of sensor material is available, corresponding to a volume fraction of 50% in simulation A.

In the simulations with geometry B, in which the radius of the circle geometry is doubled and the optimization area Ω_1 increased accordingly, we expect the sensor (of the same volume as in Simulation A) to be designed according to the example from §10.3.1 as semicircle without influence of the boundary conditions.

In order to examine the coupling of the optimization with infinite element domains, the geometry must be adjusted further. Following COMSOL® in [Com, 2015b], when using the infinite element domain, there should be no change of material parameters at the boundary adjoining the infinite element domain. For this reason, we introduce a material buffer zone in which no optimization takes place.

In simulation C, see figure 10.17 left, we therefore consider the same source–boundary configuration as in simulation B, whereas in this application we only allow optimization in the inner semicircle according to simulation A.

Finally, in Simulation D we investigate the compatibility of the infinite element domain with the optimization routine. For this purpose the infinite element domain is assigned in an additional outer ring (indicated by the red shading in figure 10.17, right). The geometry in the inner circle, i.e. radius of the circle and position of the source, corresponds to the geometry in the inner circle of geometry C.

For all simulations we apply a triangular mesh, resulting in about 2900 to 3100 degrees of freedom depending on the geometry.

It has to be noted that – in order to make the presentation of the optimization results clearer – we use differently scaled illustrations in the following.

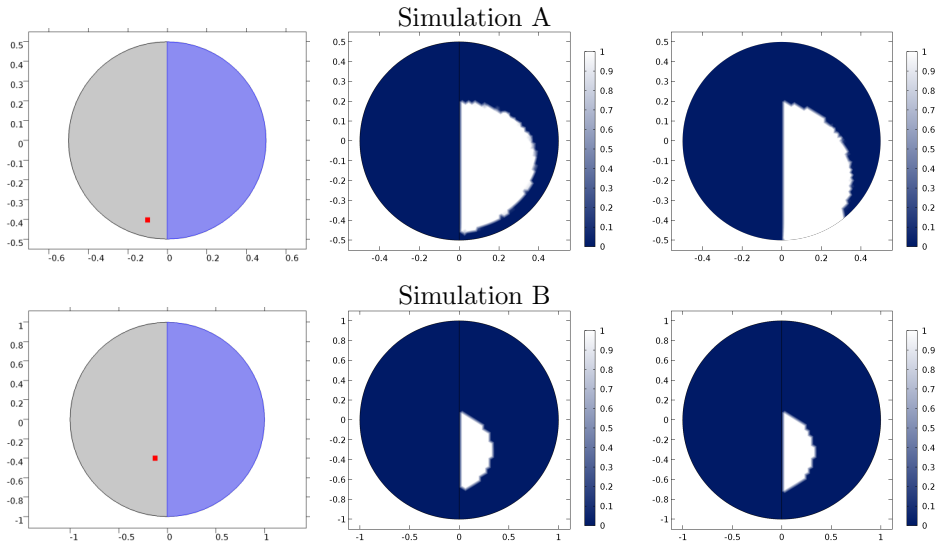

Figure 10.18.: Scenarios A and B for optimization. Geometry (left), Optimization result with $\alpha = 1 + 2\mathrm{i}$, $\beta = 1$ (middle) and Optimization result for $\alpha = 1 + 2\mathrm{i}$, $\beta = 1 + 1\mathrm{i}$ (right).

The results from simulations A and B show exactly the expected behaviour. For simulation A, where the source is located so close to the edge that the influence of the zero boundary condition is enforced, one can see that the shape of the sensor is influenced (see figure 10.18, simulation A). If, using the same volume of phase A, the source is correspondingly far located from the edge, the sensor forms a semicircle as expected (simulation B). It can be seen in both simulations, although much better in simulation A, that the choice of the material parameter of material B clearly influences the result of the optimization. Obviously, the choice of a material with no absorbing properties, i.e. $\beta_i = 0$, influences the optimization in that a distinct buffer zone of material B is built in between sensor and boundary in contrast to the simulation with material parameter $\beta = 1 + 1\mathrm{i}$.

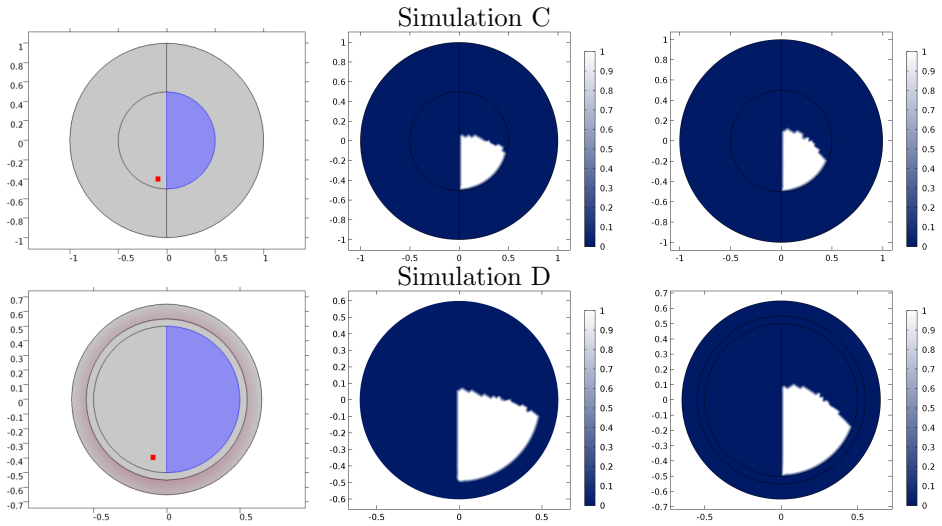

Figure 10.19.: Scenarios C and D for optimization. Geometry (left), Optimization result with $\alpha = 1 + 2i$, $\beta = 1$ (middle) and Optimization result for $\alpha = 1 + 2i$, $\beta = 1 + 1i$ (right).

Intuitively, one initially expects that the optimization in setting C results in a sensor design that corresponds to a truncated sensor geometry from simulation B. However, since the solution of the adjoint problem, which in turn depends on the objective functional defined only on Ω_1, also has an influence on the optimization, the optimal design reflects this input (see figure 10.19). There are also again slight differences in the optimal design depending on the choice of the parameter β.

Comparing both simulations C and D, the extension using infinite element domains is obviously successful. Figure 10.20 additionally highlights the regions, in which the derived optimal designs of simulation C and D differ. For both choices of material parameters $\beta = 1$ and $\beta = 1 + 1\mathrm{i}$, the sensors for simulation C and D essentially correspond except for the edge of the boundary between both phases where mesh artefacts are visible.

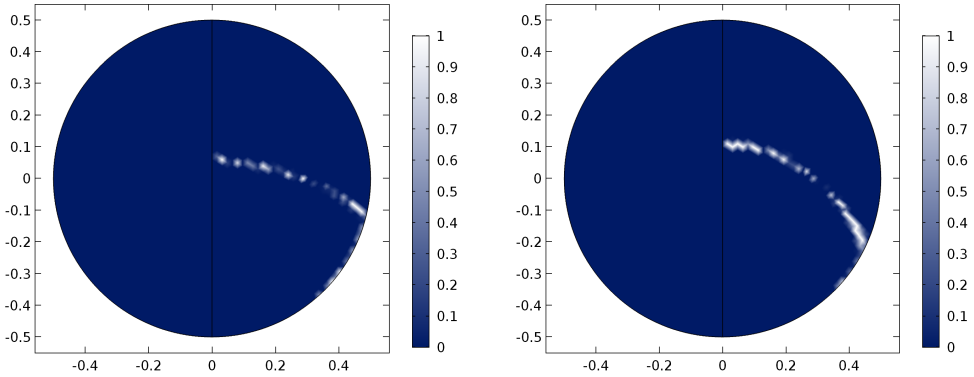

Figure 10.20.: Comparison of optimal design in Simulation C and D: $|\theta_C(x) - \theta_D(x)|$ for $\alpha = 1 + 2i$, $\beta = 1$ (left) and $\alpha = 1 + 2i$, $\beta = 1 + 1i$ (right).

The results demonstrate that it can be purposeful to couple the optimization method with infinite element domains in order to restrict the model to those parts of the geometry that contain the necessary details. Such a procedure can significantly reduce the complexity of the model and thus the computational effort.

11. Summary and outlook

The question of optimal shape and position of the EME sensor in the conducted experiments and further questions directly related to the sensor design were the motivation for the second part of the work. A formulation of the optimal design problem as a two-phase optimization problem showed that an extension of the well-known theory of shape optimization via homogenization to complex-valued parameter input is required. Despite the described difficulties to establish a closed chain of argumentation like in the real-valued parameter setting, we were able to formulate an algorithm that generates an improved design on the basis of simple rank-1 laminates as materials of interest. The application examples in chapter 10 show clearly that this derived optimization method for the complex-valued parameter setting works. Besides functionality tests, we addressed several questions related to the sensor design in the described experimental setup. Among these, we investigated the influence of grounded components such as AE sensors on the result of the optimization and the possibility of combining the optimization with the use of infinite element domains in oder to reduce the model complexity.

In principle, the deduced method does not guarantee that the optimization results in a 0-1 design, even though this was the case for most of the presented example problems. Furthermore, although the method generally leads to an improvement of the objective functional, this does not mean that a global optimum is reached, in particular since the optimality of simple laminates is not ensured in the complex-valued parameter setting.

The applications show that exact adjustment of parameters, geometry, source strength and boundary conditions to the physical conditions is extremely important. The interaction of source strength, geometry and boundary conditions must be carefully considered because this may influence the optimization result. The applications show further that the optimization can be accelerated considerably where appropriate by using sources with high source strength. Such simulations are especially suitable to get a first impression for an optimal design or to use them as a starting value for further optimization.

In summary, it can be stated that the derived and implemented method is well suited for conducting qualitative studies in order to investigate working hypotheses.

Finally, the following further interesting aspects and questions arise in this context, but go beyond the scope of this work should be mentioned. In the described qualitative studies, the proxy for energy measured in the sensor was chosen as objective functional. However, practical experience shows that, depending on the experimental setup, a full-material version of a sensor is undesirable but for example thin but long structures or half-shells would be preferable instead. From an experimental point of view, it would be rewarding to take

this fact into account in the objective functional, for example by means of penalty mechanisms. Based on the findings described in Part I of the work on the strong directional character of the source, one could also think of a sensor system in the experiment which, if necessary in supported by results of AE analysis, allows conclusions about the position of crack surfaces in the material. It might be purposeful to use optimized sensor arrays to measure the signals from different directions and thus, in combination with the findings from Part 1, draw conclusions about the position of fracture surfaces in the material. Here, too, further adjustment of the objective functional would be required in order to derive optimal shape and position of the sensor array.

Bibliography

[Com, 2015a] (2015a). COMSOL Multiphysics®. v. 5.2, www.comsol.com. COMSOL AB, Stockholm, Sweden.

[Com, 2015b] (2015b). COMSOL Multiphysics® Reference Manual. v. 5.2, www.comsol.com. COMSOL AB, Stockholm, Sweden.

[Agrawal and Hoppe, 2017] Agrawal, A. and Hoppe, H. W. (2017). Optimization of plane wave directions in plane wave discontinous Galerkin methods for the Helmholtz equation. *Portugaliae Mathematica*, 74:69–89.

[Allaire, 2002] Allaire, G. (2002). *Shape Optimization by the Homogenization Method*. Springer-Verlag New York, Inc.

[Allaire and Castro, 2001] Allaire, G. and Castro, C. (2001). A new approach for the optimal distribution of assemblies in a nuclear reactor. *Numerische Mathematik*, 89:1–29.

[Alt, 2012] Alt, H. W. (2012). *Lineare Funktionalanalysis*. Springer-Verlag, Berlin Heidelberg.

[Bartelmann et al., 2018] Bartelmann, M., Feuerbacher, B., Krüger, T., Lüst, D., Rebhan, A., and Wipf, A. (2018). *Theoretische Physik 2 Elektrodynamik*. Springer Spectrum, Berlin.

[Bendsœ, 1995] Bendsœ, M. P. (1995). *Optimization of Structural Topology, Shape and Material*. Springer, Berlin Heidelberg.

[Bergman, 1982] Bergman, D. J. (1982). Rigorous bounds for the complex dielectric constant of a two-component composite. *Annals of Physics*, 138:78–114.

[Cherkaev, 2000] Cherkaev, A. (2000). *Variational Methods for Structural Optimization*. Springer, Berlin-Heidelberg.

[Cherkaev and Gibiansky, 1992] Cherkaev, A. and Gibiansky, L. V. (1992). The exact coupled bounds for effective tensors of electrical and magnetic properties of two-component two-dimensional composites. *Proceedings of the Royal Society of Edinburgh Section A: Mathematics*, 122(1-2):93–125.

[Cherkaev and Kohn, 1997] Cherkaev, A. V. and Kohn, R. V., editors (1997). *Topics in the mathematical modelling of composite materials*. Progress in Nonlinear Differential Equations and their Applications, Volume 31, Birkhäuser, Boston.

[Cioranescu and Donato, 1999] Cioranescu, D. and Donato, P. (1999). *An Introduction to Homogenization*. Oxford lecture series in mathematics and its applications. Oxford University Press.

[Craig, 1986] Craig, J. (1986). *Introduction to robotics mechanics and control*. Addison-Wesley publishing company.

[Deaton and Grandhi, 2014] Deaton, J. D. and Grandhi, R. V. (2014). A survey of structural and multidisciplinary continuum topology optimization: post 2000. *Structural and Multidisciplinary Optimization*, 49:1–38.

[Eck et al., 2011] Eck, C., Garcke, H., and Knabner, P. (2007, 2011). *Mathematische Modellierung, 2., überarbeitete Auflage*. Springer-Verlag, Berlin Heidelberg.

[Frid et al., 2003] Frid, V., Rabinovitch, A., and Bahat, D. (2003). Fracture induced electromagnetic radiation. *Journal of Physics D: Applied Physics*, 36:1620–1628.

[Gade et al., 2014] Gade, S. O., Weiss, U., Peter, M. A., and Sause, M. G. R. (2014). Relation of electromagnetic emission and crack dynamics in epoxy resin materials `https://doi.org/10.1007/s10921-014-0265-5`. *Journal for Nondestructive Evaluation*, 33:711–723.

[Gibiansky, 1993] Gibiansky, L. V. (1993). Bounds on the effective moduli of composite materials. School on Homogenization ICTP, Trieste, September 6-17.

[Glowinski, 1983] Glowinski, R. (1983). Numerical simulation for some applied problems originating from continuum mechanics. In *Trends and Applications of Pure Mathematics to Mechanics, Invited and Contributed Papers presented at a Symposium at Ecole Polytechnique, Palaiseau, France November 28 - December 2*, Berlin Heidelberg. Spinger-Verlag.

[Hamstad, 1986] Hamstad, M. A. (1986). A review: Acoustic emission, a tool for composite-materials studies. *Experimental Mechanics*, 26:7–13.

[Hashin and Shtrikman, 1963] Hashin, Z. and Shtrikman, S. (1963). A variational approach to the theory of the elastic behavior of multiphase materials. *Journal of the Mechanics and Physics of Solids*, 11:127–140.

[Hunger, 2020] Hunger, R. (Accessed: 04.03.2020). An introduction to complex differentials and complex differentiability. https://mediatum.ub.tum.de/doc/631019/631019.pdf.

[Jackson, 2006] Jackson, J. D. (2006). *Klassische Elektrodynamik, 4., überarbeitete Auflage.* Walter de Gruyter, Berlin.

[Johnson and Dudgeon, 1993] Johnson, D. H. and Dudgeon, D. E. (1993). *Array Signal Processing: Concepts and Techniques.* PRT Prentice-Hall, Inc., Englewood Cliffs, New Jersey.

[Kielhöfer, 2010] Kielhöfer, H. (2010). *Variationsrechnung.* Vieweg + Teubner, Wiesbaden.

[Milton, 1980] Milton, G. W. (1980). Bounds on the complex dielectric constant of a composite material. *Applied Physics Letters*, 37:300.

[Milton, 1990] Milton, G. W. (1990). On characterizing the set of possible effective tensors of composites: The variational method and the translation method. *Communications on Pure and Applied Mathematics*, 43:63–125.

[Milton, 2002] Milton, G. W. (2002). *The theory of composites.* Cambridge University Press, Cambridge.

[Murat and Tartar, 1997a] Murat, F. and Tartar, L. (1997a). Calculus of variations and homogenization. In Cherkaev, A. and Kohn, R., editors, *Topics in the Mathematical Modelling of Composite Materials*, pages 21–43. Birkhäuser, Boston, MA.

[Murat and Tartar, 1997b] Murat, F. and Tartar, L. (1997b). H-convergence. In Cherkaev, A. and Kohn, R., editors, *Topics in the Mathematical Modelling of Composite Materials*, pages 21–43. Birkhäuser, Boston, MA.

[Orfanidis, 2019] Orfanidis, S. J. (Accessed: 16.10.2019). Electromagnetic waves and antennas. https://www.ece.rutgers.edu/ orfanidi/ewa/.

[Rudin, 1986] Rudin, W. (1986). *Real and Complex Analysis.* McGraw-Hill, New York u.a.

[Sause, 2016] Sause, M. G. R. (2016). *In situ monitoring of fiber-reinforced composites: theory, basic concepts, methods, and applications.* Springer Series in Materials Science, Cham.

[Sedlak et al., 2008] Sedlak, P., Sikula, J., Lokajicek, T., and Y., M. (2008). Acoustic and electromagnetic emission as a tool for crack localization. *Measurement Science and Technology*, 19(4):045701.

[Showalter, 1997] Showalter, R. E. (1997). *Monotone Operators in Banach Space and Nonlinear Partial Differential Equations.* American Mathematical Society; Mathematical Surveys and Monographs Volume 49.

[Sigmund and Maute, 2013] Sigmund, O. and Maute, K. (2013). Topology optimization approaches - a comparative review. *Structural and Multidisciplinary Optimization*, 48:1031–1055.

[Spagnolo, 1976] Spagnolo, S. (1976). Convergence in energy for elliptic operators. In *Proceedings of the 3rd Symposium on the Numerical Solution of Partial Differential Equations*, New York, San Francisco, London. Academic Press, INC.

[Tartar, 2009] Tartar, L. (2009). *The General Theory of Homogenization*. Springer-Verlag, Berlin Heidelberg.

[Tröltzsch, 2009] Tröltzsch, F. (2009). *Optimale Steuerung partieller Differentialgleichungen*. Vieweg+Teubner, Wiesbaden.

[von Winckel and Borzì, 2008] von Winckel, G. and Borzì, A. (2008). Computational techniques for a quantum control problem with H^1-cost. *Inverse Problems*, 24:034007.

[von Winckel et al., 2009] von Winckel, G., Borzì, A., and Volkwein, S. (2009). A globalized Newton method for the accurate solution of a dipole quantum control problem. *SIAM Journal on Scientific Computing*, 31(6):4176–4203.

[Wirtinger, 1926] Wirtinger, W. (1926). Zur formalen Theorie der Funktionen von mehr komplexen Veränderlichen. *Mathematische Annalen*, 97:357–375.